The potential of graphite, graphene, and amorphous carbon structures as DNA sensor platforms

Rob Vansweevelt

Promotor: prof. dr. Patrick Wagner

Copromotor: prof. dr. Chris Van Haesendonck

Acknowledgements

Now that I have come to the end of my PhD, it is time to thank all the people that have made it possible for me to be at this point. I have had the pleasure to get support, of all kinds, from a lot of people. Here, I would like to thank all of you for your contribution to this thesis.

Allereerst wil ik mijn promotor, prof. dr. Patrick Wagner alias Paddi, bedanken! Om te beginnen heb jij me de kans gegeven om te kunnen doctoreren in de BIOS groep. De afgelopen jaren heb je mijn onderzoek in het oog gehouden en gestuurd waar nodig. Dit heb je altijd gedaan met je kenmerkende brede glimlach en vriendelijkheid!

Ik wil ook mijn copromotor, prof. dr. Chris Van Haesendonck, bedanken voor het opvolgen van mijn werk. We hebben elkaar niet veel gezien maar op de momenten dat je me bijstond werd je hulp zeker en vast geapprecieerd. Bedankt voor het zorgvuldige nalezen van diverse teksten! Ik wil je ook bedanken voor de kennismaking met e-beam lithografie in de labo's van jouw groep.

Het derde lid van mijn doctoraatscommissie, prof. dr. Luc Michiels, wil ik bedanken om altijd aanwezig te zijn op mijn PhD meetings, waar je me ook altijd van de nodige tips en opbouwende kritiek voorzag. Natuurlijk ook bedankt om in mijn doctoraatscommissie te zetelen!

During the years of my PhD, I have had the luck to collaborate with external groups leading to very interesting results and of course getting acquainted with helpful and friendly people!

I would like to thank dr. Mirco Cantoro from the Nano Applications and Materials Engineering group of IMEC (Leuven) for the nice collaboration on the functionalization of graphene flakes. Thank you for showing me the Geim method and for providing me with the right material to do this! The production of graphene suddenly went a lot better. I also want to thank you for performing all the Raman measurements and for keeping to perform them when the first results did not look good. It is a pity that I did not have more time to work further on this promising collaboration.

Een andere persoon van IMEC die ik wil bedanken is dr. Michael De Volder. Bedankt voor het aanleveren van de prachtige structuren en voor de fijne samenwerking! Hopelijk zal het artikel snel aanvaard worden.

De allereerste samenwerking van mijn werk als PhD student was met dr. Annick Vanhulsel en Alexander Malesevic van het VITO (Mol). Bedankt voor de vele CNW stalen die ik van jullie heb gehad. Deze stalen hebben me mijn eerste resultaten opgeleverd. Alexander, het was fijn om met een oude klasgenoot te kunnen samenwerken.

Ik wil ook prof. dr. Margriet Van Bael en Lino da Costa Pereira van de KULeuven bedanken voor de SQUID metingen op HOPG.

Binnen het IMO zelf zijn er natuurlijk ook een hoop mensen die ik wil bedanken voor hun hulp. Dr. Jan D’Haen en Bart Ruttens wil ik bedanken voor de SEM metingen en de e-beam lithografie, dewelke veel tijd in beslag nam. Het was niet altijd gemakkelijk om een plaatsje te krijgen in jullie drukke programma maar uiteindelijk heeft de e-beam lithografie toch mooie resultaten opgeleverd.

I would like to thank prof. dr. Hans-Gerd Boyen for the XPS measurements and for stressing out the importance of clean sample preparation. For AFM measurements in the last years I could always go to dr. Hong Yin. Thank you Hong, you were always very friendly and motivated to do these measurements!

I also have to thank dr. Anitha Ethirajan for her advice and directions. You could be very persuasive but this just might have been what we needed. Thank you for all the help!

Dr. Vincent Mortet, thank you for the assistance with the setup and measurements for the electronic characterization! I wish you the best in France. Regarding this work, I also want to thank Stoffel Janssens for his help!

De volgende personen wil ik bedanken voor de toegang tot hun apparatuur: prof. dr. Marcel Ameloot voor de confocale fluorescentie microscoop; prof. dr. Luc Michiels voor de fluorescentie microscoop; prof. dr. Roland Valcke voor de fluorescentie spectrometer (PTI); prof. dr. Thomas Cleij voor de fluorescentie spectrometer (Horiba Yobin Yvon) en de infrarood spectrometer. Huguette Penxten bedank ik voor de uitleg en de infraroodspectroscopie metingen.

Verder wil ik ook nog de volgende personen bedanken voor hun hulp: Johnny om de apparatuur werkende te houden; Christel en Hilde voor de praktische werking, netheid en veiligheid van de labo's; Erik voor de computer-gerelateerde problemen; Jan, Lieven en Geert voor hun hulp bij de elektrische meetopstellingen; Lea, Relinde en Lisette voor de hulp met paperassen en het versturen van pakjes.

Tijdens de afgelopen jaren heb ik ook de hulp gehad van enkele stage studenten. Matthias, Martijn, Jef en Joeri bedankt voor jullie bijdrage!

De sfeer op het IMO, en daarbuiten, was altijd zeer aangenaam. Tussen het werk door was er dikwijls tijd voor een practical joke, een movie time, een quizke,….Ook als de resultaten tegen zaten waren er altijd de collega's om je verhaal tegen te doen.

Eerst was er de "oude garde" met Rob, Koen, Sylvia, Peter, Pieter, Ann, Michael, Ilse die voor de plezante sfeer zorgden. Tot deze "oude garde" behoorden ook Ronald en Wouter die ik nadrukkelijk wil bedanken voor de plezante sfeer op het IMO, op weg van en naar het IMO en tijdens de ontspannende avonden in de Ambi, Hemelrijk of andere oorden. Ik zal het carpoolen, de Kerstmannen, de practical jokes, het kreng van een vespa, het pokeren en nog zovele dingen nooit vergeten! En Wouter, merci voor de kennismaking met uw lieftallige zus!

De "oude garde" werd stilaan vervangen door de "nieuwe garde". Evi, Lars, Jan, Bert, Bart, Stoffel, Kasper, Matthias, Marloes, Mohammed, Thijs en Stijn, allemaal bedankt voor de toffe sfeer en de ontspanning tijdens en na het werk. Jullie waren een plezante bende en het zal zeer moeilijk zijn om collega's te vinden die jullie evenaren. Ik denk dat het wel op zijn plaats is om Lars nog eens extra te bedanken voor zijn tomeloze hulp en collegialiteit voor heel de BIOS groep en zelfs heel het IMO. Alleen nog een beetje werken aan die zuren!

Dan resten nog de mensen die niets met het werk te maken hebben maar toch hebben bijgedragen door hun steun op het thuisfront. Yvan en Gert, ik ben jullie zeer dankbaar voor alle steun! Men zegt dat de ideale "schoonouders" niet bestaan maar jullie komen toch in de buurt!

Mama, papa, Loes en Bieke, bedankt voor de warme thuis die jullie me altijd geboden hebben! Bedankt om me de kans te geven om te studeren en zeker om me te laten blijven studeren na mijn jonge jaren waarin studeren nog niet mijn prioriteit was. Bedankt voor het feit dat ik altijd op jullie kon en nog steeds kan rekenen!

Tot slot mijn Belleke, bedankt voor de afgelopen drie jaar. Ik ben superblij dat je bij me bent en ik kijk er naar uit om samen onze toekomstplannen te verwezenlijken! Ik hou van u!

Table of contents

Acknowledgements II

Table of contents VI

Abstract IX

Nederlandstalige samenvatting XII

Chapter 1 Introduction 1

- 1.1. Carbon 2
- 1.2. Graphene 3
  - 1.2.1. Historical overview 4
  - 1.2.2. Graphene structure 6
  - 1.2.3. Defects 7
  - 1.2.4. Physical properties 9
  - 1.2.5. Graphene production 17
  - 1.2.6. Chemical modification and functionalization 25
  - 1.2.7. Applications 30

Chapter 2 Characterization techniques 32

- 2.1 Optical microscopy 32
- 2.2 Raman spectroscopy 33
- 2.3 Atomic force microscopy 36
- 2.4 Scanning electron microscopy 39
- 2.5 Contact angle measurements 42
- 2.6 X-ray photoelectron spectroscopy 43
- 2.7 Fluorescence-based techniques 45
  - 2.7.1 Fluorescence theory 45
  - 2.7.2 Fluorescence microscopy 47
  - 2.7.3 Confocal laser-scanning fluorescence microscopy 48
  - 2.7.4 Fluorescence spectroscopy 51

Chapter 3 Functionalization of carbon nanowalls 53

- 3.1 Introduction 53
- 3.2 CNW structure 54

3.3 Synthesis by MW PECVD 56
3.4 Functionalization with DNA strands 57
3.4.1 Attachment of probe DNA 58
3.4.2 Hybridization of target DNA 61
3.4.3 Substrate investigation 66
3.5 Conclusion 68
Chapter 4 Functionalization of ultrathin graphite flakes and graphene 70
4.1 Introduction 70
4.2 Production of flakes 71
4.2.1 The Geim method 71
4.2.2 Liquid-phase exfoliation 72
4.3 Non-covalent functionalization 72
4.3.1 Method 72
4.3.2 Results on non-covalent functionalization 74
4.3.3 Conclusion on non-covalent functionalization 80
4.4 Covalent functionalization 81
4.4.1 Diazonium salts 83
4.4.2 4-nitrobenzene diazonium tetrafluoroborate 83
4.4.3 4-Benzoic acid diazonium tetrafluoroborate 88
4.4.4 Conclusion on covalent functionalization 94
Chapter 5 Functionalization of amorphous carbon microstructures 96
5.1 Fabrication of amorphous carbon microstructures 97
5.2 Morphology of the microstructures 97
5.3 Functionalization method 99
5.4 Functionalization results 101
5.5 Resistance measurements on bridge structures 105
5.5.1 Measurement method 105
5.5.2 Results on resistance measurements 106
5.6 Conclusions 109
Chapter 6 Electronic characterization of ultrathin graphite flakes 111
6.1 Sample preparation 112
6.1.1 Flake deposition 112

6.1.2 Electrical contact preparation 112

6.2 Cryostat setup 114

6.3 Results 115

6.3.1 Colossal positive magnetoresistance 115

6.3.2 Hall effect- and mobility study 122

6.4 Conclusion 130

Chapter 7 Conclusion and outlook 132

References 136

Appendix 1: List of abbreviations 152

Appendix 2: Publications and conference contributions 155

Appendix 3: List of figures and tables 158

Abstract

The potential of graphene, graphite and amorphous carbon as DNA sensor platforms was investigated. Therefore, different functionalization strategies to bind DNA strands to graphene, thin graphite and amorphous carbon were tested. Furthermore, ultrathin graphite flakes were electronically characterized as a first step in the development of sp^2 carbon based sensors with electronic readout.

The hydrogen-terminated edges and defect sites of carbon nanowalls (CNW), upstanding microplates made out of 4-6 stacked graphene sheets, were succesfully functionalized with single stranded DNA. DNA strands were covalently bonded using a fatty acid linker molecule. The fatty acid linker was attached to the CNW edges through a photochemical reaction. This was followed by the coupling of amino-labeled DNA to the carboxylic acid groups of the fatty acid linker, using 1-ethyl-3-(3-dimethylaminopropyl)-carbodiimide (EDC) as a mediator. Hybridization experiments in combination with fluorescence microscopy allowed for the clear differentiation between fully complementary target DNA and DNA with a single mismatch, out of a 29 nucleotides sequence. The optimal hybridization temperature to achieve high selectivity was found to be 60 °C. Furthermore, hybridized DNA could be denatured and rehybridized for at least 10 cycles.

In order to increase the DNA functionalization levels, different functionalization routes that act upon the basal plane of sp^2 carbon were tested. First, a non-covalent method, based on π-π stacking, was investigated. A pyrene-like molecule was used to π-stack with the aromatic structure of graphene and graphite. The pyrene-like molecule also contained a carboxylic acid group that was used to couple DNA with the known EDC-mediated reaction. However, different experiments using fluorescence microscopy, fluorescence spectroscopy and XPS could not prove the binding of DNA or the pyrene-like linker to the graphene or graphite surface. The functionalizing species are probably rinsed off by mild washing steps.

A second, covalent, method was tested to functionalize the graphene and graphite surface with DNA strands. This method was based upon diazonium salts. The aim was to use the diazonium as a linker to attach the DNA, again via the known EDC-mediated reaction. Two different diazonium molecules were used. The first one resulted in nitro groups as an anchor point for further DNA coupling. Since the required reduction of the nitro groups into amino groups posed some problems, another diazonium molecule, with a carboxylic acid group, was used to facilitate the DNA coupling. This second type of diazonium, 4-benzoic acid diazonium tetrafluoroborate, was homemade by two different methods. Functionalization was investigated with Raman spectroscopy, as this method allows to characterize preselected individual flakes. The results from Raman spectroscopy (and XPS) indicated that a part of the diazonium physisorbs to the graphene, as it could be removed by thorough washing steps, while another part of the diazonium covalently binds to the graphene surface. This covalent binding was shown by the appearance of a defect-related D peak in the Raman spectra of functionalized samples. The presence of DNA was not clearly detected by the Raman spectroscopy and no real difference between samples with(EDC-positive) and without (EDC-negative) the necessary EDC-mediator could be observed.

In addition to graphene-like materials, amorphous carbon microstructures were tested for their potential use in DNA sensing. The amorphous carbon microstructures contained an outer layer of nanostructured carbon, drastically enhancing the surface area. The amorphous carbon microstructures were successfully functionalized by the fatty acid route and by the diazonium route, as shown by confocal fluorescence microscopy. Amorphous carbon microstructures, lacking the nanostructured outer layer, were used as a reference. It was clear that these regular microstructures showed greatly reduced functionalization levels due to the much smaller surface area. The electrical resistance over bridge-shaped amorphous carbon microstructures was measured using a four probe technique. The resistance change for positive samples was 40 % lower than the change for EDC-negative samples, and this for the samples functionalized via the fatty acid route. Samples functionalized via the diazonium route display a difference in resistance change of 12 %. Bulk amorphous carbon structures did not show a difference in resistance change between positive and EDC-negative reference samples.

In order to further investigate the potential of sp^2 carbon as DNA sensor platforms, ultrathin graphite flakes were electronically characterized. Four electrical contacts in van der Pauw configuration were deposited on individual flakes, with a thickness of 25 – 50 nm, using e-beam lithography. The samples showed a zero-field resistivity of 40 – 55 μΩcm at room temperature. The magnetoresistance effect of the samples was studied in magnetic fields up to 2.06 T and in a temperature range of 5 K – 400 K. At fields of 2.06 T, positive magnetoresistance effects of up to 130 % and 235 % were found for temperatures of 300 K and 77 K, respectively. It was also proven that in-plane components of the magnetic field had no effect on the magnetoresistance. Next, the Hall voltage was investigated in function of magnetic field (0.1 T – 2.06 T) and temperature (77 K – 400 K). The Hall voltage exhibits a linear field dependence for the lowest fields and shows a downward bent for higher fields. The charge carrier concentrations and mobilities were determined, using the zero-field resistivity and Hall measurements, for low magnetic fields in a temperature range of 77 K – 300 K. Charge carrier mobilities up to 891 cm^2/Vs ($n = 1.75 \times 10^{20}$ cm^{-3}) and 1329 cm^2/Vs ($n = 8.28 \times 10^{19}$ cm^{-3}) were found at 300 K and 77 K, respectively.

Nederlandstalige samenvatting

Grafeen is een flinterdun laagje koolstof waarvan de structuur vergeleken kan worden met kippengaas. Echt grafeen is slechts één atoomlaag dik, wat overeenkomt met 0.335 nm, en werd pas ontdekt in 2004. Omwille van zijn speciale structuur en tweedimensionale vorm bezit het zeer interessante en unieke fysische eigenschappen. Het is dan ook een materiaal van verschillende superlatieven; het is niet alleen het dunste materiaal ter wereld maar ook het sterkste. Samen met koolstof nanobuizen, welke kunnen gezien worden als opgerolde grafeenvellen, heeft het de beste thermische geleidbaarheid van de tot nu toe gemeten materialen. De elektrische ladingsdragers in grafeen verplaatsen zich met een extreem hoge snelheid en vertonen nog tal van andere unieke eigenschappen.

In deze thesis werd onderzocht of deze grafeenlagen en verwante materialen potentieel bezitten om gebruikt te worden in elektrisch uitleesbare DNA sensoren. Met DNA sensoren worden sensoren bedoeld die specifieke DNA sequenties kunnen detecteren. Ze kunnen bijvoorbeeld gebruikt worden om DNA mutaties of genetische verwantschappen op te sporen. Om te kunnen dienen als platform voor DNA sensoren is het noodzakelijk dat er DNA strengen aan deze grafeenlagen gebonden kunnen worden. Het binden van DNA aan deze lagen noemen we functionalisatie van de grafeenlagen. Verschillende bindingsmethoden werden getest om DNA aan grafeen-achtige materialen te binden. Elke bindingsmethode mikt op een specifiek type materiaal.

Koolstof nanomuurtjes, bestaande uit rechtopstaande pakketjes van 4-6 grafeenlagen, werden gefunctionaliseerd met enkelstrengig DNA. De functionalisatie vond plaats op de randen van de nanomuurtjes en op defecten. Om het DNA covalent te binden werd eerst een linker molecule, een onverzadigd vetzuur, aan het DNA bevestigd met behulp van een fotochemische reactie. De carboxyl groep aan het uiteinde van dit vetzuur werd gebruikt in een tweede reactie, gekatalyseerd door EDC, om amino-gemodificeerd DNA te binden. Doordat DNA gebruikt werd dat gelabeled was met een fluorescerende groep, was het mogelijk om het resultaat van de bindingsreacties te analyseren met behulp van fluorescentie microscopie. Hybridisatie experimenten toonden aan dat er een onderscheid gemaakt kon worden tussen volledig complementaire DNA paren en paren met één fout of mutatie in de sequentie. Dit betekent dat het systeem een hoge selectiviteit bezit. De herbruikbaarheid van het systeem werd getest door 10 opeenvolgende cycli van hybridisatie en denaturatie uit te voeren.

Vervolgens werd getracht om het oppervlak van individuele grafeen en dunne grafietlagen te functionaliseren met DNA. Eerst werd een niet-covalente methode onderzocht. Hiervoor werd een linkermolecule gebruikt met een pyreen groep. De pyreengroep zou dan kunnen interageren met de aromatische structuur van het grafeen oppervlak door middel van π-π stapeling. Deze methode bleek echter niet succesvol, waarschijnlijk doordat de binding niet sterk genoeg was om de nodige spoelstappen te kunnen doorstaan. Daarna werd er overgeschakeld op een covalente bindingsmethode waarbij diazonium zouten gebruikt werden als linker molecules. Raman spectroscopie werd aangewend om de gefunctionaliseerde stalen te karakteriseren vermits deze methode het toelaat om te focussen op één grafeenschilfer zonder het omliggende substraat mee te meten. De resultaten toonden aan dat het diazonium gedeeltelijk covalent gebonden was en gedeeltelijk geadsorbeerd aan het oppervlak. De aanwezigheid van DNA werd echter niet aangetoond. Het is wel mogelijk dat DNA aanwezig was op het oppervlak maar dat het niet gedetecteerd kon worden met de gebruikte karakterisatiemethode. Deze bewering is gebaseerd op andere experimenten, uitgevoerd op diamant en amorfe koolstof, waar de aanwezigheid van DNA wel aangetoond werd na binding met diazonium linkers.

Er werd ook een niet-grafeen-achtig materiaal gebruikt om een provisoire DNA sensor te ontwikkelen. Hiervoor werden amorfe koolstof microstructuren gefunctionaliseerd met DNA. Deze amorfe koolstof microstructuren bevatten een nanogestructureerde buitenste laag die resulteert in een immens groot contactoppervlak. Dit laatste wilt zeggen dat er veel DNA strengen gebonden kunnen worden. De twee bovengenoemde linker methodes, vetzuur en diazonium zouten, werden in combinatie met de EDC-reactie met succes gebruikt om DNA te binden aan deze structuren. Om sensor potentieel van deze structuren verder te onderzoeken werd de elektrische weerstand over deze structuren gemeten, en dit voor en na de binding met DNA. Vergelijking van de verandering in weerstand na de DNA binding voor een positief staal en een EDC-negatief referentiestaal toonde aan dat de weerstandsverandering voor het positief staal 40 % kleiner was dan voor het referentiestaal. Dit wilt zeggen dat de binding van DNA gedetecteerd kon worden en er dus eigenlijk een elementaire DNA sensor ontwikkeld werd.

Tenslotte werden ook nog de elektronische eigenschappen van uiterst dunne grafietschilfers (75 – 150 grafeenlaagjes dik) onderzocht. Er werden vier elektrische contacten aangebracht op individuele grafietschilfers met behulp van elektronenbundel lithografie. Zo werd er een resistiviteit van 40 µΩcm gevonden in de richting evenwijdig met de grafeenlagen. De magnetoweerstand werd onderzocht in magneetvelden van 0 T tot 2.06 T en een temperatuurbereik van 77 K tot 300 K. De stalen bleken een gigantisch magnetoweerstandseffect te vertonen in de positieve richting. Zo vergrootte de resistiviteit met 235 % bij een magnetische veldsterkte van 2.06 T en een temperatuur van 77 K. Verder werd de invloed van het magneetveld op de Hallspanning getest. Initieel vertoont de Hall spanning een lineaire vergroting met toenemende magnetische veldsterkte. Bij hogere magnetische veldsterktes werd de toename in Hallspanning afgezwakt of daalde ze zelfs. De resistiviteit en Hall spanning werden gebruikt om de dichtheid en mobiliteit van de ladingsdragers te bepalen. Zo werd er gevonden dat de geleiding voornamelijk bepaald werd door gatengeleiding in plaats van elektronengeleiding. Er werd een mobiliteitswaarde van 1329 cm^2/Vs gevonden bij een temperatuur van 77 K.

Dit werk toonde aan dat grafeen, grafeen-achtige materialen en amorfe koolstofstructuren kunnen dienen als bindingsplatform voor DNA strengen. Een primitieve elektrische DNA sensor werd ontwikkeld op basis van amorfe koolstofstructuren en de eerste stappen werden genomen in de karakterisatie van de elektronische eigenschappen van grafeen-achtige materialen. Verder onderzoek zal de invloed van DNA binding op de elektrische eigenschappen van grafeen-achtige structuren moeten onderzoeken om zo grafeen-gebaseerde DNA sensoren te ontwikkelen met elektrische uitlezing.

Chapter 1

Introduction

Despite the general thought that a pure two-dimensional material, consisting of only one single atomic layer, could not exist, the isolation of two-dimensional graphene from graphite became a fact in 2004. Geim and coworkers produced and observed an atomic layer of carbon atoms by peeling off a graphite crystal [1]. This single layer carbon material is called graphene and it is the subject of a super-fast growing amount of research papers from all over the world. The topic graphene is hot and this was illustrated by awarding the 2010 Nobel Prize in Physics to A. Geim and K. Novoselov "*for groundbreaking experiments regarding the two-dimensional material graphene*".

In this work graphene and graphene-like materials are studied for their potential use in biosensors and more specific DNA sensors. A biosensor is a sensing device that uses a biological or biomimetic component to detect an analyte of interest. The idea behind developing a DNA sensor is to be able to detect specific DNA sequences in test samples. One could for example perform DNA tests to identify criminal offenders or verify genetic relations between people or animals. DNA sensors could also be used in screening for diseases marked by a specific DNA mutation. Current DNA tests are mostly based on relatively slow and labor intensive working methods such as PCR combined with electrophoresis and microarrays. The development of DNA sensors, and biosensors in general, should lead to significantly faster, easier and cheaper testing.

Very little research has been done on the use of graphene and graphene-like materials as biosensing platforms. Graphene-like materials can be used at the same time as anchoring surfaces for biomolecules and as transducers to convert an analyte recognition event into a measurable signal. The potential advantages of graphene in biosensor development are its size, elemental composition and its unique physical properties. Graphene with its (sub)nanometer scale thickness and micrometer scale lateral dimensions is perfectly suited for miniaturization of sensing devices. The fact that graphene consist solely of carbon atoms makes graphene a good candidate for the production of biocompatible sensors. And finally, the unique physical properties, which will be dealt with later in this thesis, could lead to very fast and extremely sensitive biosensors. Some work already exists to support this idea. Adsorption or binding of DNA [2,3], bacteria [3], antigens [4] and even single gas molecules [5] evoked a detectable change in the electronic properties of graphene.

1.1. Carbon

Carbon is a relatively rare element on earth; less than 0.1 % of all elements on earth is carbon according to Wikipedia. Although it might be rare, it is an extremely important element. Together with a few other elements it forms the basic building block for all living organisms on earth. Furthermore, carbon is the sole building block of some unique materials like for example diamond, graphite, bucky balls, carbon nanotubes (CNT) and off course the subject of this thesis: graphene.

Carbon, denoted by symbol C, is element number 6 in the periodic table of elements and has the following electronic configuration: $1s^2$ $2s^2$ $2p_x^1$ $2p_y^1$. Carbon belongs to the same group as silicon and germanium for example. The elements in this group can form a maximum of four covalent bonds with one to four different atoms. Depending on the type of bond, carbon can form a variety of materials. So are diamond and graphite, the hardest material and one of the softest materials, due to its layered structure, both composed of carbon. This different type of bonding can be explained by describing different hybridizations of the atomic orbitals of carbon, shown in Figure 1-1. The valence s-orbital can hybridize with one p-orbital to form two sp-hybridized orbitals. Together with two unchanged p-orbitals a triple bond can be formed between two carbon atoms. Another type of hybridization is the sp^2 hybrid. Three of these hybrids are formed when the 2s orbital mixes with two p-orbitals. A carbon atom of this type can form three different σ-bonds and one π-bond to make up a double bond. These bonds are oriented in a plane with angles of 120° between the bonds. Graphite, graphene and carbon nanotubes are all sp^2-bonded. A third and last type of hybrid can be made when the 2s orbital hybridizes with all three 2p orbitals, generating 4 hybridized sp^3-orbitals. These can make 4 σ-bonds in a tetrahedral configuration with angles of 109.5° between all bonds/orbitals. Diamond has an sp^3 configuration. [6]

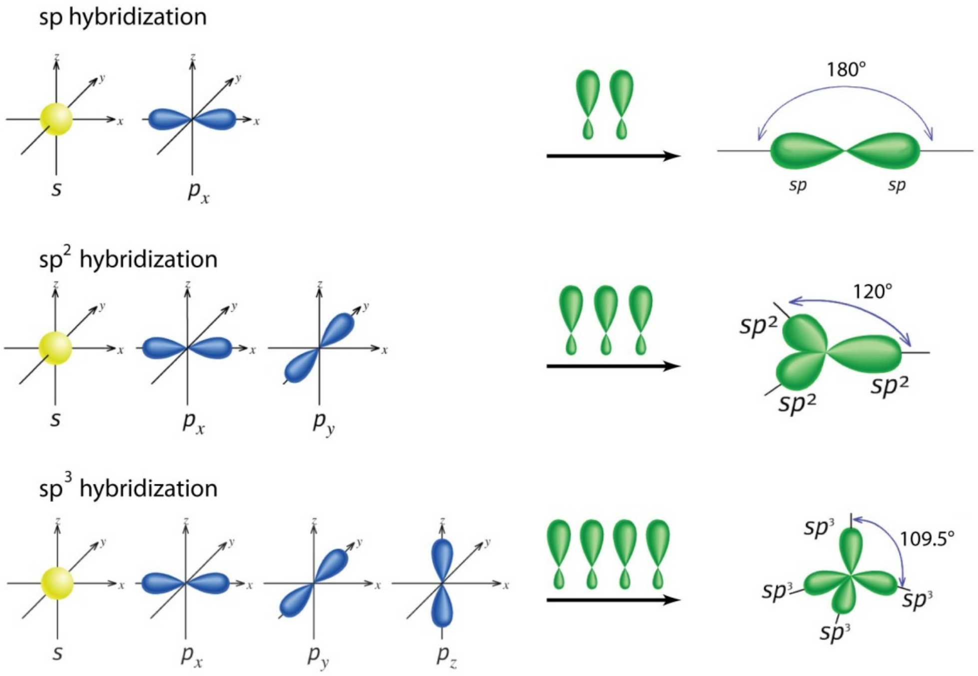

Figure 1-1. Illustration of different atomic orbital hybridizations of carbon. Adapted from [7].

1.2. Graphene

After a short background of this work and a brief introduction into carbon, this section will deal with graphene itself. The discovery of this carbon layer with single atomic thickness will be described first, followed by the structure, potential structural defects and physical properties of graphene. Furthermore different methods to produce graphene will be described. Some possible chemical modifications will be explained and future applications will be given.

1.2.1. Historical overview

In order to describe the history of graphene one has to start long before the actual isolation and observation of graphene by Geim and Novoselov. Terms like graphite oxide and graphite intercalation compounds, which are now used as precursors for graphene, already turned up in the 1840s. German scientist Schafhaeutl reported on the intercalation and exfoliation of graphite [8,9]. More work on graphite oxide was published in the following decades by Brodie and Staudenmaier [10,11].

The history of graphene itself starts in 1947 with Philip Russell Wallace, a Canadian theoretical physicist. While working on graphite, Wallace realized that this graphite consists of loosely bound carbon layers. He became interested in the properties of single layers, mostly to describe the more complex 3D graphite structure. He performed some calculating work on these single layers and concluded that the electrons in graphene behave like massless particles [12]. In the 1950s more theoretical work was published where graphite was modeled by single layers to calculate the band structure [13] and explain diamagnetism [14].

The next fact in graphene's history was in 1962 when Boehm and coworkers chemically reduced dispersions of graphite oxide. This yielded thin carbon sheets with a low hydrogen and oxygen content. By using transmission electron microscopy (TEM) they determined a minimal thickness of 0.46 nm, which must be attributed to single layer carbon [15]. This was followed by the detection of graphene in Auger spectra by Blakely and coworkers in 1974. They were investigating the surface segregation of carbon on nickel surfaces [16,17]. Carbon, dissolved in metal alloys, phase separated and formed single or multiple carbon layers on the surface after exposure to elevated temperatures.

The term "graphene" was invented in 1986 by Boehm [18] and was formalized in 1997 when IUPAC incorporated it into their Compendium of Chemical Technology [19,20]. Despite all the previous work and formalization of the term graphene, it was believed that graphene could not exist. According to the Mermin-Wagner theorem, a strictly two-dimensional crystal would be thermodynamically unstable and would break or curl up to form soot or fullerenes [21-23].

It was waiting until 2004 for the big event when Geim and Novoselov from Manchester University found a way to produce actual pristine graphene [1]. It was only now that the term graphene became known to a broader scientific community. The common idea that they produced graphene for the first time by just peeling off graphene from graphite (or even pencil) with scotch tape is a bit simplistic. They started from highly oriented pyrolytic graphite (HOPG) from which they etched 5 µm high squares or mesas of different sizes. Then they pressed these mesas to a substrate covered with wet photoresist. After baking, the mesas could be cleaved off from the rest of the HOPG as they were attached to the photoresist. It was only then that the Scotch tape came into the story. Using the Scotch tape they kept peeling off thick flakes from the mesas on the resist. Thin flakes that were still on the resist were released by dissolving in acetone. A silicon (Si) substrate was subsequently dipped in the acetone solution to fish out thin flakes. After some washing steps their sample was ready. By serendipity they found that the use of Si wafers covered with a specific thickness of silicon dioxide (SiO_2) was essential for the optical observation of graphene.

Since then graphene became a rapidly rising "star" on the horizon of materials science and condensed-matter physics, as said by Geim himself [24]. He was not exaggerating: the number of research papers on the topic boomed (see Figure 1-2) and more and more properties, production methods and potential applications are found. Nowadays, graphene becomes known to the general public.

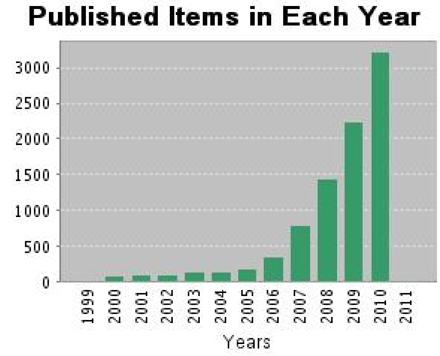

Figure 1-2. Number of manuscripts per year when the search term "graphene" was entered as topic in Web of Knowledge.

1.2.2. Graphene structure

As mentioned before, graphene is a single atomic layer of carbon atoms. The carbon atoms are sp^2-hybridized and therefore are arranged in a hexagonal crystal lattice. The atomic structure of graphene can be compared with chicken wire or a honeycomb. This structure was confirmed for example by scanning tunneling microscopy (STM) [25]. The bond length between two carbon atoms in graphene is about 0.142 nm. Although considered as a flat sheet, graphene is actually rippled, see Figure 1-3. Experimental observation [26] and theoretical calculations [27,28] show an out-of-plane deformation of about 1nm. The lateral size distribution of these ripples is 50-100 nm. These ripples may be the reason that relatively large graphene sheets are stable at all. They can be seen as a mechanism to lower the thermal vibrations that threaten the stability of all two-dimensional layers. One should bear in mind that it was believed that strictly two-dimensional structures could not exist without support.

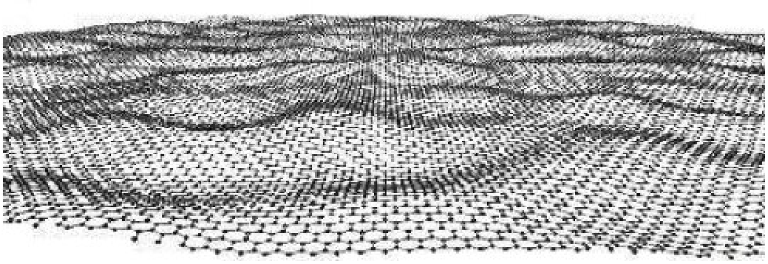

Figure 1-3. Artistic impression of a rippled graphene sheet [26].

Graphene can be considered as the base material from which other sp^2 carbon allotropes can be folded. Figure 1-4 illustrates how graphene can be shaped into a bucky ball (0D) or carbon nanotubes (1D). Different graphene layers stacked on top of each other make up graphite (3D) off course. While graphene consists solely off hexagons, bucky balls also contain 12 pentagons. Carbon nanotubes can also possess some pentagons if they have closed ends.

The interlayer spacing in stacks of multiple layers is 0.335 nm. The layers in few-layer graphene (FLG) and graphite are held together by weak van der Waals forces. The layers are stacked in an ABAB configuration or Bernal stacking. It means that the layers are shifted relative to each other to form a hexagonal close packing. Two adjacent carbon atoms in the layer are non-equivalent. Half of the carbon atoms have a neighbor straight above and below them. The other half lies over and under the centre of hexagons of the adjacent layers [29]. There is also an ABCABC stacking with a rhombohedral crystal lattice. This is a metastable phase and has not been observed as a separate phase in natural graphite [30].

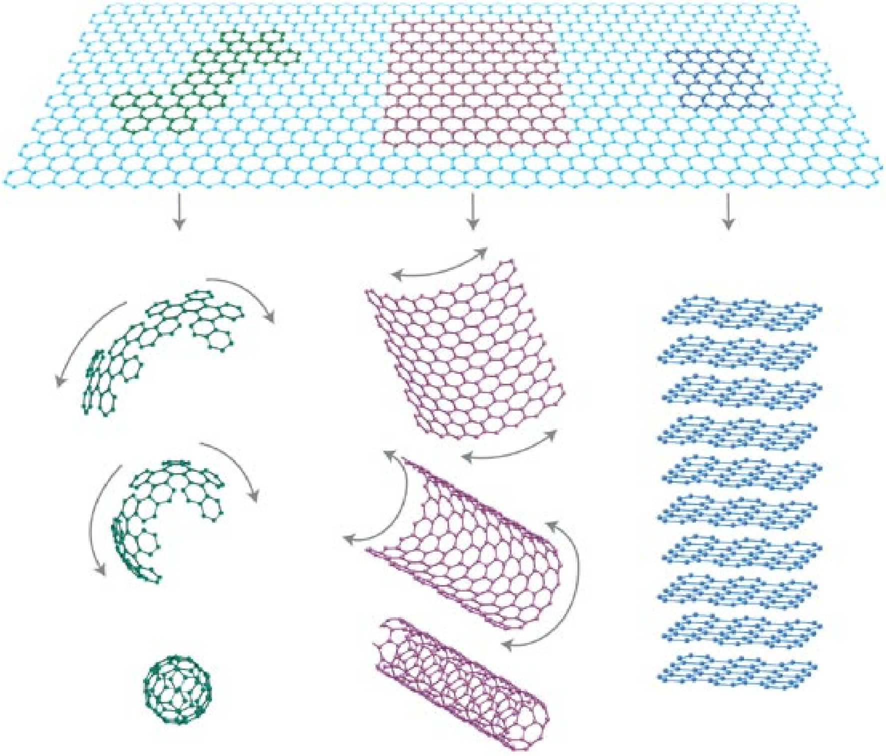

Figure 1-4. Graphene sheet (top) as the base for other sp^2 carbon materials. Folding yields 0D bucky balls (left) or 1D carbon nanotubes (middle). Stacking gives 3D graphite (right) [24]*.*

1.2.3. Defects

Defects or imperfections can play a crucial role in the electronic, chemical and morphological properties of crystalline structures. Graphene can potentially possess a variety of defects, a lot of them are already known from carbon nanotubes and other sp^2 carbon materials. The different types of defects in graphene can be grouped in different categories [31,32]. A first category comprises the structural defects. These are usually caused by the presence of non-hexagonal rings, like pentagons or heptagons. The presence of such a pentagon or heptagon leads to the formation of curvatures in the structure. Bond rotations are a second but related category. A carbon-carbon bond rotation leads to the formation of pairs of non-hexagonal rings. These pairs only induce local curvature changes as compared to the structural defects that cause an overall topography change. A well-known defect is the Stone-Wales defect [33,34] where a bond is rotated over 90°. This converts four hexagonal rings into two pentagons and two heptagons. This is illustrated in Figure 1-5.

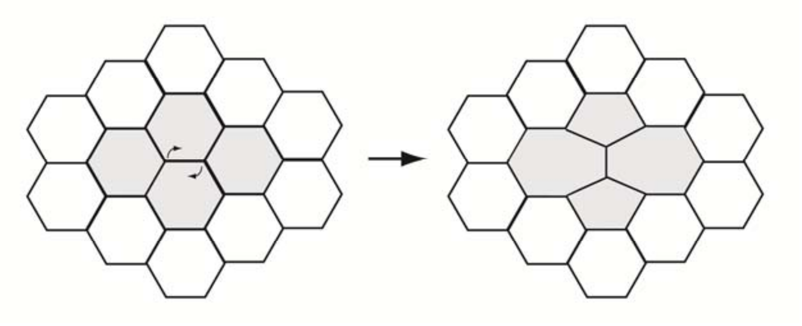

Figure 1-5. Illustration of Stone-Wales defect. Rotation of one carbon-carbon bond over 90°, resulting in two pentagons and two heptagons.

A third group are doping-related defects where non-carbon atoms can substitute carbon atoms. Nitrogen and boron are two examples of possible dopants. These are especially important for the electronic properties of graphene as they increase n-type and p-type conductivity, respectively. A last category are non-sp^2 carbon defects. In this case, highly reactive carbon species are present in the form of dangling bonds, interstitials, adatoms and vacancies. Graphene edges can also be seen as defects and fall in this category. The graphene edges have very different chemical and electronic properties compared to bulk graphene [35,36]. In graphene nanoribbons, these edges become a dominant factor in the characteristics of the whole nanoribbon [37-41].

Defects in graphene structure can be exploited or even deliberately introduced to tune its physicochemical properties.

1.2.4. Physical properties

Electronic properties

The electronic properties of graphene have opened new doors in physics and they are often described as exotic and unique. Charge carriers in graphene cannot be described with regular nonrelativistic quantum mechanics and the Schrödinger equation. They obey the rules of relativistic quantum mechanics also called quantum electrodynamics (QED). Charge carriers in graphene are described as massless Dirac fermions. This type of physics could be observed only in cosmology and high-energy particle accelerators. With the discovery of graphene however, these phenomena of quantum electrodynamics can be studied in the laboratory. For now, graphene is the only solid known to exhibit these quantum electrodynamics [42]. This is partly due to the fact that graphene can be produced or isolated with exceptional crystalline quality. Other existing 2D materials lack this electronic quality.

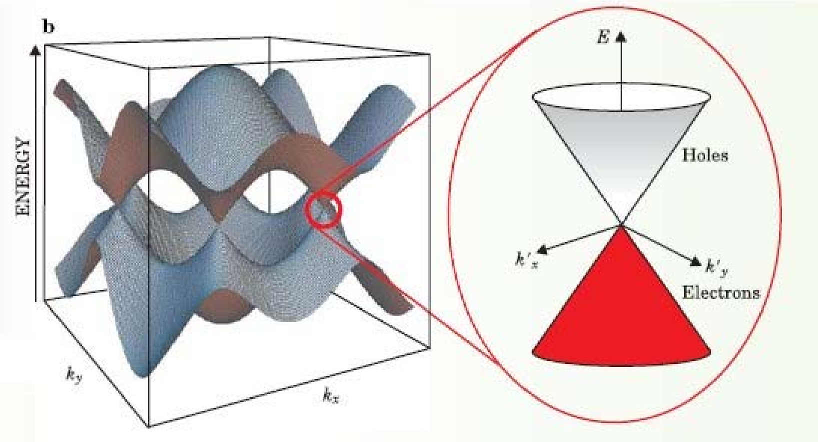

Figure 1-6. Electronic band structure of graphene, showing the dependence of energy on momentum. The right side illustrates the conical shape of the touching valence and conduction bands around the K point. [43]

A single graphene layer is a zero-gap semiconductor. The electronic band structure of graphene, shown in Figure 1-6, is determined by its π-orbitals. The valence and conduction bands touch each other at the K points, also called Dirac points. These K points are the corners of a two-dimensional hexagonal Brillouin zone. There are actually three K points and three K' points linked to the two sublattices of graphene. The low energy band structure around these K points resembles two touching cones with a linear energy-momentum (E-k) dispersion relation. The dispersion relation is given by the following equation:

$E = |\hbar k| v_f$, where $\hbar k$ is momentum and v_f is the Fermi velocity

The Fermi velocity in this case is 10^6 m s^{-1}, which is 300 times slower than the speed of light. A consequence of this linear dispersion relation is that the charge carriers behave as massless particles [24,42-45].

The type of charge carriers and the carrier density (n) can be tuned by applying a gate voltage. This ambipolar field effect is possible through the raising or lowering of the Fermi energy. The Fermi energy is lowered by applying a negative gate voltage, resulting in hole-type charge carriers. Electron-type charge carriers can be induced by positive gate voltages. Without the presence of an electric field, there is a mixed state of charge carriers, neutralizing each other. Charge carrier density can also be increased by increasing temperature. [1]

These charge carriers in graphene show ballistic transport on micrometer scale. Charge carrier mobility (μ) values as high as 15000 cm^2/Vs were measured under ambient conditions [1,44,46]. This mobility is even improved to values around 30000 cm^2/Vs (at $n = 2.10^{11}$ cm^{-2}) by measuring at low temperature and vacuum conditions. However, mobility measurements done on suspended and annealed graphene reached a stunningly high value of 230000 cm^2/Vs (at $n = 2.10^{11}$ cm^{-2}) [47]. Lower mobility values are due to scattering of charge carriers. It is believed that this scattering stems mostly from sources extrinsic to graphene because of the exceptional quality of graphene. These scattering sources can be adsorbates and the presence of substrates.

Another exotic aspect of graphene is that its conductivity never falls below a certain value, even when charge carrier concentration goes to zero. Some theoretical calculations predict a conductivity minimum of $\sigma = 4e^2/\pi h$ [48-50] while others predict a conductance quantum of (4)e^2/h [44,51,52]. The factor 4 points to double spin and double valley degeneracy (from the two sublattices) in graphene. Experimental work gave conductivity minima values of $2e^2/h$ to $12e^2/h$ [44,53], independent of temperature up to 100 K. For clarity, $\sigma_{min} = 4e^2/h$ equals ρ_{max} = 6.4 kΩ/□.

Graphene shows an anomalous quantum Hall effect (QHE) in the sense that the quantization condition is given by half integers instead of the normal integer values. For a regular QHE the expected Hall conductivity (σ_{xy}) plateaus are situated at $(4e^2/h)N$ where N is an integer. The σ_{xy} plateaus in graphene however are situated at $(4e^2/h)(N+1/2)$. This is shown in Figure 1-7, an actual measurement of the QHE in graphene and bilayer graphene (inset). The QHE of bilayer graphene is described below.

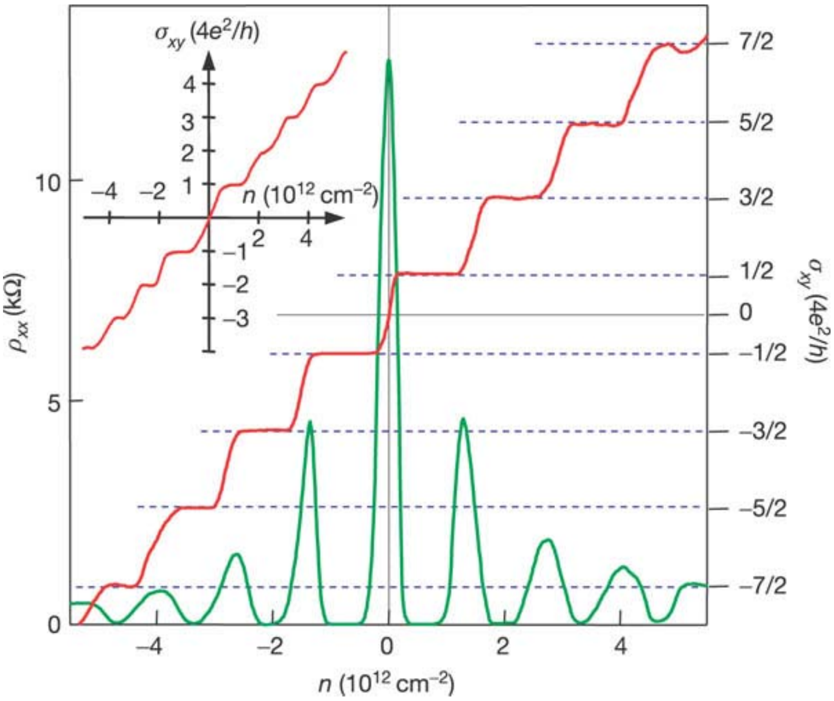

Figure 1-7. Quantum Hall effect measurement on single and double (inset) layer graphene. The oscillating and step-like curves show the longitudinal resistivity (ρ_{xx}) and the Hall conductivity (σ_{xy}), respectively, in function of the carrier density (n) [44].

The origin of the quantization of the Hall effect are the Landau levels. These Landau levels are discrete energy levels, linked to cyclotron orbits that can be occupied by charged particles in a magnetic field. The higher the strength of the magnetic field, the more particles can occupy a specific Landau Level. These Landau levels cause oscillations of the electronic properties of materials in the presence of magnetic fields, like the Shubnikov-De Haas effect. The Hall conductivity shows plateaus when the Fermi energy (E_f), which can be tuned by a gate voltage, is located in the Landau level tails. When E_f crosses a Landau level the Hall conductivity changes by $4e^2/h$. In the special case of graphene, the first plateau occurs at $\pm 2e^2/h$. The end of the first hole plateau and the beginning of the first electron plateau share the same Landau level, namely the zero-energy level. The existence of this zero-energy Landau level is typical for the unique band structure of graphene [44,54-56]. The presence of this half integer quantum Hall effect is a proof for the relativistic Dirac like nature of graphene's charged particles.

Another exotic and highly counterintuitive property of Dirac like particles is the Klein tunneling, also called Klein paradox [57]. Klein tunneling implies the perfect tunneling of relativistic particles through large potential barriers. If a potential barrier exceeds a certain energy value (the electron's rest energy $E=mc^2$), the transmission probability of an incoming electron is only weakly depending on the height and width of the barrier. The transmission probability is 100% in the case of really high potential barriers. This is fundamentally different from the conventional tunneling of non-relativistic particles where the probability of transmission is exponentially decaying with increasing barrier height. The Klein tunneling can be explained by the fact that strong potentials that are repulsive for electrons, are attractive for its relativistic antiparticles or positrons. The role of this positron in graphene is fulfilled by the holes. Electrons and holes in graphene are interconnected analogues to charge-conjugation symmetry in QED. This is a result of graphene's crystal symmetry with two sublattices. When an electron encounters a potential barrier it aligns with its positron and tunnels through the barrier, since this barrier can be seen as a potential valley for the positron. This tunneling is dependent on the incidence angle of the incoming particle. Perfect tunneling occurs only at specific resonance conditions. However, perfect tunneling occurs always at angles close to the normal incidence. [42,55,58].

Graphene provides a unique platform to test the Klein paradox. Without graphene, the observation of Klein tunneling is not possible since the creation of suitable potential barriers requires enormous electric fields. In graphene samples this barrier does not have to be this large. As a consequence, the first experimental observations of the Klein paradox in graphene are a fact [59,60]. Klein tunneling was observed through potential barriers formed by graphene p-n junctions.

The electronic properties of bilayer graphene are already very different from single layer graphene. Bilayer graphene is a semimetal according to its electronic band structure and this in contrast to the zero-gap semiconductor properties of single layers. The band structure of bilayer graphene around the Fermi energy at the K point is parabolic compared to the linear spectrum of single layer graphene. Valence and conduction bands in bilayer graphene have a very small overlap of 1.6 meV and only along the ΓK direction in the Brillouin zone. This band overlap increases with the number of stacked layers and the difference with the band structure of bulk graphite becomes already smaller than 10% when more than 10 graphene layers are involved [45].

Bilayer graphene also shows a unique QHE where the Hall plateaus occur at integer values and the zero-level plateau is absent [44,61]. This is shown in the inset of Figure 1-7. Theoretical analysis predicts a Klein tunneling in bilayer graphene that is different from single layer graphene. Although there is perfect tunneling at specific incidence angles, there is perfect reflection of particles for angles close to the normal incidence [58].

Mechanical properties

The extraordinary characteristics of graphene are not restricted to electrical properties. Graphene is also extreme in its mechanical properties as it is the strongest material ever measured. Numerical investigations already predicted that the intrinsic strength of graphene is unmatched by any other material (except for CNTs) [62,63]. They calculate a Young’s modulus of 1 TPa, a Poisson ratio of 0.186 and a maximum stress of 120 GPa. These mechanical properties are confirmed by experimental work. Mechanical properties of graphene are mostly tested by indenting suspended graphene sheets with atomic force microscopy (AFM) tips [64-67]. Measurements on single layers confirm the Young's modulus of 1 TPa and yield an elastic stiffness of 340 N/m and an intrinsic strength of 130 GPa [64]. Although it is believed that single layer graphene is very susceptible to folding and scrolling, freestanding sheets of graphene supported only by one side were observed [68]. Graphene can extend freely for 10 µm without support illustrating its extreme stiffness. To compare, a sheet of paper with similar stiffness would extend freely for 100 m. This behavior is only observed in gas atmosphere though. Graphene sheets do fold and scroll in liquid environment.

Theoretical [69] and experimental work [70] have shown that graphene sheets are impermeable to standard gases, including the small helium gas atoms. Graphene nanoballoons can withstand pressure differences larger than one atmosphere [70]. Tests with these nanoballoons gave an elastic constant of 400 N/m and a surface tension of 1 N/m. The resonance frequency of these membranes can be controlled by the pressure inside the balloon. This made it possible to perform a measurement of the mass of a graphene sheet. Bunch and coworkers determined the mass of their graphene to be 0.96 $\mu g/m^2$. The fact that this is 30 % higher than the theoretical value is probably due to adsorbed species.

Thermal properties

Theoretical studies suggested a very high thermal conductance of graphene sheets [71-73]. The thermal conductivity in graphene is described as ballistic and isotropic. The thermal conductivity has two contributions, thermal conductance of electrons/holes and phonons. In intrinsic graphene, with the Fermi energy located exactly between the valence and conduction band, thermal conductivity is dominated by the phonon conductance, proportional to $T^{1.5}$. Thermal conductance by electrons and holes in this case varies with the square temperature. In the case of an applied gate voltage, and consequently a shifted Fermi energy, the electron or hole thermal conductance becomes the most important factor at low temperatures. The electron or hole thermal conductance changes linearly with temperature at low temperatures [71].

This extreme thermal conductivity of graphene was confirmed experimentally via Raman spectroscopy [74]. The G peak and 2D-bands of graphene in Raman spectroscopy are temperature-dependent [75]. As local temperature of a graphene sheet can be raised by the laser power of the Raman excitation it is possible to determine the thermal conductivity. This noncontact measurement on suspended graphene yielded thermal conductivities of about 5000 W/mK. This value is similar to the upper limit for CNTs and higher than any other known material.

Optical properties

Freestanding graphene has an optical transmittance of 97.7 % and a reflection of less than 0.1 %. Furthermore, the optical transmittance is independent of wavelength [76,77]. Graphene has an absorption coefficient of 301.655 cm^{-1} [78] and a complex refractive index of $n = 2.0 - 1.1i$ in the visible range [79]. The opacity or absorption of 2.3 % of white light is relatively high for a single atomic sheet. This is the result of graphene’s unique electronic properties. Each layer that is added to a stack of graphene sheets gives an extra opacity of 2.3 % as shown in Figure 1-8.

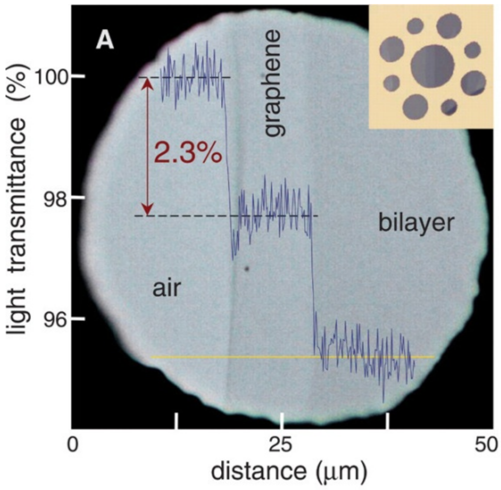

Figure 1-8. Light transmittance of graphene and bilayer graphene spanning a 50 µm hole in a metal support. Each single layer absorbs 2.3% of transmitted white light. The solid horizontal line indicates the scan position for the transmittance profile. A lower magnification of the setup is shown in the inset [77].

The optical transparency of graphene is actually defined solely by the fine structure constant (α). This is a fundamental physical constant that describes the strength of the interaction between photons and relativistic electrons in QED. It is defined by $\alpha = e^2/\hbar c \approx 1/137$ with e the electron charge, ħ the reduced Planck constant and c the speed of light. Graphene absorbs a fraction $\pi\alpha$ of white light, corresponding to 2.3 %. Graphene provided a simple platform to determine this otherwise hardly measurable fundamental constant. It was observed however that this universal behavior becomes anomalous for photon energies lower than 0.5 eV, due to doping and finite temperature effects [80].

Luckily for researchers, graphene shows a remarkably good optical contrast when placed on specific substrates. This contrast enables researchers to locate the ultrathin graphene and investigate its morphology with a regular optical microscope. The origin of this contrast lies in an increased optical path combined with the abovementioned strong opacity of graphene. This results in an interference color that is slightly different from the bare substrate. The best known and mostly used substrate is Si with a 300 nm SiO_2 layer on top. Other thicknesses of SiO_2 like 90 nm , 280 nm and 465 nm are also used [79,81-84].

Besides Si with SiO_2, other substrate materials were tested. Some examples are Si with 68 nm Si_3N_4 [85], Si with 72 nm Al_2O_3 [86] and SiC [87]. Optical contrast rapidly decreases to zero when substrate thicknesses deviate from these specific interfering thicknesses.

1.2.5. Graphene production

Mechanical exfoliation

Mechanical exfoliation actually encompasses a few methods that are very similar. There is the Geim method [1], also called the Scotch tape method and there is the drawing method [46]. Both are top-down approaches and they start from graphite. As described above, the Geim method was the first successful method to produce freestanding graphene. The Geim method used today is further simplified as compared to the first description, see historical overview. The "modern" version starts from clean HOPG or graphite ore and thin layers of graphitic material are peeled off directly from the unprocessed HOPG or ore. These thin layers are made even thinner by folding and unfolding the tape a number of times. When the sheets are thin enough, they are transferred to a Si substrate. This is done by pressing the tape with flakes onto the substrate, followed by gently rubbing over the tape to remove trapped air bubbles. Usually, a special kind of tape, for wafer dicing, is used instead of the regular Scotch tape. This tape leaves much less residue on the substrate and facilitates the transfer of flakes from the tape to the substrate.

The drawing method involves the rubbing of graphite onto a substrate. This rubbing, like writing with a pencil, leaves thin flakes on the substrate. This method is not used often as it yields less graphene flakes than the Geim method. Other 2D materials, like hexagonal boron nitride and dichalcogenides, were also produced by this method [46].

Both of these approaches deposit a bunch of flakes with a wide variety of lateral dimensions and thicknesses. One has to search for true graphene sheets, or if desired few-layer graphene, under the optical microscope. An example of a graphene sheet produced by the Geim method is given in Figure 1-9. Searching for graphene is a time-consuming task because a substrate of cm^2 dimensions has to be scanned slowly to detect a faintly visible sheet, mostly with maximum dimensions of a few tens of μm^2. Although time-consuming, this method still gives the best quality graphene samples, regarding crystal quality and physical properties.

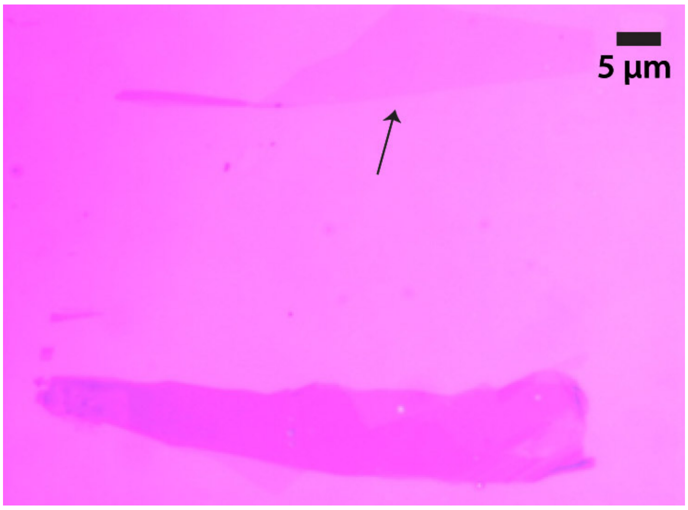

Figure 1-9. Optical microscopy image of a graphene flake (indicated by the arrow) produced by the Geim method. The flake is lying on top of a Si substrate with 300 nm SiO_2. The flake in the lower region of the image is about 3-5 layers thick.

Chemical oxidation and reduction

The chemical oxidation and reduction method is the best technique for large scale production of graphene. Unfortunately, the quality of reduced graphite oxide is fairly poor. A lot of the unique electronic properties of graphene are not preserved after reduction of oxidized graphene.

Graphite can be oxidized by the Hummers method [88] whereby an oxidizing mixture of potassium permanganate ($KMnO_4$), sodium nitrate ($NaNO_3$) and sulfuric acid (H_2SO_4) is used. Other oxidation methods are the Brodie method [10], with potassium chlorate ($KClO_3$) and fuming nitric acid (HNO_3), and the Staudenmaier method [11], with $KClO_3$, HNO_3 and H_2SO_4. Graphite oxide contains a variety of functional groups, like epoxy, hydroxyl and carboxyl groups [89,90]. An illustration of graphene oxide is given in Figure 1-10.

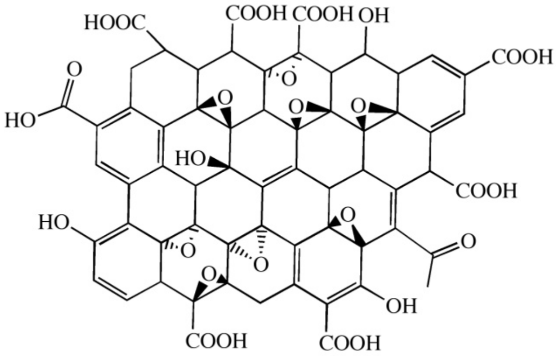

Figure 1-10. Illustration of possible graphene oxide structure. [91]

The functional oxygen containing groups render the graphite oxide hydrophilic. This hydrophilicity together with the intercalation of the used salts make graphite oxide dispersible in many solvents, including water [92]. Graphite oxide exfoliates in few-layer graphene oxide, but mostly not in monolayers. Furthermore, dispersions of graphene oxide are not very stable in most solvents. Heat treatment [89] and ultrasonication [93] are used to enhance exfoliation. Graphene oxide can be chemically modified to improve the stability of dispersions [93-95].

Graphene oxide is an electrical insulator and needs to be reduced again to restore the conducting properties. As mentioned above, the electronic properties of reduced graphene oxide are very different from pristine graphene because reduction cannot fully restore the sp^2 structure of graphene. Reduced graphene oxide has a strongly decreased conductivity and carrier mobility for example [96]. Graphene oxide is mostly reduced by hydrazine (N_2H_4) [94,97-100]. Other possible reducing agents are hydroquinone [101] and sodium borohydride [102]. Graphite oxide can also be reduced by elevated temperatures. In this case, reduction causes the simultaneous exfoliation of the graphite oxide through elevating gas pressures between the layers. The decomposition of the oxygen containing groups produces gas bubbles that drive the layers apart [89,103].

This graphite oxide reduction method can be combined with a Langmuir-Schaefer approach to deposit single layer graphene with tunable coverage of hydrophobic surfaces [104]. A dispersion of graphene oxide in water was injected with octadecylamine, a long-chain surfactant. The octadecylamine bonds to the graphene oxide and forms a hybrid Langmuir film at the air-water interface. The density of the hybrid layer can be controlled by changing the surface area of the Langmuir bath. The surfactant molecules with the attached graphene oxide pack closer together when the surface tension is raised. Deposition is realized by a Langmuir-Schaefer method, meaning slowly dipping the substrate horizontally in the bath. The hydrophobic chains of the octadecylamine-graphene oxide are attracted by hydrophobic substrates and the hybrid Langmuir film is transferred to the substrate, see Figure 1-11. After reduction with hydrazine, thermal annealing and healing of defects with ethylene gas, a high quality film of monolayer graphene sheets is formed, with carrier mobilities of 12 cm^2/Vs.

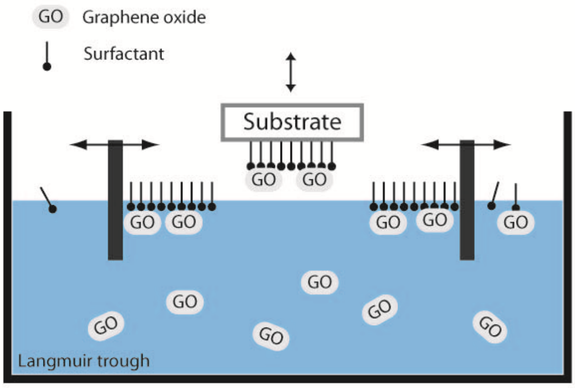

Figure 1-11. Schematic representation of the Langmuir-Schaefer method

Liquid-phase exfoliation

Liquid-phase exfoliation of graphite is another method that is potentially suitable for large scale production of graphene. In contrast to the previous method, the graphite is not oxidized or otherwise covalently functionalized. The electrical properties however are similar to reduced graphite oxide. Another drawback of this method is the relatively small size of graphene flakes, in the order of a few micrometers. This method involves the exfoliation of graphite in certain solvents, like N-methylpyrrolidone (NMP), N,N-dimethylacetamide (DMA) and γ-butyrolactone (GBL), for which the surface energy matches that of graphene. The exfoliation is aided by ultrasonication. Almost all material is exfoliated in layers with a thickness of less than 5 atomic sheets and 1 wt% of the starting material is exfoliated into single layer graphene [105]. Graphite can also be exfoliated in water-based solutions with surfactants [106].

Thermal decomposition of silicon carbide

Thermal decomposition of silicon carbide (SiC) is a form of epitaxial growth of graphene. It is proposed as a route for large scale synthesis of wafer-size graphene. SiC wafers are heated to temperatures between 1250 °C and 1450 °C in vacuum for a couple of minutes. This heat treatment evaporates the Si atoms and graphitizes the carbon to form thin layers of graphene and few layer graphene (FLG) [107-110]. The method can be improved by heating the SiC wafers in a near atmospheric pressure of argon gas (900 mbar). As a consequence, the temperature at which Si starts to evaporate is elevated. The surface of the SiC wafer at this elevated temperature is much smoother compared to temperatures used with vacuum conditions. Therefore, when the graphene layer starts to grow, at 1650 °C, the surface underneath has an improved morphology. This results in much larger domains (2 x 50 μm^2) and better uniformity in layer thickness [111].

Although continuous films were grown with wafer-size dimensions, they are like a polycrystalline sheet consisting of different domains. The resulting material is of fairly good quality with carrier mobilities in the order of 1000 - 2000 cm^2/Vs [107,111] and even 20000 - 30000 cm^2/Vs [108,109] for patterned structures with nanowire dimensions. Disadvantages of this technique are non-homogeneous layer thickness and small domain sizes. Thermal decomposition of SiC mostly gives a film consisting of monolayer and few-layer graphene. SiC is a wide bandgap (3 eV) semiconductor that is insulating enough to avoid the need for transfer of the grown graphene to other insulating materials. Single crystal SiC wafers are used in most experiments. The Si-terminated face or the C-terminated face can be used to grow graphene. Growth on a C-terminated face generally gives larger domain sizes (~ 200 nm) compared to Si-terminated planes (30 – 100 nm) [112]. Furthermore, stacks of graphene grown on C-terminated faces are rotationally disordered, meaning that there is no stacking order and the layers show only weak electronic coupling. Nevertheless, this resulted in exceptional electronic quality and a carrier mobility of 250000 cm^2/Vs inside a stack of 100 layers [113]. However, external electric fields are screened by the outer layers of the stack, making it unattractive for a lot of electronic applications [114].

Epitaxial growth on metal surfaces

The epitaxial growth of graphene on metal surfaces is related to the epitaxial growth on SiC wafers. This method is maybe the most promising method for industrial production of good quality wafer-size graphene, although it is still difficult at the moment to produce a layer with uniform single atom thickness. An additional problem can be the need to transfer graphene to insulating substrates or to remove the metal layer in order to use graphene for electronic applications.

Graphene is grown on metal surfaces by chemical vapor deposition (CVD) via decomposition or segregation. Decomposition involves the cracking of carbon containing molecules, like ethylene, that are adsorbed on the surface. These molecules can be adsorbed at room temperature, followed by heating to start decomposition, or they can directly adsorb and decompose on hot substrates. Segregation means diffusion of dissolved carbon to the metal surface at elevated temperatures. The carbon atoms can be present as natural impurities or metal substrates can be doped with carbon at elevated temperatures.

Graphene or FLG were grown on a variety of transition metals. Some examples are nickel (Ni) [115-119], copper (Cu) [115,120], ruthenium (Ru) [121,122], platinum (Pt) and palladium (Pd) [123]. Ni and Cu show the most potential for industrial application, as they are relatively cheap and mobilities around 4000 cm^2/Vs were measured [116,120].

The transfer of the grown graphene or FLG from the metal surface to an isolated substrate is possible through the wet chemical etching of the metal layer in the presence of a support layer for the graphene. After etching, one can handle and stamp the support material with the graphene. A graphene layer grown on a Ni foil for example can be transferred by etching the Ni layer with HCl in the presence of a poly(methyl methacrylate) (PMMA) layer. The latter serves as a capture and support layer for the graphene. Next, the graphene can be stamped onto another substrate and the PMMA layer can be dissolved with acetone [117].

The previous method can be adapted to avoid rupture, tearing and wrinkling. Before the PMMA is removed with acetone, there is a redeposition of fresh liquid PMMA which partly dissolves the "old" cured PMMA. This results in a mechanical relaxation of the graphene attached to the PMMA, leading to a better transfer to the target substrate [124].

Bottom-up chemical synthesis of nanoribbons

An entirely new method was developed to fabricate graphene shaped into atomically precise nanoribbons [125]. It is a bottom-up approach that starts from precursor monomers. The production starts with thermal sublimation of halogenated monomers, like for example 10,10-dibromo-9,9-bianthryl, onto a solid gold or silver substrate. Upon sublimation, there is a dehalogenation of the monomers to form surface-stabilized biradicals. A thermal activation step causes the biradicals to diffuse across the solid substrate and polymerize with each other through radical addition. Polymer chains are formed with the orientation of the functional groups determining the shape of the chain. This can be linear or zigzag for example. A second thermal activation starts a surface-assisted cyclodehydrogenation, resulting in a graphene nanoribbon. The reaction scheme is illustrated in Figure 1-12.

Graphene nanoribbons can also be made by unzipping CNT, for example via oxidation [126,127] or plasma etching [128]. Alternatively, graphene nanoribbons are produced top-down by lithographical processing of graphene sheets.

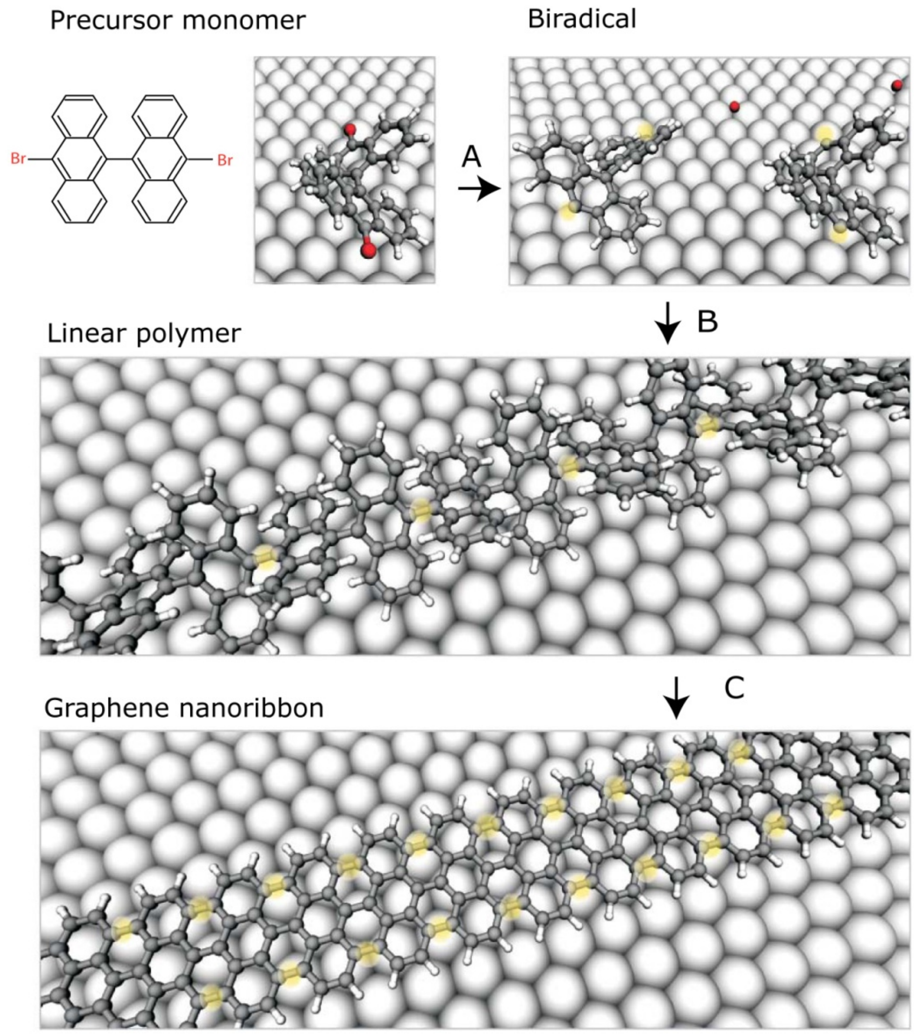

Figure 1-12. Bottom-up fabrication of graphene nanoribbons starting from precursor monomers (10,10-dibromo-9,9-bianthryl). (A) Dehalogenation of adsorbed monomers. (B) Diffusion and polymerization of biradical species upon thermal activation. (C) Second thermal activation initiates cyclodehydrogenation to form graphene nanoribbons. Adapted from [125]*.*

1.2.6. Chemical modification and functionalization

The main purpose for the chemical modification of graphene and FLG is to improve their solubility as graphene itself is highly hydrophobic and therefore insoluble in most solvents. Another reason to modify graphene is opening and tuning of the bandgap. Pristine graphene is a zero-gap semiconductor and a bandgap needs to be introduced in order to develop transistors with good on-off ratios. The covalent chemical functionalization of graphene almost always involves the changing from sp^2 hybridization to sp^3 hybridization and from conducting to insulating properties, depending on the scale of functionalization. Chemical modification can also induce doping of the material. Coupling of electron-withdrawing functional groups, like oxygen groups, induce p-doping. On the other hand, electron-donating functional groups, like nitrogen groups, cause n-doping. Also, the development of graphene-based biosensors requires the functionalization of graphene and FLG. Biological receptor molecules need to be immobilized on the surface or edges of graphene and graphene-like materials.

At present, most of the chemical modifications and functionalizations deal with graphene oxide. Very little work has been done on pristine graphene, probably due to the fact that the sp^2 carbon structure is rather inert to chemical reactions. It is expected that some chemical reactions have a preference for zig-zag or arm-chair conjugated tracks [129]. Furthermore, once a covalent bond is formed at a certain point in the graphene lattice, adjacent sites will show an increased reactivity due to the presence of unpaired electrons. The conjugated bond structure can be opened like a zipper in this way.

The chemical modification of graphene is based on CNT chemistry. Like CNTs graphene can be functionalized covalently or non-covalently. Both of these methods will be shortly described.

Covalent functionalization

A special form of covalently functionalized graphene is graphane. The latter is a graphene sheet that is fully saturated with hydrogen atoms. Every carbon atom is covalently bonded to a hydrogen atom with the two sublattices bonding on opposite sides [130,131]. An artist's impression is given in Figure 1-13. After the prediction of the existence of graphane it took some time to produce the first graphane sheet. This was accomplished by exposing a suspended graphene sheet to a cold hydrogen plasma at low pressure for two hours. The transformation of graphene into graphane is accompanied by the conversion of sp^2 bonds into sp^3 bonds and electronic transformation into an insulator. The hydrogenation is reversible and electronic structure can be restored to a large extent [131]. The hydrogenation of graphene could be used for further attachment of organic moieties.

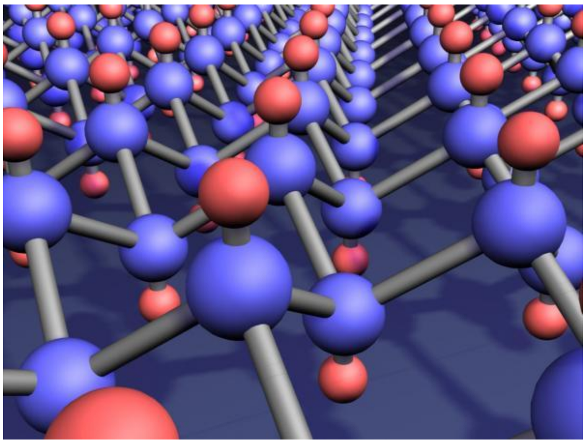

Figure 1-13. Artistic impression of graphane. Small and large spheres correspond to hydrogen atoms and carbon atoms, respectively. The proposed structure is one with crystalline order. [132]

A fully saturated analog to graphane also exists where the place of hydrogen is taken by fluorine atoms. This is called poly-(carbon monofluoride) with the chemical formula CF [133].

The functionalization of graphene with diazonium salts is one of the very few functionalization methods that can be applied to pristine graphene, although it is also used with reduced graphene oxide [97,102,134-136]. Diazonium salts contain a very reactive N_2^+ group which acts as a leaving group when a covalent bond is formed. Benzenediazonium species are used to functionalize graphene. A proposed reaction scheme is as follows: first the diazonium adsorbs on the graphene. Second, graphene spontaneously donates an electron to the electrophilic diazonium group. An N_2 molecule splits off and leaves behind an aryl radical. This aryl radical then binds to the unpaired electron that is left behind on the graphene after it donated one electron. Finally, a C-C bond is formed between the benzene ring and graphene [137].

It should be noted however that the covalent character of the diazonium coupling on graphene is subject of debate. Some results suggest that the bond is not covalent but stronger than regular van der Waals adsorption [138]. Other results indicate that both covalent binding and adsorption occur with covalent binding dominating on graphene, and especially at graphene edges, and adsorption dominating on FLG [134].

Other covalent functionalizations use graphene oxide as base material. The oxidation of graphene was described in the section on graphene production. A variety of covalent reactions can be performed on oxidized graphene sheets. Each kind of oxygen containing group can be used for a specific reaction.

The epoxy groups of graphene oxide can react with sodium azide (NaN_3) to yield azide functionalities that can subsequently be reduced with $LiAlH_4$ to get amino groups or they can be used to perform click chemistry [139]. This is shown in Figure 1-14. Another possibility to functionalize the epoxy groups is a nucleophilic ring-opening reaction between the epoxy groups and amine-terminated ($R\text{-}NH_2$) target molecules [140,141].

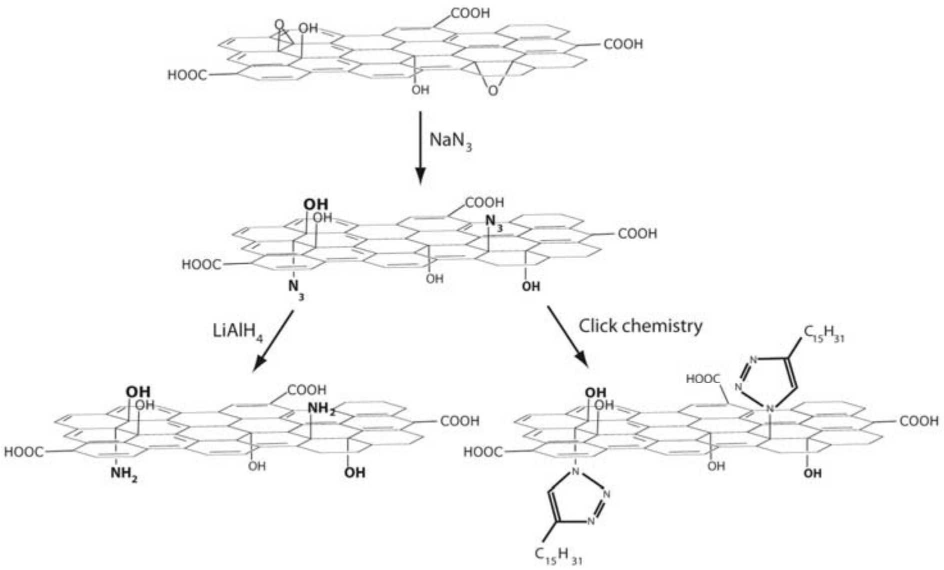

Figure 1-14. Reaction of graphene oxide with sodium azide (NaN_3). Azide functionalities can be reduced with lithium aluminium hydride ($LiAlH_4$) to aminogroups (left) or used in click chemistry (right).

Carboxylic acid groups can be esterified via carbodiimide activation of the carboxylic acid and reaction with hydroxyl groups [142,143]. Alternatively, an intermediate with acyl chloride groups, generated by adding thionylchloride ($SOCl_2$), can react with hydroxyl groups to form an ester bond [142]. Graphene oxide was functionalized with poly (vinyl alcohol) (PVA) chains for example.

Exposure to isocyanates leads to reaction of the hydroxyl groups on the surface as well as carboxylic acid groups on the edges of graphene oxide. Hydroxyl groups react into carbamate esters (RNHCOOR’) and carboxylic acid groups into amides (RC(O)NHR’) [93,95,144], as shown in Figure 1-15.

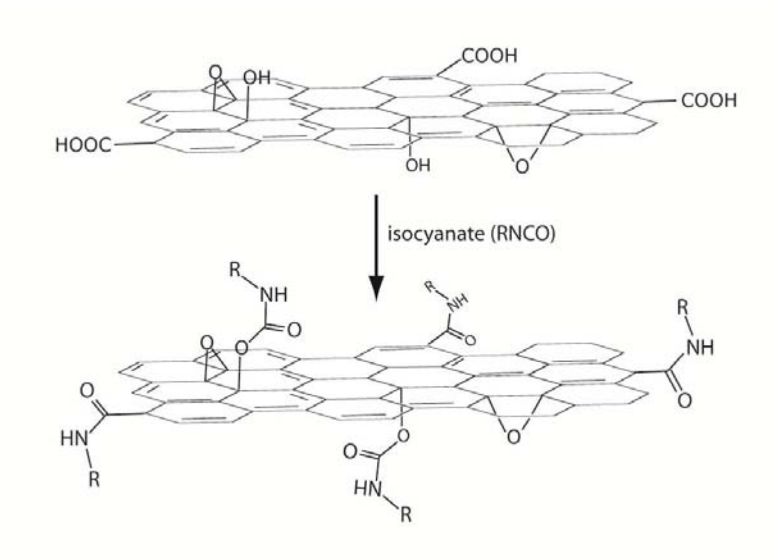

Figure 1-15. Reaction of graphene oxide with isocyanate to transform hydroxyl and carboxyl groups into carbamate esters and amides, respectively.

Non-covalent functionalization

Non-covalent functionalization, like covalent binding, is mainly used to improve the solubility of graphene or graphene oxide. The great advantage over covalent functionalization is that non-covalent modifications do not disrupt the sp^2 structure of graphene. This way, graphene can be solubilized without losing physical properties like its electrical conductivity. Non-covalent functionalization is based on hydrophobic interactions or π-π interactions. This means that aromatic (parts of) molecules can interact with the aromatic structure of graphene through strong π-π interactions [145]. The aromatic ring structures stack on graphene like two or more graphene sheets stack on each other. Functionalized pyrene molecules, like pyrene butanoic acid, are often used to decorate graphene planes to improve their solubility [146-148]. Other aromatic molecules that can be used are perylene derivatives [147,149].

Graphene and graphene oxide can also be functionalized with DNA in order to develop a biosensor [150,151], dope graphene through negative potential gating [2] or protect the DNA from enzymatic cleavage [152]. The interaction between DNA and graphene is due to van der Waals forces, with only a limited contribution of the aromatic rings [153].

1.2.7. Applications

The reason for the huge amount of interest in graphene and graphene-like materials is the myriad of potential applications for these remarkable structures. The unique electronic, mechanical, thermal and optical properties of graphene-like materials may contribute to large improvements of existing technologies.

Maybe the highest expectations for graphene-like materials are in transistor development. Graphene could enable the production of transistors at the nanometer scale due to its stability, high signal-to-noise ratio and conductivity, even in the nanometer range. Graphene is possibly the material of choice to prolong the lifetime of Moore's law [42]. This law states that the amount of transistors on a given chip area doubles every 2 years. It is expected that the transistor density will reach a limit at some point and Moore's law will not apply anymore. Graphene could extend the period of validity of this law. A lot of work has already been done on graphene-based field effect transistors [44,54,154-156]. Graphene-based transistors with very fast operating frequencies of 100 GHz were developed [154]. Furthermore, a single-electron transistor was developed with dimensions of only a few hundred nanometers. It is even possible to decrease this size down to quantum dots of about 10 nm [155]. It should be noted however that graphene's zero gap band structure is detrimental for transistor on-off ratios as there is always a minimal conductance in pristine graphene. Introducing a bandgap can solve this problem and increase the on-off ratios significantly [157]. Bandgap introduction can be realized by chemical modifications, restriction of lateral dimensions to nanoribbons or by interaction with substrates. FET structures made from graphene nanoribbons, smaller than 10 nm wide, were fabricated and showed I_{on}/I_{off} ratios of about 10^7 [158].

Graphene-like materials also show great potential as transparent conductive electrodes. The high conductivity and optical transmittance of graphene makes it a good candidate to replace traditional materials such as indium tin oxide (ITO). The need for alternatives to ITO is growing as indium sources are shrinking and therefore prices are escalating. Furthermore, ITO is not suited for future flexible electronics due to its decreasing conductivity after bending [159]. A lot of progress has been made in the production and handling of graphene and graphene-like materials, making its commercial use more and more relevant. A lot of research has already been done on the use of graphene in transparent conductive films [124,160,161]. It has been used for example in photovoltaics [147,162,163], organic light-emitting diodes (OLEDs)[164] and liquid crystal devices (LCDs) [165].

Graphene has also proven to be useful in sensor devices. Binding or adsorption of chemical [5,166-168] and biological species [169,170] can evoke a measurable change in electrical properties, due to for example charge transfer or gating effect. Its high surface-to-volume ratio and low electrical noise, related to its metallic conductivity and crystal quality, are great advantages in the development of highly sensitive detection devices. It was demonstrated that graphene devices could easily detect 1 part per million (1 ppm) concentrations of gases like ammonia (NH_3) and carbon monoxide (CO). It was even possible to detect the adsorption of individual gas molecules [5]. Other work showed the detection of chemical warfare agents and explosives at the parts per billion (ppb) concentration level [166]. Furthermore, different biological species like bacteria [169], DNA [169] and proteins [170] can be detected electrically with graphene-based devices. Sensing of target molecules is not limited to electrical response as shown by the detection of DNA strands via optical methods [151,171]. This was based on the quenching of fluorescing labels upon adsorption on graphene's aromatic structure.

Other possible applications of graphene-like materials include lithium ion batteries, where graphene is used as high capacity storage medium of Li ions [172,173], ultracapacitors [174,175], hydrogen storage [176], electrochemical resonators that can be used as mass, force and charge sensors [177], support films for high resolution transmission electron microscopy [178] and as fillers in graphene-polymer composites to improve mechanical and electrical properties [144,179].

Chapter 2

Characterization techniques

This chapter will describe the characterization techniques that were used in this work. Some techniques, like optical microscopy and atomic force microscopy, were used to characterize the graphene-like materials while others, such as fluorescence based measurements and X-ray photoelectron spectroscopy, were used to investigate functionalization of these graphene-like materials. A brief theoretical background of each technique will be given, followed by the specific contribution of the technique to this research. The precise apparatus that were used in this work will also be given.

2.1 Optical microscopy

Optical microscopy or conventional light microscopy utilizes a specific set of lenses to focus a beam of visible light on a sample and magnify an image from the sample. Optical microscopy is of special importance in graphene research since it gives a rather good indication of the thickness of flakes. A trained eye can distinguish between single layer, bilayer and multiple layer graphene when deposited on specific substrates. This was already mentioned in the section on the optical properties of graphene. Optical microscopy was also used to quickly investigate the lateral dimensions of flakes, coverage of a substrate with flakes or to check lithographically made patterns for example.

An example of an optical image of a flake is given in Figure 2-1. This flake was deposited via the Geim method on a Si substrate covered with 300 nm SiO_2. The area of the flake that consist of only one single layer is denoted by "A" and a small band of bilayer graphene is indicated by "B". The following letters indicate parts with increasing thickness with G being the thickest part of the flake. G corresponds to an approximate thickness of 50 layers.

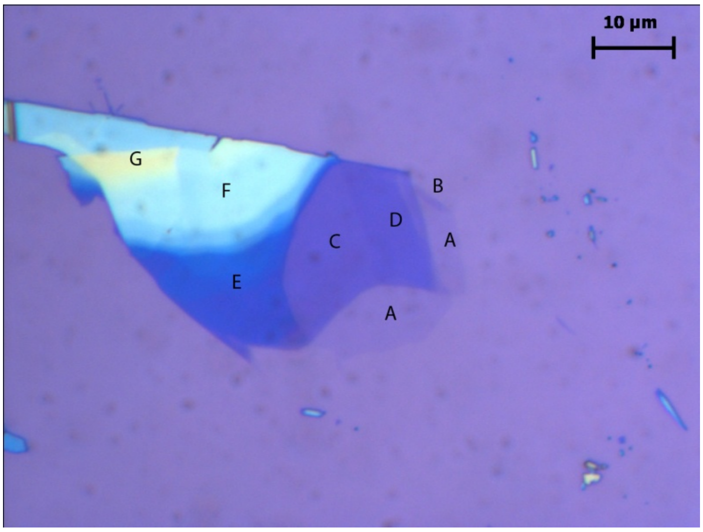

Figure 2-1. Optical microscopy image of a flake on Si/SiO$_2$ 300 nm. Letters indicate some parts with different thicknesses with "A" the thinnest and "G" the thickest part. "A" indicates single layer graphene, "B" bilayer graphene and "C" marks an area consisting of at least three layers. Different steps in thickness can be seen in the transition zone from "E" to "F". The image was taken with a 100x objective.

The optical microscope that was used in this work is an inverted microscope, type Axiovert 40MAT from ZEISS, equipped with 5x, 10x, 20x, 50x and 100x objectives. A BrightLine HC 560/14 bandpass filter from AHF analysentechnik AG (Tübingen, Germany) was sometimes used to improve contrast. However, as this filter only transmits green light, the color indication for flake thickness is lost by using it.

2.2 Raman spectroscopy

Raman spectroscopy is an analysis technique that is based on Raman scattering or the Raman effect. When light falls onto a sample, most photons are elastically scattered and a very small part is inelastically scattered. Elastic scattering means that the scattered photon has the same energy (frequency) as the incident photon whereas there is a difference in energy for inelastic scattering. Elastic scattering, also called Rayleigh scattering, is filtered out or ignored and the inelastic scattering, or Raman scattering, is used for analysis. Photons are inelastically scattered when they interact and exchange energy with the material they fall onto. Energy exchange is possible through the coupling between the incident light and vibrational, rotational and electronic energy levels of the target molecules. Raman spectroscopy measurements use monochromatic light to irradiate a sample and the frequency shift after scattering is measured. The frequency can shift to lower (Stokes shifted scattering) or higher (Anti-Stokes shifted scattering) energy depending on the vibrational state before excitation. At room temperature, most vibrational states are in the ground state resulting in Stokes shifted scattering. At elevated temperatures, there are more excited vibrational states that scatter incoming light, contributing to Anti-Stokes shift. Since Stokes shifted peaks are more intense than Anti-Stokes shifted peaks, most Raman studies focus on the Stokes shifted scattering.

The frequency shift corresponds to certain excitation modes of the investigated material. These excitations are dependent on the atoms that constitute a molecule, the bonds between them and the symmetry of the molecule. Only certain excitations are Raman active and contribute to the Raman spectrum. Other complementary techniques, like infrared spectroscopy, can be used to investigate excitations that are not Raman active [180,181]. Elaborate symmetry-based selection rules exist to determine if a certain vibration is Raman active and/or infrared active. As this is beyond the scope of this text, one can also state the selection rules as follows: to be infrared (Raman) active, a vibration must change the dipole moment (polarizability) of the molecule. Raman spectra are presented as frequency shifts in wavenumber (cm^{-1}) with their corresponding intensities. The wavenumber is determined by the following equation:

$$\nu(cm^{-1}) = \left(\frac{1}{\lambda_{ex}(nm)} - \frac{1}{\lambda_{scat}(nm)}\right).10^{7} \tag{2.1}$$

Most carbon structures, including graphene, have a distinct Raman signature and Raman spectroscopy is one of the most suitable techniques to determine the number of layers in thin stacks of graphene. Raman spectroscopy can rather clearly differentiate between single layer and bilayer graphene. The most important Raman peaks associated with graphene are the so called G peak (at

~1580 cm^{-1}) and 2D peak or band (at ~ 2700 cm^{-1} for λ_{ex}= 514 nm and at ~ 2650 cm^{-1} for λ_{ex}= 633 nm). The G peak is linked to the doubly degenerate zone center E_{2g} mode, which is the stretching of the strong intralayer bonds, see Figure 2-2. The 2D band is the second order of zone-boundary phonons. Graphene edges and defective graphene also possess a D peak (at ~ 1350 cm^{-1}) linked to disorder-induced first order scattering. The G peak can show a shoulder, called the D′ peak (at ~ 1600 cm^{-1}), related to the D-band and linked to finite size effects and lattice defects [182-186].

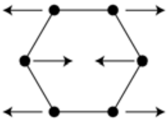

Figure 2-2. G vibration mode with E_{2g} symmetry. Adapted from [187].

The Raman spectra for graphene and graphite are shown in Figure 2-3 (A). The G peak and 2D band are clearly shown and a first difference between the spectra of graphene and graphite can be seen in the intensity ratio ($I_{(G)}/I_{(2D)}$) of both peaks. This intensity ratio is smaller than 1 for graphene and larger than 1 for graphite.

A closer look at the G peak (see Figure 2-3 (B)) shows a shift in Raman frequency with each added layer up to a stack of 5 layers. The difference in Raman shift between graphene and a stack of 5 layers is about 5.5 cm^{-1}. The 2D band also shifts upwards with increasing number of layers. Furthermore, the 2D band broadens and changes shape with increasing thickness, see Figure 2-3 (C).

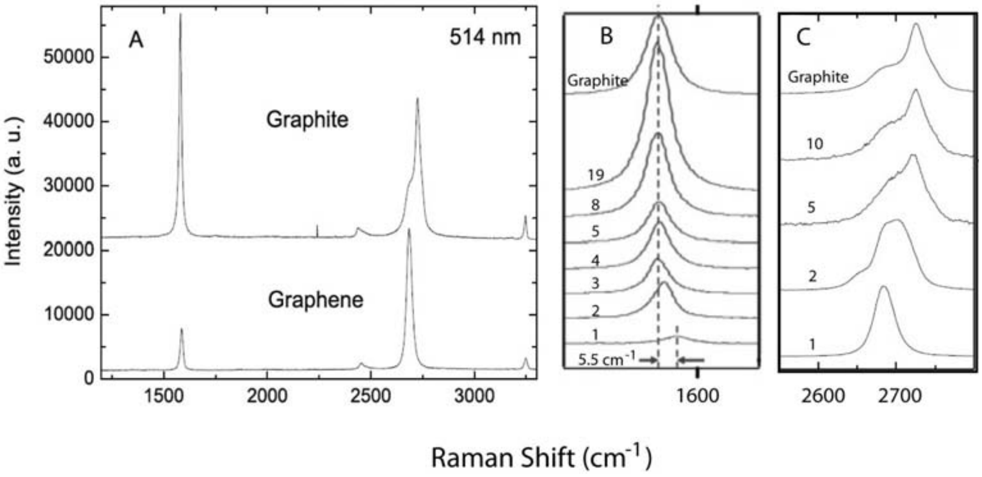

Figure 2-3. (A) Raman spectra of graphene and graphite. (B) Evolution of the G peak in function of the number of layers, indicated on the left. The G peak shifts by about 5.5 cm^{-1} when the thickness changes from single layer to 5 layers. (C) Evolution of the 2D peak in function of number of layers. All spectra are taken at λ_{ex} = 514 nm. Image is adapted from [184,185].

The Raman measurements presented in this work (Chapter 4) were performed at IMEC by Dr. Mirco Cantoro. Micro-Raman spectra were collected with a LabRAM HR Jobin-Yvon spectrometer (1.5 cm^{-1} spectral resolution), coupled with a 633 nm laser excitation and 100x microscope objective (~ 1 μm^2 spot size). A laser power of ~ 1 mW (corresponding to < 10^5 W/cm^2 power density) was employed to minimize laser heating effects and other detrimental effects on graphene. The spot size is small enough to focus selectively on the graphene surface without illumination of the substrate.

2.3 Atomic force microscopy

Atomic force microscopy (AFM) is a scanning probe microscopy method. An AFM tip scans over a sample surface to generate a topography image of the sample. The tip is conical and very sharp (± 10 nm radius) to yield high lateral resolution profiles. This tip is attached to a cantilever which is usually made of Si or silicon nitride and fixated at one end. The free end of the cantilever can move up and down as the cantilever is flexible with a certain spring constant (in the order of 0.1 N/m and 40 N/m for contact and non-contact mode, respectively). An AFM setup is further composed of a piezoelectric stage that can move in three dimensions, a laser and a laser detector with four quadrants. The sample is mounted on the stage, which moves in the XY direction to scan the area of interest. While scanning, a laser beam is reflected off the back of the cantilever, with the tip beneath it, and captured at the position sensitive detector. If the laser spot deviates from the center of the detector a feedback-loop moves the stage to adjust it back to the 'blind spot" in the center of the detector. The magnitude of the z-displacement is saved in a computer and a profile of the sample is formed. A schematic of the working principle is given in Figure 2-4.

The origin of the displacement or deflection of the tip and cantilever are the atomic interactions between the tip and the sample surface. These interactions can be van der Waals interactions, electrostatic forces, capillary forces,…. Special tips can be used to map specific properties of the surface like magnetic tips and conducting tips to probe magnetic and conductive properties, respectively.

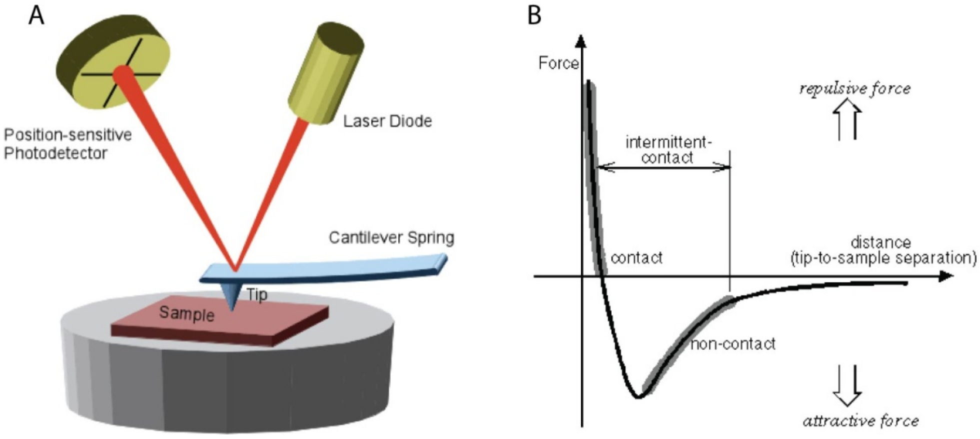

Figure 2-4. (A) illustration of the AFM working principle and setup. (B) Force-distance curve that forms the basis for the AFM operation. In contact mode there is a repulsive force between tip and sample. In non-contact mode there is attraction. [188]

An AFM can work in three different modes, depending on the distance between the tip and sample. If the tip touches the sample, it is called contact mode and the forces are in the repulsive regime, see Figure 2-4 (B). This mode is the simplest one and has the highest resolution. Two submodes are possible where the feedback loop keeps either the force or the height constant. A disadvantage of the contact mode, however, is the possibility of damaging soft samples due to high frictional forces as the tip slides over the surface. Therefore, this mode is not suitable for biological samples or other soft materials.

The AFM can also be operated in a mode where the tip is oscillating above the sample without touching the sample. This mode is called the non-contact mode and depends on attractive forces between tip and sample. The cantilever oscillates with a certain frequency and amplitude about 10 nm above the sample. Interactions between the tip and sample surface influence the oscillation. Again two different feedbacks are possible, one to keep the frequency constant and one to keep the amplitude constant. The frequency modulation allows to generate a phase image, showing the phase difference between the measured and the applied oscillation. This phase difference depends on the type of surface material and therefore gives additional information on top of the topographical info. This mode has a lower resolution but is better suited for soft samples.

A third mode, called tapping mode, is a combination of the two previous modes. The cantilever is again driven to oscillate above the surface but now with an increased amplitude. Each time the tip reaches its lowest point in the oscillation cycle, it taps the surface. This mode has an improved resolution compared to non-contact mode and does not damage fragile samples.

AFM is a straightforward technique to determine the thickness of graphene-like materials. However, it is not always easy to pinpoint the exact number of layers in thin stacks of graphene, despite the known single layer graphene thickness of 0.335 nm. Experimental errors and adsorbates on the surface can complicate the analysis. An example of an AFM image of graphene is presented in Figure 2-5 (A).

It is also noteworthy that graphite is often used as substrate material to image adsorbed biomolecules with AFM. Graphite has an atomically flat surface due its crystalline layered structure, enabling the characterization of large molecules, like DNA and antibodies, adsorbed on the surface. Figure 2-5 (B) shows an AFM image of IgG antibodies adsorbed on a HOPG surface.

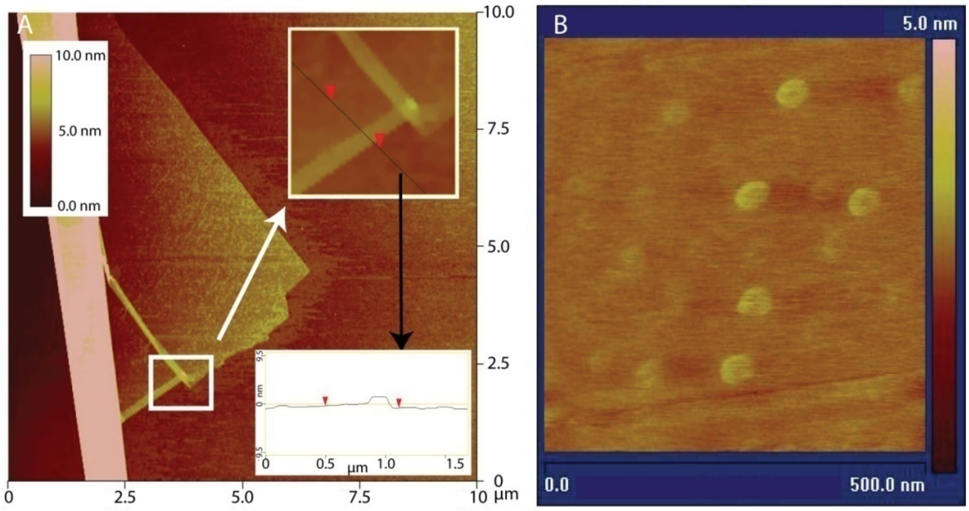

Figure 2-5. (A) AFM height image of a graphene flake. The upper right insert shows a magnification of the indicated area and the lower right insert shows the height profile along the black line, indicated in the upper right insert. The vertical distance between the red arrows is 0.416 nm, corresponding to single layer graphene. (B) AFM height image of IgG antibodies adsorbed on a HOPG surface. Both images were recorded in tapping mode.

AFM measurements in this work were performed with a Veeco Multimode microscope combined with a Nanoscope IIIa controller from Veeco Digital Instruments. Images were recorded in tapping mode. Measurements were performed by Dr. Hong Yin. Figure 2-5 (B) was recorded by the author.

2.4 Scanning electron microscopy

Another method to obtain topographical and compositional sample images is scanning electron microscopy (SEM). This method has a significantly improved spatial resolution compared to light microscopy due to the use of electrons, which have smaller wavelengths, instead of larger wavelength photons. Another advantage of SEM over light microscopy is its higher depth of focus, making it especially suitable for studying surfaces with high roughness.

A scanning electron microscope produces an electron beam via thermionic emission or field emission in an electron gun, usually made of tungsten or lanthanum hexaboride. The electron beam is accelerated by a voltage difference, focused by a set of electromagnetic lenses and scanned across the surface through scan coils. When the electron beam hits the sample, it is scattered elastically and inelastically, producing a variety of detectable signals.

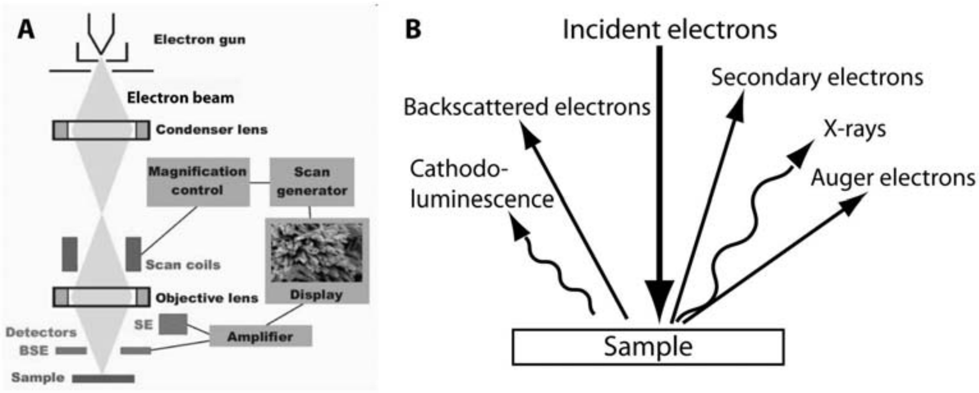

Figure 2-6. (A) Schematic of scanning electron microscope. [189] *(B) Detectable electron-sample interactions.*

Figure 2-6 (B) gives an overview of the signals that are produced by an incoming beam of electrons. Each signal requires a specific detector and gives different but complementary information about the sample. The most commonly used signals are the secondary electrons and the backscattered electrons. Secondary electrons are generated by the collision of incoming electrons and loosely bound outer electrons of sample atoms, followed by the ionization of the sample atoms. These electrons give topographical information as only electrons generated in the top layers are able to escape from the surface. These secondary electrons are detected with an Everhart-Thornley detector (ETD). Backscattered electrons are the incoming electrons that are elastically scattered and escape from the surface. These electrons have a high energy and give topographical information and compositional information of deeper sample layers. They are detected with a solid-state detector (SSD). The amount of electrons that reaches the detector depends on the local height and curvature of the sample surface. Regions that are oriented towards the detector will allow more electrons to reach the detector and will appear bright on the screen. The same holds for higher lying regions as compared to lower lying regions, resulting in a 3D-like impression of the surface.

Incident electrons can also generate X-rays, Auger electrons and cathodoluminescence, but these are less commonly used. X-rays and Auger electrons give compositional information of lower and top sample layers, respectively. X-rays are analyzed in energy-dispersive X-ray spectroscopy (EDX). Cathodoluminescence yields information about the electronic band structure of the target material.

A different, but related apparatus can be used for transmission electron microscopy (TEM) which detects electrons that are transmitted through the sample and are captured on the back side. Only very thin samples can be measured this way since thick samples do not allow the transmission of electrons. The spatial resolution of TEM microscopes (~ 0.1 nm) is about an order of magnitude better than SEM microscopes (~ 1 nm).

SEM microscopes are also used in electron beam lithography. E-beam lithography is a method whereby an electron beam is used to write patterns in an electron sensitive resist. By developing the exposed sample, written areas are selectively removed or preserved, depending on the type of resist and developer. This way, people were able to make patterns with a line width of only ~ 10 nm.

SEM was used to generally visualize and investigate samples. Although SEM images show no difference between single layer graphene and few-layer graphene, they are very useful to investigate overall morphology and lateral aspects. The e-beam lithography module was used to write electrical contact lines onto ultrathin graphite flakes.

The SEM microscope, a Quanta 200F (FEI Europe, Eindhoven, The Netherlands), with field emission source, was operated by Dr. Jan D'Haen and Bart Ruttens. It is equipped with an ETD, SSD, EDX module and an electrostatic beam blanker to perform e-beam lithography. The e-beam lithography module is a Nanometer

Pattern Generation System (NPGS) from JC Nabity Lithography systems (Bozeman, MT, USA).

2.5 Contact angle measurements

Because SEM is not suited for investigation of material surface terminations like oxidation and hydrogenation, which are important parameters for chemical functionalization routes, other methods are required for these purposes.

The hydrophilic or hydrophobic properties of sample surfaces can be probed with contact angle measurements. A small droplet of test fluid, like water, is deposited on the sample surface and the angle between the tangent, at the bottom of the droplet, and the sample surface is measured. Small water contact angles (0° - 90°) correspond to hydrophilic surfaces and large contact angles (90° - 180°) correspond to hydrophobic surfaces. The method is illustrated in Figure 2-7. In practice, a small droplet (e.g. 1 µl) is placed on the sample with a needle attached to a movable arm. The droplet is filmed by a camera while lit from behind to maximize optical contrast. Dedicated software models the shape of the droplet and determines the contact angle.

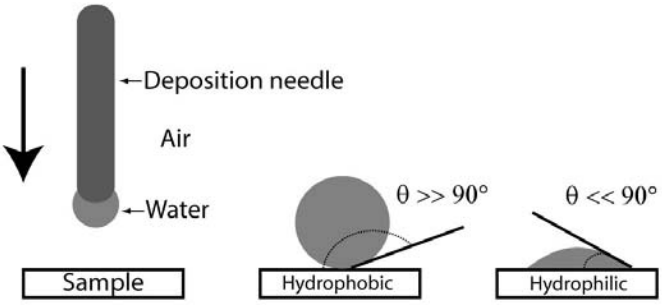

Figure 2-7. Contact angle principle.

The contact angle, and related hydrophilicity, are determined by the polarity of the surface material and the roughness of the surface. Although it is possible to calculate also interfacial energies, the contact angles as such are used in this work as they already give interesting information about surface properties.

This method was used to investigate substrate surfaces before and after functionalization with fatty acid molecules. Measurements were performed on an OCA 15 plus Contact angle system from Dataphysics (Filderstadt, Germany) combined with SCA20 software.

2.6 X-ray photoelectron spectroscopy

X-ray photoelectron spectroscopy (XPS) is a (semi)quantitative, surface sensitive, technique that provides information about elemental composition, chemical state and electronic state. XPS is based on the photoelectric effect; meaning that electrons are emitted from the surface by incident X-ray photons. The photoelectrons that are able to escape from the surface pass through a collector lens into the electron energy analyzer and eventually reach an electron detector. This way, the kinetic energy of the escaped electrons is measured. Since the energy of the incoming X-rays is known, it is possible to determine the binding energy of the detected photoelectrons via the following formula:

$$E_B = E_{X-ray} - (E_K + \phi) \tag{2.2}$$

with E_B the binding energy, $E_{X\text{-ray}}$ the energy of the incoming X-rays, E_K the measured kinetic energy of the photoelectrons and Φ the work function of the spectrometer. The latter is determined by calibration of the spectrometer. A schematic representation of the XPS principle is given in Figure 2-8, where a core 1s electron is ejected by an X-ray photon. XPS measurements require ultra-high vacuum conditions as the detector is usually placed at a rather large distance from the sample (~ 1 m). Although X-rays have a large penetration dept, the photoelectrons can only escape into the vacuum from the top 1 – 10 atomic layers.

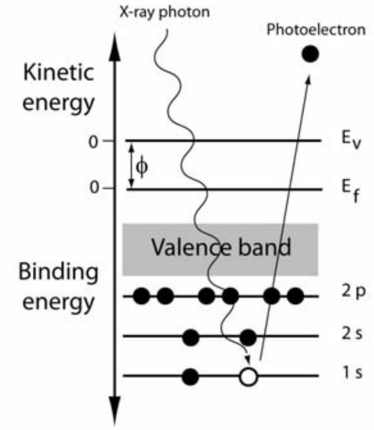

Figure 2-8. Schematic representation of the XPS principle.

The high energy X-rays eject core level electrons which have specific binding energies depending on the type of chemical element and chemical state of the atom. The amount of detected electrons is counted for each specific energy value of the measured spectrum. This number is plotted against the binding energy in a typical XPS spectrum.

In addition to core level electrons, there is also emission of Auger electrons (1000 – 1200 eV) and low energy valence level electrons (0 – 20 eV). Auger electrons are emitted as a relaxation mechanism. After emission of the core electron, the core level vacancy is filled with an electron from higher energy levels, accompanied by the formation of excess energy. This excess energy is emitted as X-ray fluorescence or is transferred to another electron that subsequently escapes from the surface, known as an Auger electron. These Auger electrons are specifically analyzed in a technique called Auger electron spectroscopy (AES). Furthermore, a related technique exists that is dedicated to the study of valence level electrons. This technique is called ultra-violet photoelectron spectroscopy (UPS), as it uses UV photons with lower energy as compared to X-ray photons.

XPS contributed to this work by the characterization of samples after the functionalization procedures were performed. XPS was used to search for the presence of molecules linked to HOPG and flakes deposited on Si. XPS was also applied in the general sample characterization with respect to impurities.

XPS measurements were performed by Prof. Dr. Hans-Gerd Boyen. The measuring device was a 5600 LS electron spectrometer from Physical Electronics (Chanhassen, MN, USA). X-rays were monochromatic (1486.6 eV), and produced by an AlK_{α} source.

2.7 Fluorescence-based techniques

2.7.1 Fluorescence theory

Fluorescence is a process of relaxation of an excited molecular state through the emission of a photon. The absorption and relaxation processes taking place between molecular energy levels are given in a so called Jablonski diagram, see Figure 2-9. If a fluorescently active molecule absorbs a photon with a specific energy, it is excited from the singlet electronic ground state (S_0) to an excited electronic state, e.g. S_1, and a certain vibrational substate. This excited state is unstable and the molecule relaxes back to the ground state via radiative and nonradiative processes. Fluorescence is the process with the following transitions: first, energy is lowered by the nonradiative vibrational relaxation within the same electronic level, accompanied by heat dissipation. This is followed by the transition from the excited electronic state to a certain vibrational level of the electronic ground state, accompanied by photon emission. This photon emission is the actual fluorescence. The emitted photon has a longer wavelength (smaller energy) than the absorbed photon, due to the previous vibrational relaxation. The red shift between absorbed light and emitted light frequency is called the Stokes shift. Another possible way of relaxation is intersystem crossing where the electron undergoes a spin conversion into the forbidden excited triplet state (T_1), followed by the delayed emission of a photon. This photon emission process is called phosphorescence. Phosphorescence and fluorescence take place in different time scales, namely 10^{-3} – 10^{2} s for phosphorescence and 10^{-9} – 10^{-7} s for fluorescence.

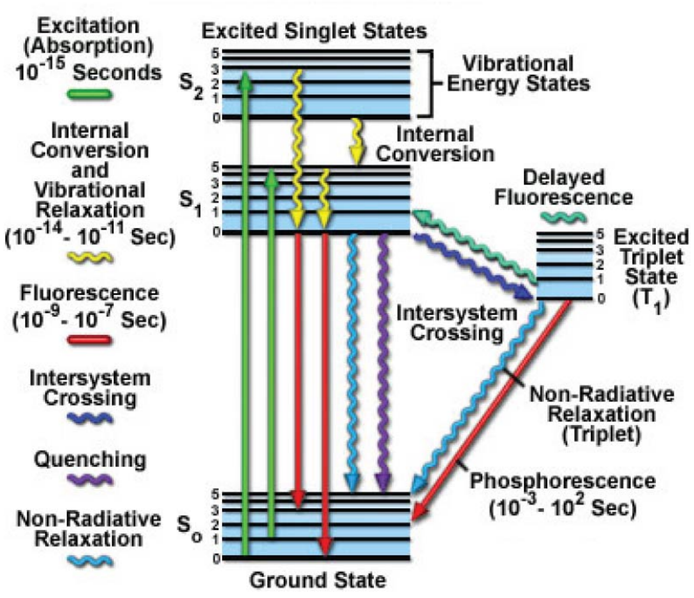

Figure 2-9. Jablonski energy diagram [190]

The transition to the electronic ground state is also possible through non-radiative relaxation, like heat loss. Fluorescence quenching is another way of relaxation, where excess energy is absorbed by another molecule. The latter is also called Förster resonance energy transfer.

Fluorescing molecules contain delocalized electrons that readily switch between the molecular energy states. Therefore, they are most often aromatic or conjugated molecules. Some molecules are autofluorescent and can be used as such in fluorescence-based techniques while others are labeled with a fluorescent dye in order to be able to detect them. The Stokes shift is a very convenient property of fluorescence because it allows fluorescence-based techniques to differentiate between excitation light and emission light. Fluorescent dyes preferably contain a large Stokes shift. Other important characteristics of fluorophores, fluorescing groups, are the fluorescence quantum yield, Φ_f, and molar extinction coefficient, ε_{max}. Fluorescence quantum yield gives the efficiency of the fluorescence process and can be defined by the following equations:

$$\phi_f = \frac{N_{em}}{N_{abs}} \tag{2.3}$$

$$\phi_f = \frac{k_f}{\sum k_i} \tag{2.4}$$

N_{em} and N_{abs} in equation (2.3) correspond to the number of emitted fluorescence photons and the number of absorbed photons, respectively. The symbols k_f and k_i in equation (2.4) denote the rate constant of fluorescence emission and the rate constants of all other relaxation mechanisms, respectively. The molar extinction coefficient is a measure of the ability of fluorophores to absorb photons with a wavelength equal to the absorption maximum.

Fluorescence-based techniques were used within this thesis to detect the presence of functionalizing molecules and to visualize their spatial distribution on sample surfaces. The different employed fluorescence-based techniques are conventional fluorescence microscopy, confocal laser-scanning fluorescence microscopy and fluorescence spectroscopy.

2.7.2 Fluorescence microscopy

Fluorescence microscopy is an imaging technique much like conventional light microscopy. Instead of absorption and reflection of light by the sample, it utilizes fluorescence light coming from the sample. Usually, a narrow spectrum lamp, like a xenon arc lamp or a mercury-vapor lamp, is used as illumination source. Excitation light passes through a filter to obtain monochromatic light, followed by the focusing on the sample. Emitted photons pass through an objective and an emission filter that only allows wavelengths coming from the desired fluorescence signal.

Fluorescence microscopy was used to investigate the hybridization and denaturation of fluorescently labeled DNA strands on carbon nanowall samples as discussed within chapter 3. DNA strands were labeled with the Alexa Fluor 488 fluorophore. The chemical structure and absorption/emission spectra of Alexa Fluor 488 are presented in Figure 2-10.

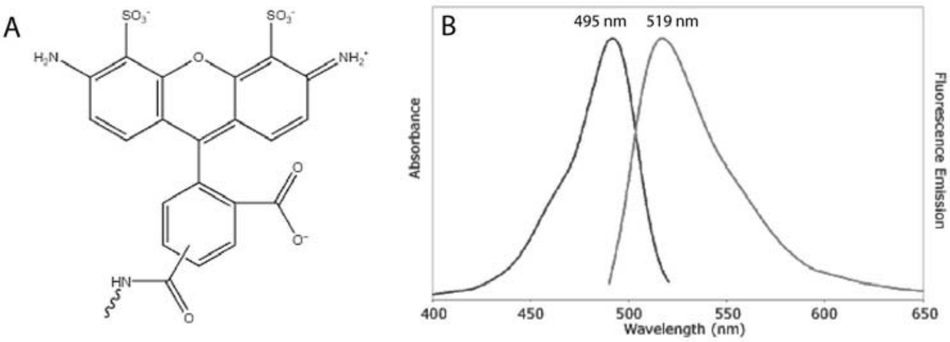

Figure 2-10. Chemical structure (A) and absorbance- and emission spectrum (B) of Alexa Fluor 488 label. The maximum absorption and emission are located at a wavelength of 495 nm and 519 nm, respectively. This means that there is a Stokes shift of 24 nm.

A Nikon eclipse 80i, equipped with a mercury lamp, was used. The microscope belongs to the group of Prof. dr. Luc Michiels. An appropriate filter set was used consisting of the following components: Excitation bandpass filter (482/35 nm), a dichroic mirror (506 nm) and an emission bandpass filter (536/40 nm). A 20x objective was used with 400 ms exposure time to excite the fluorescence labels. The gain was set to 4x to enhance the signal. Measurements were performed in phosphate buffered saline (PBS) at room temperature. PBS is an important buffer solution with isotonic salt concentrations that is used to preserve the natural conformation of biomolecules. If biomolecules, like DNA, are not in their natural conformation, they lose their biological activity and DNA strands would not be able to hybridize for example.

2.7.3 Confocal laser-scanning fluorescence microscopy

Instead of using a lamp to illuminate the sample as a whole, a focused laser beam is used in confocal laser-scanning fluorescence microscopy to scan the sample surface line by line. This method will further be referred to as confocal fluorescence microscopy. A detector measures the emitted fluorescence photons at each point of each line and builds up a fluorescence image of the investigated sample. Furthermore, this technique can selectively detect photons coming from a specific narrow depth. This process, also called optical sectioning, is possible through the use of two pinholes or small apertures, one before the laser hits the sample and one before emission light falls on the detector. The smaller the pinhole, the smaller the depth of focus or optical coupe. This implies that confocal fluorescence microscopy can achieve higher resolutions than conventional fluorescence microscopy as background light coming from out-of-focus planes is eliminated.

This method was used in all chapters of this thesis dealing with the functionalization of carbon structures. In addition to the previously described Alexa Fluor 488 label, another fluorescent label, attached to DNA strands, was used. This was a 6-FAM (6-carboxyfluorescein) label with similar absorption and emission spectra to the Alexa Fluor 488 label. The 6-FAM chemical structure is given in Figure 2-11.

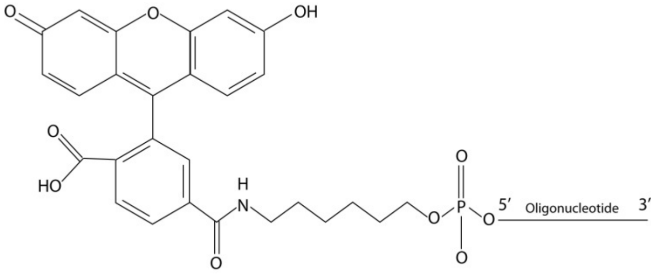

Figure 2-11. Chemical structure of the 6-FAM label.

The characterization was performed with an inverted microscope, type LSM 510 META from ZEISS in combination with the 488 nm line of an Ar-ion laser. The microscope belongs to the group of Prof. dr. Marcel Ameloot. The laser intensity was set to 10 %, corresponding to 33 μW at the sample position. The microscope configuration that was used is shown in Figure 2-12. Excitation light from the laser passes through a pinhole and is reflected by the HFT 488 dichroic mirror and passes through the objective before it excites the sample surface. Emitted light coming from the sample passes through the objective, the HFT 488 dichroic mirror, the NFT 490 dichroic mirror, the LP 505 emission filter, a pinhole and finally reaches the detector. The HFT 488 dichroic mirror reflects all wavelengths under 488 nm and allows higher wavelengths to pass. The NFT 490 beamsplitter reflects all wavelengths under 490 nm and allows higher wavelengths to pass. The light that is reflected by the NFT 490 beamsplitter can be used for detection with a second detector but this option was not utilized in case of this work. The LP 505 emission filter blocks all wavelengths below 505 nm.

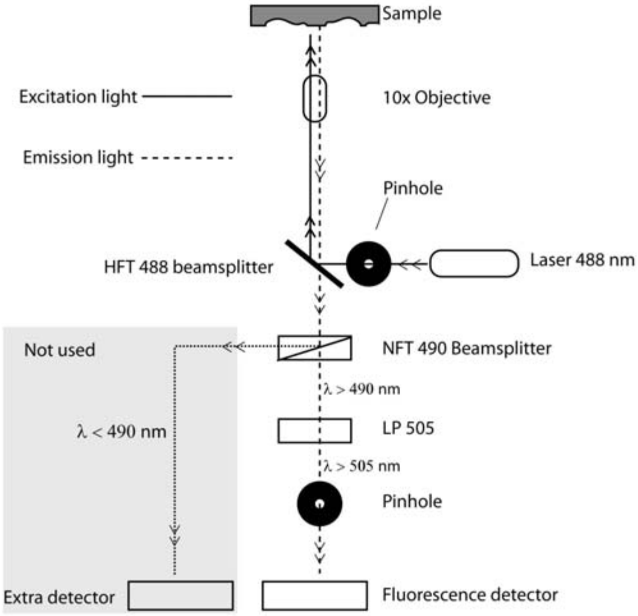

Figure 2-12. Confocal fluorescence microscope configuration.

Unless stated otherwise, the pinhole was set to 150 µm and the gain to 1000. Measurements were performed at room temperature in PBS. The confocal fluorescence microscope allows to bleach the fluorescent labels in a selected region of the sample, meaning that the labels are destroyed by prolonged intense laser light. For bleaching experiments, laser intensity was set to 100 % and selected regions were illuminated for a prolonged time at slow scan rates. Bleaching allows distinguishing actual fluorescence from background signals like reflection. Only actual fluorescence is bleachable whereas reflection is not.

2.7.4 Fluorescence spectroscopy

Fluorescence spectroscopy is used to measure the excitation and emission spectra of fluorescently active molecules. Also, it can be used to confirm the presence of fluorescent molecules and quantify their concentration if a calibration curve has been measured. Diffraction grating monochromators are used to select the desired excitation and emission wavelengths. Emission spectra are taken by illuminating the sample at a fixed wavelength (preferably at an absorption maximum) and measuring the emitted light, wavelength by wavelength, over the range of interest. Excitation spectra are taken the other way around. The spectrofluorometer has a T-shape setup (like the confocal fluorescence microscope) so that the detector is not placed in the line of excitation light.

Fluorescence spectroscopy was used to detect the presence of the fluorescently active linker molecule 1-pyrenedecanoicacid (PDA) in the section concerning the non-covalent functionalization of graphene-like flakes. The emission spectrum of PDA, taken at λ_{EX} = 340 nm, is presented in Figure 2-13. Fluorescently labeled DNA molecules were also detected by fluorescence spectroscopy.

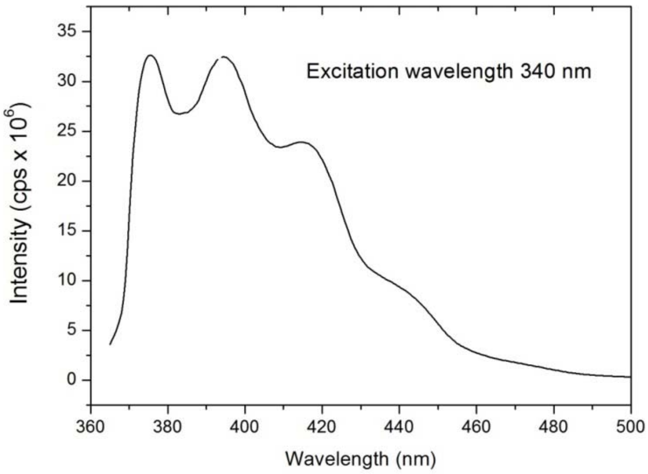

Figure 2-13. Emission spectrum of PDA in methanol, taken at λ_{EX} = 340 nm. Three emission peaks can be seen at 376 nm, 396 nm, 415 nm and a shoulder at 440 nm.

Spectra were taken with a QuantaMaster NIR fluorescence spectrophotometer from Photon Technology International (Seefeld, Germany) combined with a xenon light source. Fluids were measured in quartz cuvettes and solids were measured with a sample holder at an angle of 30° with the incident light. In addition, a FL3-22TAU spectrometer from HoribaJobin-Yvon, equipped with a 450 W Xenon lamp, was used.

Chapter 3

Functionalization of carbon nanowalls

3.1 Introduction

The combination of non-biological carbon and biological molecules is currently being studied intensively. Since the discovery that two-dimensional graphene layers do not only exist in theory but also in nature, special interest went to graphene and graphene-like structures. Their use in sensing devices is growing and some promising results were obtained for graphene-based gas sensors for example. Experimental sensors were able to detect NH_3 [5,168], CO [5], H_2O [5,168], dinitrotoluene (a simulant for the explosive TNT) [166,168] and stimulants for chemical warfare agents like mustard gas and sarin [166]. Regarding their use in biosensing devices only very little work has been done so far. Graphene-based transistor structures were developed to detect bacteria [169], DNA [169], proteins [170] and antigens [4]. Also, DNA sensors were developed that are based on the quenching of fluorescently labeled DNA and the subsequent fluorescence recovery after hybridization [151,171].

This chapter focuses on the functionalization of graphene-like structures with single stranded (ss) DNA fragments. The aim of this functionalization is to investigate the possibilities to use graphene and graphene-like structures as a platform for biosensors. These biosensors should be able to detect single mismatch DNA mutations without the need to amplify the sample DNA by means of a polymerase chain reaction (PCR).

The development of biosensors requires a material with a high surface area that can be functionalized with receptor molecules. Carbon nanowalls (CNWs) are ideally suited for such purposes as they are a graphene-based material that can be readily functionalized at the edges. They are grown by means of microwave plasma-enhanced chemical vapor deposition (MW PECVD), yielding FLG with a morphology that is comparable to lettuce, see Figure 3-1. The upstanding structure of this material results in many exposed edges that are well suited for biological functionalization. The edges contain hydrogen terminated bonds because they were grown in CH_4/H_2 plasma. These hydrogen terminated bonds are much more easy to functionalize than the basal planes of graphene. The latter, which are much more difficult to chemically functionalize, will be addressed in Chapter 4. Furthermore, the growth of CNWs via MW PECVD is highly reproducible and more easy to control as compared to other graphene production methods.

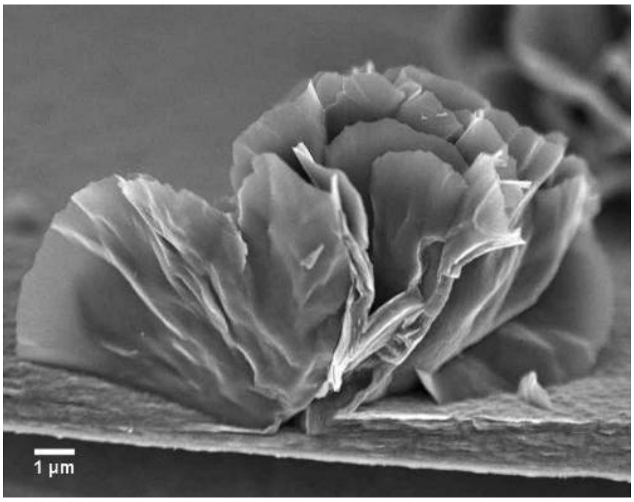

Figure 3-1. Cross-section SEM image of CNW morphology [191]

3.2 CNW structure

CNW are a network of upstanding wall-shaped structures with each wall consisting of a stack of four to six atomic graphene layers, oriented perpendicular to the substrate surface. The nanowalls have micrometer-wide lateral dimensions and a thickness of a few nanometer [191,192]. Their morphology is shown in Figure 3-1 and Figure 3-3. The CNW were grown and qualitatively characterized at the "Vlaamse Instelling voor Technologisch Onderzoek" (VITO) in Mol (Belgium) [191].

Thorough structural analysis by TEM at EMAT (Antwerp University, Belgium) revealed that these structures were highly crystalline few layer graphene stacks.

The morphology and flake thickness are shown in the scanning and transmission electron microscopy (SEM and TEM) images of Figure 3-3. The TEM analysis demonstrates the almost planar shape of the resulting structures with an average flake thickness of 4 to 6 atomic layers and an interlayer distance of 0.32 nm, corresponding to graphene stacks.

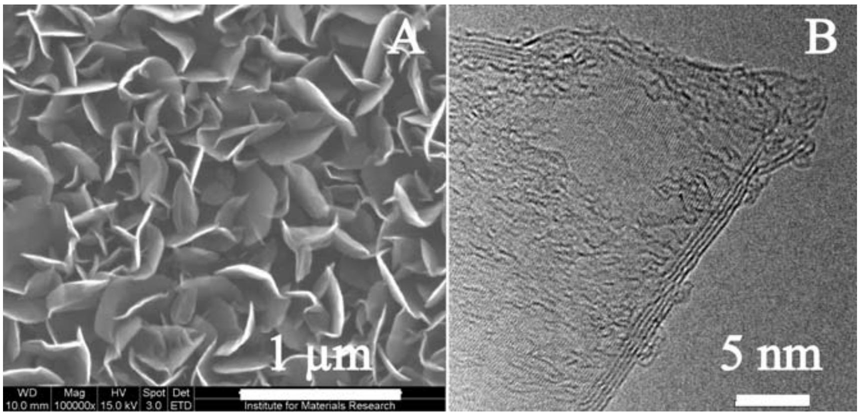

Figure 3-2. (A) Top view SEM image of CNW showing the overall morphology. (B) TEM image [191] revealing the almost planar shape and thickness of the CNW. Flakes consist of 4-6 atomic layers.

Raman spectroscopy confirms the high crystalline order of the flakes. Figure 3-3 shows a weak D-band (1350 cm^{-1}), caused by phonon scattering at defect sites and impurities. There is a strong G-band (1580 cm^{-1}), linked to phonon vibrations in sp^2 carbon. The intensity ratio of these two bands gives the R-value, which is an indicator for the crystal quality. The lower this number, the higher the quality. An R-value of zero indicates perfect quality of HOPG or graphene. The CNW have an R-value between 0.2 and 0.3 and therefore show good crystallinity. The absence of a typical graphite shoulder at 2680 cm^{-1} in the 2D-band (2700 cm^{-1}) is proof that the structures are few layer graphene rather than graphite. The 2D-band is the second order of zone-boundary phonons [184,191].

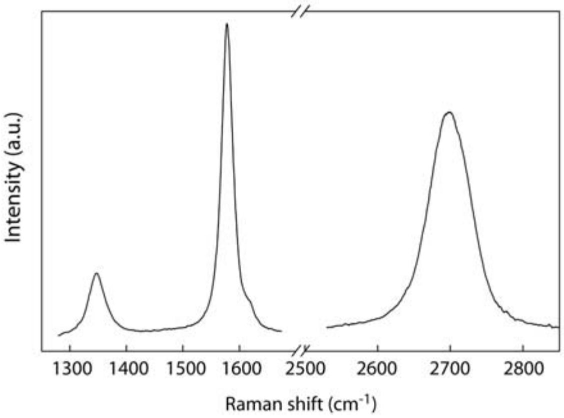

Figure 3-3. Raman spectrum [191] *of CNW with D-band (1350 cm^{-1}), G-band (1580 cm^{-1}) and 2D-band (2700 cm^{-1}). Here, the R-ratio lies between 0.2 and 0.3.*

It is interesting to note that boron nitride (BN) structures with similar morphology can also be grown [193,194]. BN can exist in sp^2 and sp^3 hybridized forms like carbon. The sp^2 hexagonal BN (hBN) has exactly the same structure as graphene and graphite. It is also a layered material with a comparable interlayer spacing. In contrast to the semimetallic behavior of graphite, it is a semiconductor with a wide band gap of around 6 eV. Just like CNW, they can be grown by MW PECVD, but with a gas mixture of BF_3, N_2 and H_2.

3.3 Synthesis by MW PECVD

The CNW were grown on supporting substrate surfaces by microwave plasma enhanced chemical vapor deposition (MW PECVD), without the need for a metal catalyst. All substrates that can withstand temperatures up to 700 °C can be used and in this study silicon substrates were employed. These form a thin SiC layer, which provides a good attachment between the CNW and the Si substrate. First, a heating step was applied to the substrates, in which they were heated to 700 °C in a H_2 plasma. Immediately after the heating step, a gas mixture of CH_4 and H_2, with a ratio of 1/8, was injected into the growth chamber. The gas mixture had a total flow rate of 200 sccm and growth times varied from 5 min to

40 min. Plasma power and pressure are kept at 2 kW and 53.33 hPa, respectively. [191]

3.4 Functionalization with DNA strands

Materials

The probe ssDNA oligonucleotides had the sequence: 5′- NH_2 – C_6H_{12} – AAA-AAA-ACC-CCT-GCA-GCC-CAT-GTA-TAC-CCC-CGA-ACC – 3′ (36 bases) and were modified at the 5′ end with an amino (NH_2) group. Hybridization and denaturation experiments were performed with complementary and single base mismatch target ssDNA oligonucleotides, both labeled with a fluorescent Alexa 488 label at the 5′ end. The nucleotide sequence of the complementary strands was 5′- Alexa 488 – GGT-TCG-GGG-GTA-TAC-ATG-GGC-T**G**C-AGG-GG - 3′ (29 bases) in comparison with the single mismatch sequence 5′ – Alexa 488 – GGT-TCG-GGG-GTA-TAC-ATG-GGC-T**C**C-AGG-GG - 3′ (29 bases). All these were purchased from Invitrogen (Merelbeke, Belgium). We also used probe ssDNA oligonucleotides with the amino group and the Alexa 488 label on the same strand allowing to directly investigate the probe DNA attachment to the CNW. These were purchased from Eurogentec (Seraing, Belgium) and had the following sequence: 5′ – NH_2 – C_6H_{12} – CCC-CTG-CA – Alexa 488 – 3′.

MicroHyb hybridization buffer was purchased from Invitrogen (Merelbeke, Belgium). Sodium dodecyl sulfate (SDS), saline sodium citrate (SSC) buffer dry blend and acetic acid (CH3COOH) were obtained from Sigma-Aldrich (Bornem, Belgium). 10-Undecenoic acid was purchased from Acros Organics (Geel, Belgium). 2-[N-morpholino]-ethanesulphonic acid (MES) buffer and 1-ethyl-3-(3-dimethylaminopropyl)-carbodiimide (EDC) were acquired from Pierce (Rockford, USA). Sodium hydroxide was bought from UCB (Brussels, Belgium). Phosphate buffered saline (PBS) was homemade (1.29 M NaCl, 0.05 M $Na_2HPO_4 \cdot 2H_2O$, 0.015 M KH_2PO_4, pH 7.4).

3.4.1 Attachment of probe DNA

Since the CNWs are grown under methane and hydrogen atmosphere, we can assume that the edges of the flakes are hydrogen-terminated. Owing to this, the CNWs can be functionalized without breaking up the graphene-like structures. Graphene in itself is highly inert to chemical reactions and thus impossible to functionalize covalently without destroying its structure. Only the edges of graphene flakes are chemically active, because these can be seen as crystal defects. Defects in the basal planes of the structures are also potential sites for chemical reactions. The contribution of these defects will probably be small since Raman spectroscopy demonstrates good crystallinity with an R-value of 0.2 - 0.3, as stated above. Given the hydrogen-terminated edges of the CNWs, our functionalization method was based on a scheme for the attachment of biomolecules to hydrogen-terminated diamond. Different methods exist to functionalize diamond, see the review articles [195,196]. One attachment scheme is based on photochemical attachment of a linker molecule [197]. This route was simplified by the UHasselt group [198,199] and optimized for the binding of DNA molecules to nanocrystalline diamond [200].

Method

In order to attach DNA molecules to the CNW, an unsaturated fatty acid linker molecule, 10-undecenoic acid, is covalently bound to the CNW edges. This is achieved by UV illumination of a liquid 10-undecenoic acid film, on top of the CNW substrate, at 254 nm under protective N_2 atmosphere, for 20 h by a TUV G4T4 4W lamp (Philips) at 1 cm from samples, as depicted in Figure 3-4 (A).

The carboxyl group from the fatty acid was used in an EDC-mediated reaction to bind amino (NH2)-modified DNA strands to this carboxyl group through a peptide bond. This is shown in Figure 3-4 (B).

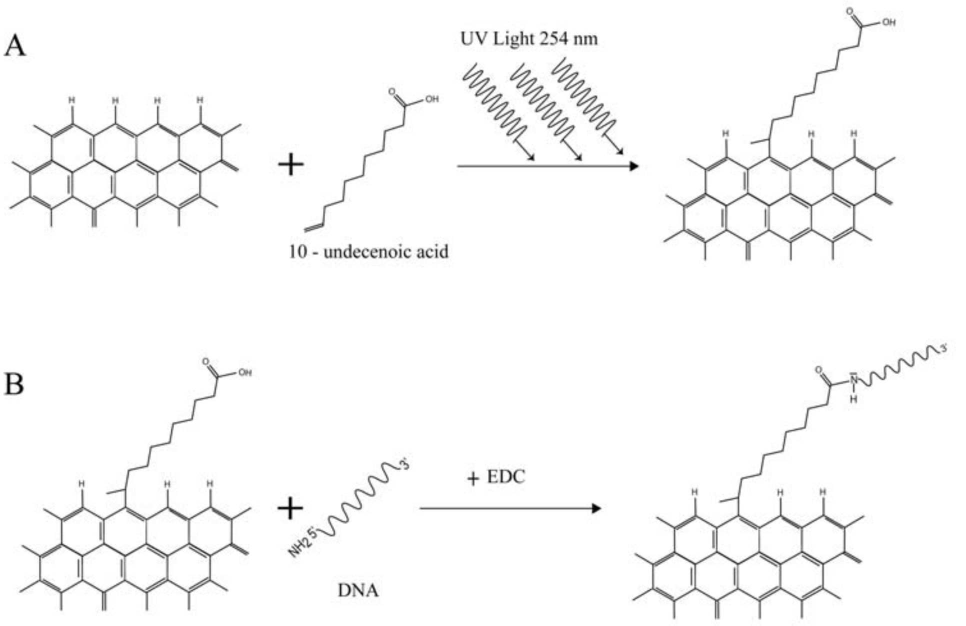

Figure 3-4. (A) Photochemical reaction to bind an unsaturated fatty acid (10-undecenoic acid) to the CNW edges. (B) EDC-mediated reaction to bind amino-modified probe DNA to the fatty acid carboxyl group.

A washing step with acetic acid was carried out before DNA molecules were added and thus after the UV attachment of the linker molecule. This was done to remove all excess fatty acid molecules.

Next, 20 µl solution of NH_2-modified DNA (15 pmol/µl, = 300 pmol per sample) and MES buffer was added. This was incubated at room temperature for 30 min. EDC powder was dissolved in cold MES buffer to a concentration of 50 mg/ml, immediately followed by the addition of 15 µl of this solution to each sample. The samples with a mixture of DNA, MES and EDC were then incubated for 4 hours at 4 °C.

The added DNA was either 8 bases long with fluorescent Alexa 488 label or 29 bases long without fluorescent label. The latter was used to perform hybridization and denaturation experiments. In this case, the target DNA strands, that are hybridized to the bound probe DNA, possess the fluorescent Alexa 488 label.

Reference samples were made by not adding EDC to these samples; MES buffer was added to these EDC-negative samples instead of EDC. Except for this, the EDC-negative samples underwent the same protocol as the EDC-positive samples including the exposure to DNA. A second type of reference samples was made by omitting the fatty acid molecules. Except for this, these samples also underwent the normal protocol including UV illumination.

The excess of DNA was removed after the 4 h incubation step. The removal was done by means of several rinsing steps with 2× SSC buffer + 0.5 % SDS, 2× SSC buffer + 1% SDS, 0.2× SSC, PBS and samples were finally stored in PBS.

Results on DNA binding

DNA binding was investigated by means of conventional and confocal fluorescence microscopy, both under wet conditions to avoid fluorescence quenching by the CNW. The wet conditions prevent the DNA from sticking to the CNW surface. The probe DNA strands that are covalently linked to the CNW surface were fluorescently labeled to examine the covalent binding directly or, alternatively, the target DNA, used to hybridize to the bound probe DNA, was fluorescently labeled to check hybridization. Figure 3-5 shows confocal fluorescence images of CNW samples with single stranded probe DNA of 8 bases.

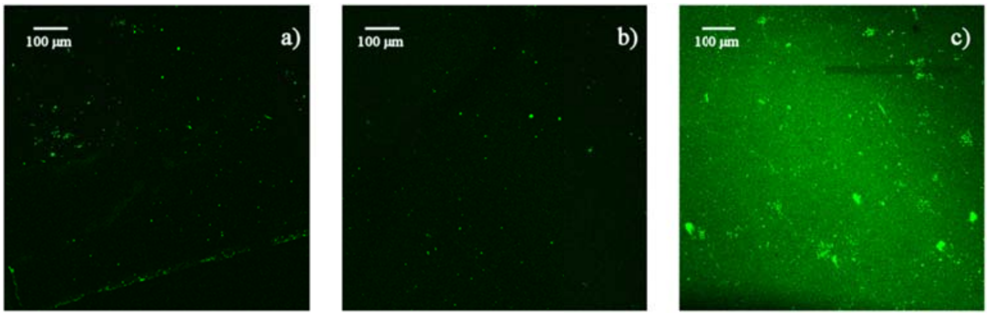

Figure 3-5. Confocal fluorescence images of CNW samples. (a) Reference sample where no fatty acid was added. (b) EDC-negative reference sample. (c) Sample where the normal binding protocol was carried out. The bar in the upper right corner was induced by photobleaching of the Alexa dye. The same intensity scale was used for all images.

The left and middle image show reference samples, where the binding protocol was performed without the fatty acid or EDC molecules, respectively. The image on the right was taken from a CNW sample with bound DNA. The normal binding protocol was carried out on this sample. It is clear that the reference samples show almost no fluorescence, indicating the importance of the fatty acid linker and the EDC mediator in the reaction scheme. The absence of fluorescent DNA on these reference samples excludes adsorption as immobilization method on the positive sample. The right image contains a darker bar in the upper right region. In this bar, fluorescent labels were bleached by prolonged exposure to intense laser light. This was done to eliminate reflection and autofluorescence of CNWs as a possible source of the signal. The fluorescence intensity on these CNWs is comparable to the fluorescence intensity measured on functionalized diamond samples, which contained about 10^{12} DNA molecules per cm^2 of substrate surface [200]. This corresponds roughly to a covering percentage of 3%.

3.4.2 Hybridization of target DNA

Method

Samples were hybridized, denatured and rehybridized 10 times to investigate the reusability of the system. The principle of hybridization is shown in Figure

3-6. Hybridization was done by adding 30 µl solution of target DNA in MicroHyb hybridization buffer so that a total quantity of 900 pmol per sample was added, which is three times the quantity of added probe DNA. Samples were incubated for 2 h in the oven. The hybridization temperatures varied between 30 °C and 70 °C. Two kinds of target DNA were compared: fully complementary strands to the probe DNA and strands with a single base mismatch from a total of 29 bases. The samples were rinsed again after DNA hybridization. This was done by immersing them in PBS, 0.2× SSC (at 5 °C below the hybridization temperature) and 2× SSC with 1% SDS (room temp). Finally, they were stored in PBS. Denaturation was executed in NaOH (0.1 M) in the oven at 50 °C for 0.5 h. Afterwards, the samples were rinsed with PBS.

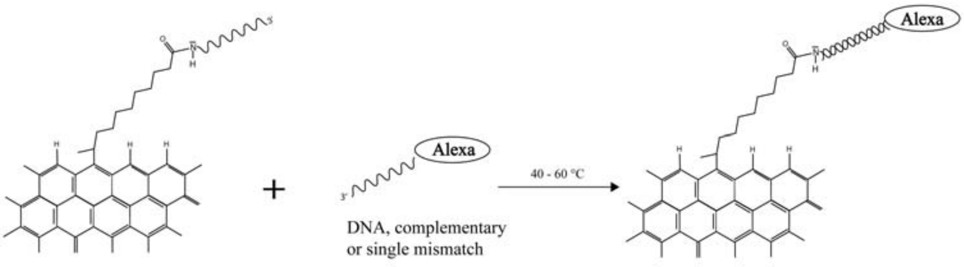

Figure 3-6. Hybridization of fluorescently labeled target DNA to bound probe DNA. DNA molecules are not drawn to scale.

Results on hybridization

The next step consisted of hybridization of the complementary DNA strands to the covalently bound probe DNA, see Figure 3-7. The left image shows a hybridized sample, the middle image is the same sample after denaturation of the double stranded DNA with NaOH. The right image is again an EDC-negative reference sample, so there was no covalently attached DNA present on the surface to hybridize with. Nevertheless, the right image has a very weak green shine due to a small quantity of adsorbed target DNA.

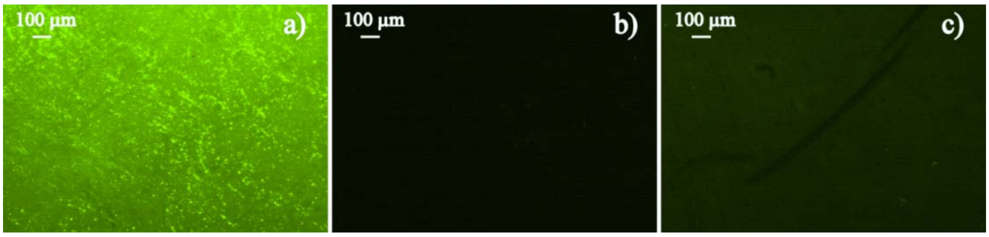

Figure 3-7. Conventional fluorescence microscopy images of hybridized CNW samples. (a) Fluorescently labeled target DNA hybridized to covalently bound probe DNA. (b) Same sample after denaturation. (c) EDC-negative reference sample with minimal amount of adsorbed target DNA. The same intensity scale was used for all images.

After denaturation of the double stranded DNA, target DNA strands can be rehybridized to the fully complementary probe DNA and this cycle could be successfully repeated at least 10 times, as illustrated in Figure 3-8. Fluorescence intensity was quantified by Image J software, which calculates the mean fluorescence intensity for a specified region in the fluorescence image. Per image, two regions of each 245 µm x 245 µm were analyzed and their average is given.

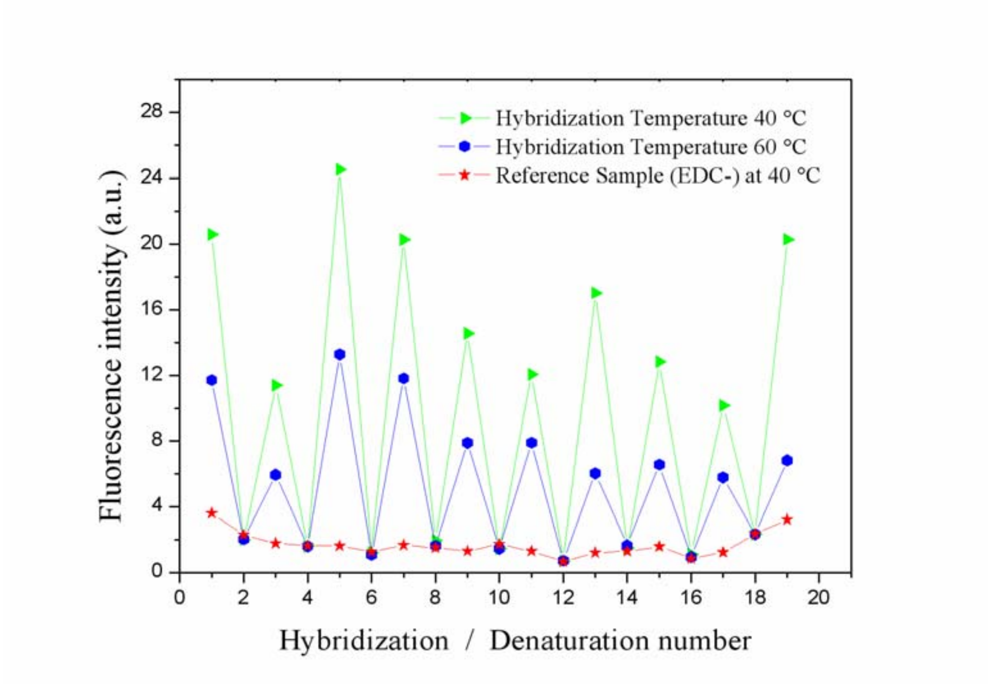

Figure 3-8. Graph showing fluorescence intensity after successive hybridization and denaturation steps for two different hybridization temperatures (green triangles: 40°C, blue circles: 60°C). The graph also displays an EDC-negative reference sample (red stars). Odd and even numbers on the x-axis represent hybridization and denaturation runs, respectively.

The graph starts with the first hybridization and the minima correspond to denaturation steps. The successive hybridization peaks are not always equally high, but there is an obvious difference between EDC-positive and EDC-negative samples and between hybridization and denaturation intensities. The curve belonging to the EDC-negative sample remains flat, meaning that there is no difference between the hybridized and denatured state in this case.

Also, different hybridization temperatures were investigated to seek for the optimal temperature where there is a high fluorescence signal and a clear distinction between fully complementary DNA (COM) and DNA with a single mismatch (MM).

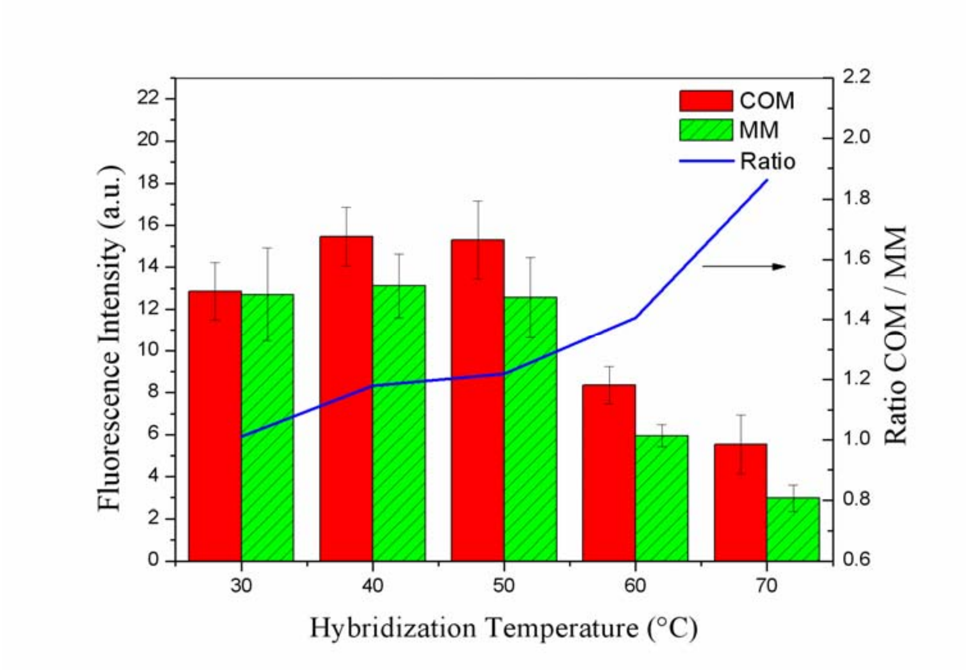

Figure 3-9. Influence of the temperature on hybridization with complementary (COM) and single mismatch (MM) DNA strands. 40 °C and 50 °C give the highest intensities. The relative difference between complementary and single mismatch DNA increases with temperature, see ratio COM/MM. Error bars show standard errors averaged over n=7 independent measurements.

As can be seen in Figure 3-9, the hybridization temperatures around 40 °C - 50 °C give the highest fluorescence signals. Figure 3-9 also nicely demonstrates the high selectivity of the system. The relative difference in fluorescence intensity between complementary and mismatched DNA increases with rising hybridization temperature. This is shown by the ratio curve. (At higher temperatures the ratio could be expected to decrease again, as the melting temperature of the dsDNA is approached, but we have not tested temperatures higher than 70 °C.) Above a hybridization temperature of 30 °C there is a substantial difference in fluorescence signal, and consequently DNA hybridization. This difference becomes marked from a hybridization temperature of 60 °C onwards, as standard error bars no more overlap. Therefore, one can conclude that for the considered mismatch, the optimal hybridization temperature is 60 °C since this temperature yields a significant difference between COM and MM DNA and in addition gives a fluorescence intensity that is still sufficiently high.

3.4.3 Substrate investigation

The Si substrates that were used in the previous experiments are not homogeneously covered with CNW. The area in the centre of the sample has no CNW. The centre zone is girded by a transition zone with significantly lower density of CNW than the outer regions of the substrate with high density coverage. Furthermore, the CNW in the transition zone are much smaller as compared to outer regions of the substrate. This is shown in Figure 3-10. This difference results from the fact that the plasma is more concentrated at the corners and edges of the sample during the growth of the CNW. Therefore, there is a higher concentration of carbon radicals at these areas, resulting in faster growth. The centre area is possibly covered with a thin layer of amorphous carbon and graphitic carbon, oriented parallel to the substrate.

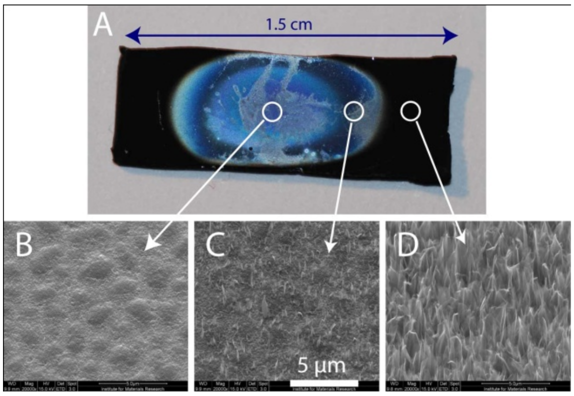

Figure 3-10. (A) Si substrate with CNW and SEM images of the regions indicated in (A). These regions are (B) Uncovered centre zone, (C) Low density transition zone and (D) Outer area with high density CNW. The scale is the same for all SEM images.

Contact angle measurements were performed on the uncovered centre zone and the high coverage zone and this before and after fatty acid attachment. The contact angle was measured using water droplets. A droplet was deposited on the right spot and measurements were started after 10 seconds. One measurement per second was taken for 20s.

Figure 3-11. Contact angle measurements of sample area with high coverage (outer zone) and area with no coverage of CNW (centre zone). Measurements were taken before and after fatty acid attachment.

Figure 3-11 shows that the contact angle is lower for the uncovered area. The CNW are highly hydrophobic as demonstrated by the high contact angle of the densely covered outer zone. The centre area without CNW also has a relatively high contact angle, probably due to some amorphous and graphitic carbon covering the surface. Attachment of fatty acids lowers the contact angle significantly. Although the alkyl chain has a high hydrophobicity, the carboxyl group is hydrophilic. The upward orientation of the carboxyl group seems to dominate the contact angle. The contact angle is lowered for both the covered and uncovered area after fatty acid attachment, meaning that the fatty acid does not bind specifically to the CNW but also to the amorphous carbon in the centre. It should be noted that the hybridization/denaturation experiments, described in the previous section, were performed on the high coverage outer zone of the samples.

Other substrate materials, like quartz and platinum were also tested in addition to Si. These substrates had a weaker attachment of the CNW. As a consequence the CNW film forms bubbles and easily detach from the substrate in liquid environments. For these reasons, these substrates were found to be less useful for functionalization purposes. CNW grown on Si substrates have a stronger attachment to the substrate, due to an intermediate layer of SiC that improves the adhesion. The growth process of the CNW on Si consists of different steps. First a SiC layer is formed, followed by a layer of amorphous carbon. On quartz and platinum there is no carbide layer, providing strong adhesion [191]. Shows confocal microscopy images of CNW grown on quartz and platinum, functionalized with fluorescently labeled DNA.

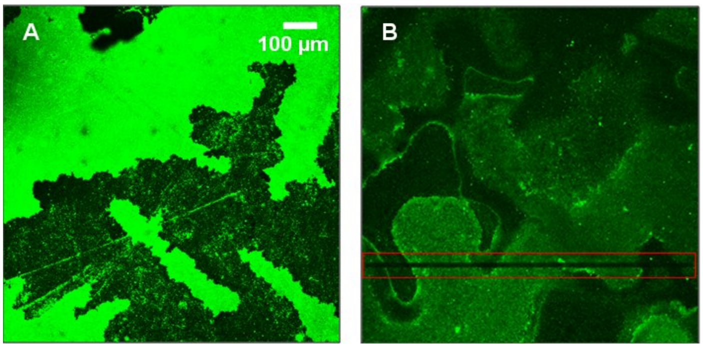

Figure 3-12. Confocal fluorescence images of functionalized CNW grown on quartz (A) and platinum (B). The dark areas are spots where the CNW came off from the substrate. (B) contains a bleached bar, marked by the red rectangle, to confirm that the signal is coming from fluorescent labels.

3.5 Conclusion

MW PECVD grown CNWs were successfully functionalized with DNA strands. Single stranded DNA molecules were covalently bound to the CNW edges. First, a fatty acid linker molecule was attached to the surface through a photochemical reaction and second, an EDC-mediated reaction coupled the DNA molecule to this linker. Conventional and confocal fluorescence microscopy proved that DNA was covalently bound to the CNWs since fatty acid- and EDC-negative reference samples showed almost no fluorescence. The bound DNA maintained its biological activity as it was possible to hybridize the bound DNA with complementary DNA strands. At least 10 denaturation-rehybridization cycles were feasible. The optimal hybridization temperature was found to be around 60 °C. The functionalized CNWs exhibit a high selectivity which is essential in the development of biosensors. The selectivity was proven by a clear difference in hybridization between fully complementary DNA strands and DNA strands with only one base pair mismatch. Although the DNA covering percentage is below maximum density, it proved to be plentiful for fluorescence detection and presumably also for impedimetric detection, as demonstrated by related work on diamond-based electrodes [201]. Finally, CNW are relatively large and robust structures that allow thorough rinsing steps, which are essential in differentiating single mismatch sequences from complementary ones. This ability to properly rinse is an advantage over functionalization of individual graphene flakes where this is not so obvious, as discussed in Chapter 4.

Chapter 4

Functionalization of ultrathin graphite flakes and graphene

4.1 Introduction

The previous chapter dealt with the functionalization of CNW. In the case of these CNW, functionalization takes place on the edges of the nanosheets. Furthermore, they exist in the form of an inhomogeneous film of interconnected nanowalls. This hampers the use and characterization of individual nanosheets. For these reasons this chapter will deal with the functionalization of loose flakes of ultrathin graphite and graphene. The aim is to functionalize the basal plane of the flakes instead of the edges. This is done as a first step in the development of biosensors based on individual graphene flakes. The functionalization of the basal plane of the flake should increase the detection response of the envisioned biosensor.

Two possible functionalization methods were tested: a covalent one and a non-covalent one. The goal was to compare the effect of covalent and non-covalent functionalization on the electronic properties and the sensing capabilities of the flakes. It can be expected that the effect on the electronic properties of both functionalization methods will be different since the covalent method breaks up the sp^2 hybridized structure whereas the non-covalent method should leave the sp^2 structure unaffected. Unfortunately, investigating the effect of functionalization on electronic properties could not be realized within the time frame of this work.

This chapter deals with graphene, FLG and ultrathin graphite flakes. Some characterization methods, like fluorescence microscopy and XPS, were applied on surfaces covered with a bunch of individual flakes, meaning that the flakes do not form a closed film on the substrate. Characterization by Raman spectroscopy enabled to focus on individual flakes. Flakes were deposited on substrates, oriented parallel to the substrate surface, or they were manipulated as fluid suspensions. Flakes possessed a wide variety of lateral dimensions as well as thicknesses, as the methods used to produce them did not allow for dimension control. However, single layer graphene sheets could be selected for Raman spectroscopy measurements.

4.2 Production of flakes

4.2.1 The Geim method

Flakes were produced via the Geim method. Thin layers of graphite were peeled off from graphite crystals with tape. The top layers were removed in order to clean the material. The tape was folded and unfolded about 5 to 15 times, more folding produces more and smaller flakes whereas less folding produces less but bigger flakes. Subsequently, the tape with thin flakes was gently pressed on a Si substrate. Contact was improved by softly rubbing over the tape. The tape was slowly pulled away leaving ultrathin graphene-like flakes on the substrate. Most samples were annealed in the vacuum oven before further processing. Annealing was performed at pressures of ≈ 10^{-8} hPa for 2 hours. Samples for covalent functionalization were annealed at 150 °C and samples intended for non-covalent functionalization were annealed at 250 – 300 °C.

Samples for Raman measurements were made from graphite ore and taped on lightly n-doped Si with 300 nm of SiO_2. The substrates had preformed alignment markers. These markers were either etched 1 μm deep or they were made from tantalum nitride (TaN). The graphite ore, tape and wafers for substrates were all received from the "Nano Applications and Materials Engineering" group of IMEC Leuven (Belgium). Furthermore, our production technique was refined at IMEC.

Other samples were made from HOPG crystals (SPI-2, SPI Supplies, West Chester, USA). The used tape was VD 8 ELEP holder wafer dicing tape (Nitto Denko, Osaka, Japan). Substrates were Si doped with arsenic and covered with 300 nm SiO_2 (WaferNet Inc. San Jose, USA).

4.2.2 Liquid-phase exfoliation

The other method that was used to produce flakes was liquid-phase exfoliation. Small pieces of HOPG (SPI-2) were scraped off and put in methanol (MeOH). The MeOH with HOPG chunks was subjected to sonication with an ultrasonic horn (UP400S, Hielscher Ultrasound technology) for 3 hours at an amplitude of 80 % and a pulse cycle of 0.5. Small volumes (3 ml) were used in long small tubes to maximize the exfoliation efficiency. Flake suspensions could be used as such for reactions in fluid or the suspensions were dropcasted on Si substrates for surface chemical reactions. Dropcasting was done on a hotplate at 70 °C to speed up evaporation of the MeOH and prevent contraction of evaporating fluid.

4.3 Non-covalent functionalization

Non-covalent functionalization of graphene-like flakes is very interesting since this provides a possibility to functionalize the flake surface without disrupting the sp^2 hybridized structure. None of the σ- or π-bonds of the graphene lattice are broken meaning that the excellent electrical conductivity is maintained after functionalization. It should be noted however that there can be doping effects from the decorating groups on the graphene for example by charge transfer.

The non-covalent functionalization of graphene is based on the observation of a strong interaction of aromatic molecules on graphite [145,202] and was used to decorate CNT [203] before it was applied on graphene. Non-covalent functionalization of graphene is mostly employed to improve the solubility and handling abilities of graphene without loss of electrical properties. It is a popular tool in the development of graphene-based electrodes for photovoltaic devices [146,147,162].

4.3.1 Method

The molecule 1-pyrenedecanoic acid (PDA) was chosen because the non-covalently interacting group is similar to 1-pyrenebutanoic acid succinimidyl ester, which is known from literature. The decanoic acid chain was chosen because it is similar to the previously used 10-undecenoic acid (fatty acid) molecule. The PDA structure is given in Figure 4-1. The goal was to bind DNA by using the same EDC-coupling described in the chapter on the functionalization of CNW.

PDA powder was dissolved in MeOH and chloroform ($CHCl_3$) to a concentration of 5 mM and 3 mM, respectively. A variety of reaction setups was tested. The solution was dropcasted on Si substrates covered with flakes or on HOPG samples. Alternatively, samples were completely submerged in PDA solution. Samples were incubated for 1 h at room temperature. The samples were rinsed by submerging them in MeOH or $CHCl_3$ for 30 min.

Other experiments involved the addition of PDA solution to suspensions of flakes. These suspensions could be dropcasted on Si substrates after incubation or they could be washed by centrifugation steps (12000 rpm for 20 min, pellet was kept to work with and supernatant was removed).

The EDC coupling reaction was also performed in a variety of setups. After the PDA reaction, the EDC coupling was carried out on dropcasted flakes or on suspensions of flakes. Furthermore, tests were done where DNA was coupled to PDA via EDC before this mixture was added to the graphene-like flakes.

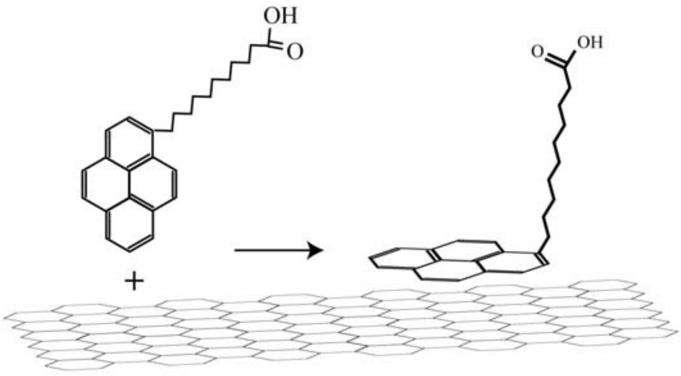

Figure 4-1. 1-Pyrenedecanoic acid structure and π-stacking to graphene.

Pyrene-1-boronic acid (PBA) was used in addition to PDA to facilitate coupling detection with XPS. The presence of the boron element should unambiguously prove the presence of PBA. PBA was dissolved in $CHCl_3$ to a concentration of 2.5

mM. Incubation and rinsing was similar to PDA. PDA and PBA were bought from Sigma-Aldrich (Bornem, Belgium). The structure of PBA is given in Figure 4-2.

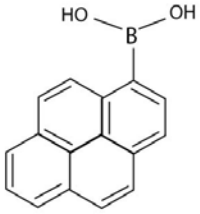

Figure 4-2. Pyrene-1-boronic acid

4.3.2 Results on non-covalent functionalization

Binding results were investigated with confocal fluorescence microscopy (CFM), fluorescence spectroscopy and XPS.

An example of results obtained with CFM is presented in Figure 4-3. The matching samples were made by coupling DNA to PDA in MeOH solution, followed by the addition of this mixture to a substrate with dropcasted flakes. The black coloured areas in the images correspond to the flakes, as these are absent in the reference sample without flakes (Figure 4-3 D). The flakes in these CFM images show no fluorescence, although there is some fluorescence on the substrates coming from adsorbed DNA. No difference can be observed between the sample that should be functionalized (Figure 4-3 A) and the reference samples where no EDC (Figure 4-3 B) or PDA (Figure 4-3 D) was added. The background signal on the bare substrates is coming from adsorbed DNA as this fluorescence can be bleached, see Figure 4-3 E.

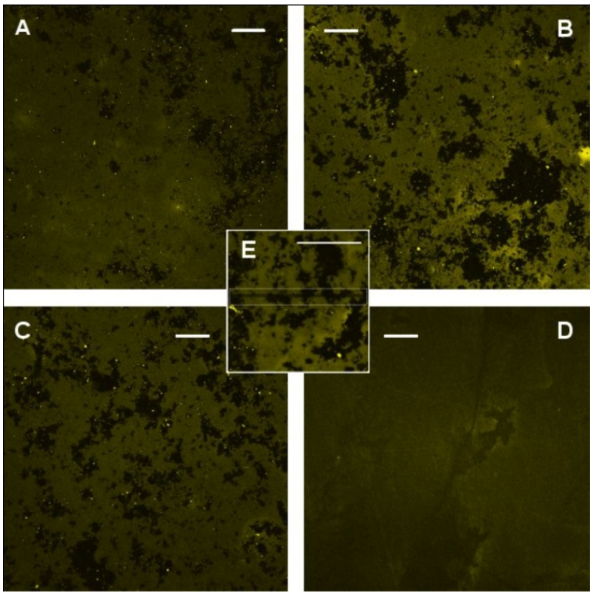

Figure 4-3. CFM images of (A) flakes functionalized with PDA and DNA, (B) EDC-negative reference, (C) PDA-negative reference, (D) Flake-negative reference. (E) shows a higher magnification of the EDC-negative sample with bleached bar. The scale bars correspond to 100 µm.

These results indicate that there was no DNA coupling on the flakes or that the fluorescence is not detectable. It is known that fluorescence can be quenched by the aromatic structure of graphite and graphene-like materials [151,171,204].

The possibility of fluorescence quenching by the flakes was further investigated by fluorescence spectroscopy. Furthermore, investigation focused on the basic step in the reaction scheme, which is the non-covalent coupling of PDA to graphene-like materials. The fluorescing properties of the PDA molecule itself are used to investigate possible quenching by graphene. PDA has an excitation wavelength of 340 nm and emission peaks at 376 nm, 396 nm, 415 nm and 440 nm in MeOH. Emission spectra were measured at different times after the mixing of PDA and flakes in MeOH. The results are given in Figure 4-4.

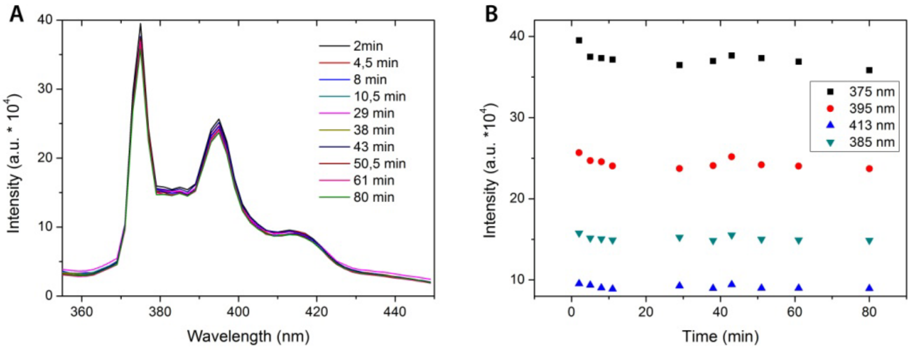

Figure 4-4. (A) Emission spectra of PDA taken at different times after the addition of flakes. Excitation wavelength 340 nm. (B) Fluorescence intensity of selected wavelengths plotted against time.

The emission spectra nicely show the emission peaks of PDA and fluorescence is still high after 80 min. The fluorescence intensities at selected wavelengths, like the emission peak wavelengths, are plotted as a function of time to facilitate the interpretation, see Figure 4-4 B. There is a small decrease in fluorescence intensity after 80 min compared to the intensity at time zero. This decrease has a maximum of 10 % at 375 nm. It should be noted however that the measurement was hampered by the sinking of the flakes to the bottom of the cuvette. This sinking interferes with the fluorescence intensity as flakes reflect and scatter incoming and outgoing light. It was tried to keep the concentration of flakes constant by shaking the cuvette immediately before each measurement. Furthermore, the first spectrum was only taken after 2 min. It is possible that there was a larger quenching effect during the first seconds and minutes. The fact that at least 90 % of the fluorescence maintains after 80 min of incubation might be due to saturation of the flakes with PDA molecules. So it is possible that the flakes reached their maximum PDA binding capacity in a time scale of 2 minutes, before the first spectrum was taken.

Another fluorescence based experiment was set up to investigate the non-covalent functionalization of flakes with PDA and DNA. Three solutions were prepared: one with all reagents (flakes, PDA, EDC and DNA), one without PDA and one without EDC. The latter two serve as reference samples. Each solution contained an equal mass of carbon flakes coming from the same ultrasonicated suspension. The EDC-reaction was carried out first (in H_2O:MeOH 3:7, at 35 °C), followed by the addition of flakes to the solution. After incubation, the three samples were centrifuged 15 times in different washing fluids (MeOH, 2x SSC + 0.5 % SDS, PBS and H_2O). The supernatant of each centrifugation step was kept to analyze with the fluorescence spectrometer. This enabled the indirect detection of PDA and DNA coupling to graphene-like flakes by analyzing the washed unbound material. The supernatants of the three different samples were compared. The results are presented in Figure 4-5.

The left spectra from Figure 4-5 show the emission peaks of PDA and the right spectra show the emission of the Alexa 488 label that is attached to DNA strands. The spectra in A and B are taken from supernatants of specific washing steps of the sample with all reagents (positive sample). It is clear that most PDA is rinsed off in MeOH and most DNA in the SDS mixture. This demonstrates that washing is strongly depending on the combination of the material-to-rinse and the rinsing fluid. The black curve in A and B represents the spectrum of the reaction mixture after the first centrifugation. This is not yet a washing step but it is the actual reaction fluid without the flakes, as the latter are concentrated in the pellet. This mixture was diluted 4 times to avoid saturation of the spectrometer.

Spectra C and D compare the supernatant of the positive sample with the reference samples after the first washing step, which was in MeOH. The fluorescence intensity of the positive sample is lower than the references suggesting that less material is washed off and more material is bonded. This difference between the positive and reference samples is neutralized however by the first rinsing step in SDS (third rinsing step in total), as shown in spectra F.

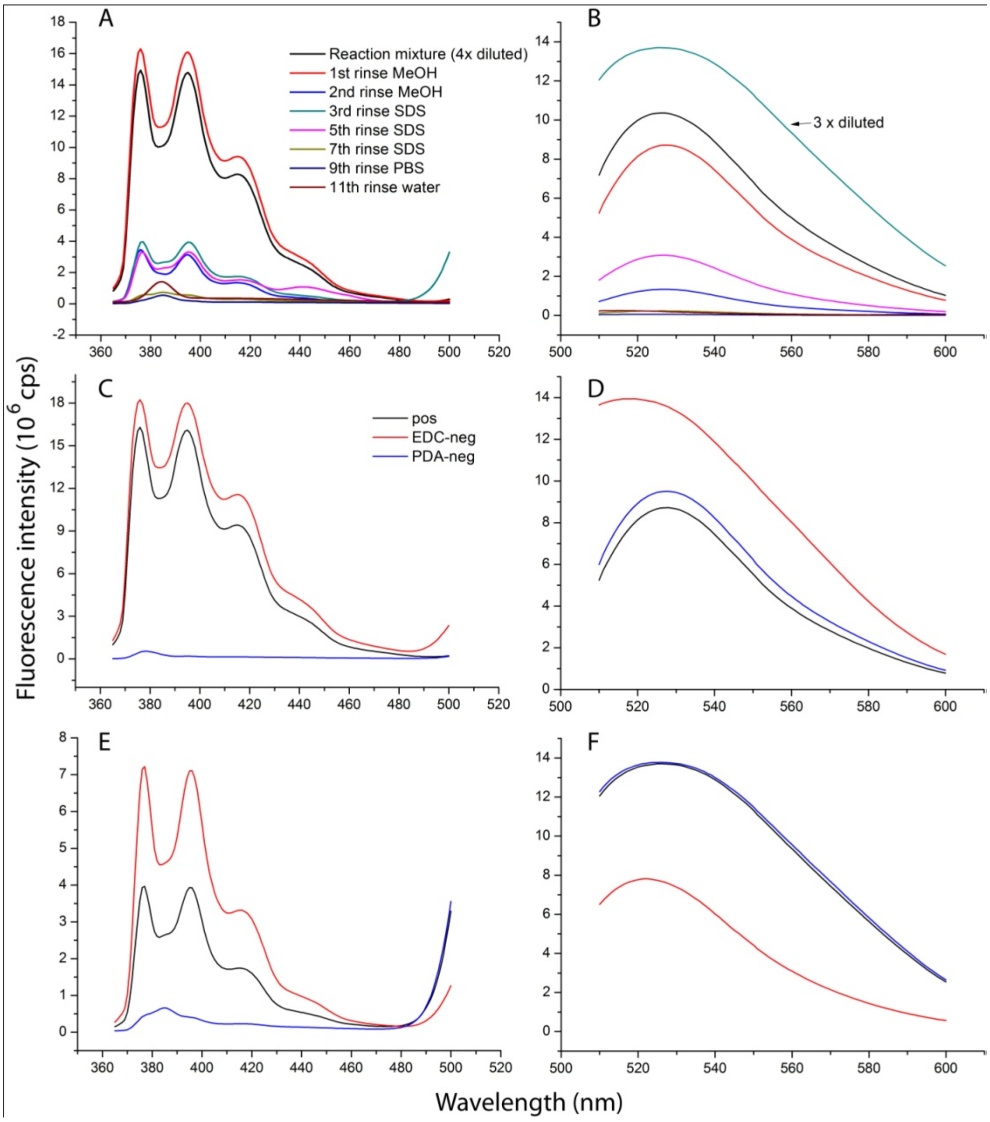

Figure 4-5. Fluorescence emission spectra of centrifugation supernatants. Spectra in the left column were taken at PDA signature wavelengths (λ_{EX} = 340 nm). The right column shows spectra taken at the Alexa fluor label signature wavelengths (λ_{EX} = 488 nm). (A, B) show spectra taken after different washing steps of the positive sample. (C, D) spectra compare the supernatants of the first washing step (in MeOH) of the positive sample with the references. (E, F) spectra are taken after the third rinsing step (in SDS).

It can be estimated how much PDA and DNA were rinsed off in total for each sample. These estimated values are shown in Figure 4-6. Estimations are made by taking the fluorescence intensity at a certain wavelength (527 nm and 376 nm for DNA and PDA, respectively) for each sample after each washing step and multiplying it by the supernatant volume of that washing step. This gives a value that is analogous to an amount of material. The values of all the washing steps are added up for each sample. This is the value that is given in Figure 4-6.

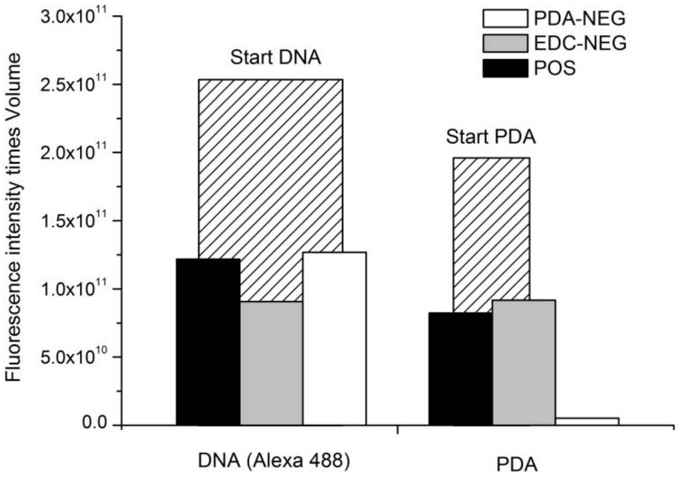

Figure 4-6. Comparison of the total amount of material that was rinsed off from the different samples. The amount of material that was added in the beginning of the reaction is also given. The y-axis respresent an arbitrary scale derived from multiplying the fluorescence intensity and volume of the supernatant.

If one compares the amount of material that was rinsed off and the amount that was added to perform the reaction, only about half of the starting material is rinsed off. This could indicate that the other half is bonded to the flakes. However, these results also point to the EDC-negative sample as the one with the lowest amount of rinsed off DNA and therefore the highest amount of bonded DNA. This does not seem logical as the EDC is required to couple DNA to PDA. The PDA negative sample has the same ratio of rinsed off to start DNA as the positive sample. These results are contradicting each other and the origin of these odd results is not clear.

A final attempt to prove the non-covalent coupling of pyrene-like molecules to the basal plane of graphene-like materials was taken by investigating the coupling by XPS. PDA, dissolved in both MeOH and $CHCl_3$, was incubated on freshly cleaved HOPG samples and Si substrates with flakes. Samples were rinsed with the solvent in which PDA was dissolved (MeOH or $CHCl_3$). XPS analysis could not prove the presence of the PDA molecule on the rinsed samples. In order to enhance coupling detection, HOPG samples were incubated with the similar molecule PBA, which contains boron. PBA was dissolved in $CHCl_3$, followed by a short rinsing step. The results are presented in Figure 4-7. Again, no coupling can be observed as the B_{1s} peak does not rise above contamination levels. The present contaminants (Na, Zn, Cu, Sn, S and Cl) are probably originating from anhydrides present in the PBA powder.

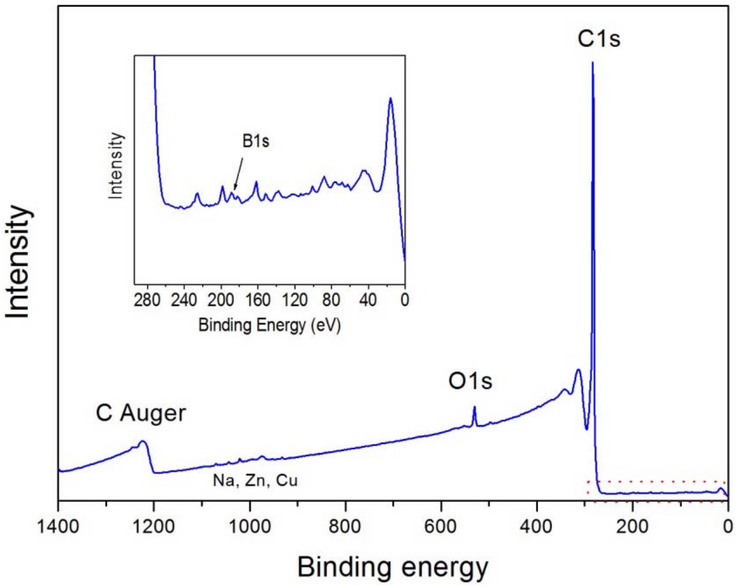

Figure 4-7. XPS spectrum of HOPG incubated with pyrene-1-boronic acid. Inset shows a magnification of the area indicated by the dotted square. The B 1s peak is indicated by the arrow. The boron level does not rise above the contamination level.

4.3.3 Conclusion on non-covalent functionalization

Efforts were made to functionalize the basal plane of graphene-like flakes in a non-covalent way. The pyrene moiety of PDA and PBA was used for π-stacking interactions on the sp^2-hybridized structure. The goal was to use these pyrene-based molecules as linkers for the attachment of DNA strands. Confocal fluorescence microscopy was applied to detect and visualize the presence of fluorescently labeled DNA. This method did not show any sign of DNA attached to the flakes. As graphene-based materials are able to quench fluorescence coming from nearby sources, other detection methods were tested. Fluorescence spectroscopy was used to investigate potential quenching effects and to analyze binding in an indirect way. The indirect detection involved the characterization of unbound PDA and DNA in washing fluids. These fluorescence spectroscopy based experiments could also not give clear indications that PDA and DNA were coupled to the graphene-like flakes. Finally, XPS characterization made it clear that there was (almost) no PDA or PBA present on "functionalized" samples after gentle rinsing. This indicates that the non-covalent π-π interaction between small aromatic molecules and graphene is not strong enough to withstand even delicate rinsing.

Non-covalent functionalizations of graphene-like materials described in literature did not perform rinsing steps to remove excess material. Most publications employ non-covalent functionalization as a means of dispersing or solubilizing graphene flakes [146,147,162]. They were not interested in the presence of the decorating material after rinsing steps or device fabrication. One publication on non-covalent functionalization on CNT demonstrated the presence of the decorating molecule after washing [203]. The curvature of the CNT might render them more susceptible for non-covalent functionalization compared to flat graphene. This chapter suggests that non-covalent interactions are not suited for attachment of biological receptor molecules that are meant to stay attached during handling and later use in sensing experiments.

4.4 Covalent functionalization

The development of robust reusable DNA sensors requires the strong binding of probe DNA strands to the graphene surface. Therefore it is attempted to covalently bind DNA strands to the basal plane of graphene-like materials.

Almost all in-plane covalent functionalizations use graphene oxide as starting material. As graphene oxide is an insulator and reduction of oxidized graphene does not fully restore the conducting properties of graphene, these are not really suited for the development of electrical response sensors. The only covalent functionalization of pristine graphene that is known from literature is with diazonium salts. Although the covalent functionalization of the basal plane always damages the conducting sp^2 hybridized structure, damage will be limited compared to fully oxidized graphene. Each introduction of a defect also means a desired functionality. There are no excess defects introduced that are not used in a later stadium. Of course, the fact that there is no need to oxidize the graphene first and reduce it later is a big advantage in itself.

Like many functionalizations of graphene, this method was first used on CNT [137,205-211]. There are two approaches to this method. One approach is to let preformed diazonium react with the CNT [137,205,206] and the other approach is the in situ generation of the diazonium compound from its precursors followed by immediate reaction with CNT [137,207-209]. The approach with the premade diazonium was used in the case of graphene-like flakes [97,102,134-136,138] and this was also the approach used in this thesis.

It was already mentioned in the introduction that there is a debate regarding the nature of the bond between diazonium and graphene. Farmer and coworkers suggested that the bond is not covalent as they found that attachment of diazonium did not suppress the conductance of graphene. But they also state that the bond is stronger than regular van der Waals adsorption, based on spectroscopic results [138]. Koehler and coworkers proposed a two-step reaction mechanism for diazonium coupling. The first step involves the adsorption of the diazonium molecule on the graphene sheet, resulting in an intermediate complex. The actual covalent binding to the graphene sheet happens in a second step. They state that this second step takes place quickly (few minutes) on single layer graphene, especially at the edges, and slowly on bilayer graphene and thicker flakes. The second step might even not occur at all on bilayer and multilayer graphene. Therefore, the diazonium coupling should be selective for single layer graphene [134]. Other results based on Raman spectroscopy clearly indicate a regular covalent bonding [136].

4.4.1 Diazonium salts

Diazonium salts are a group of organic molecules that contain a reactive group with the following composition: $R\text{-}N_2^+ X^-$. R can be an alkyl chain or an aryl, X is an organic or inorganic anion. Diazonium molecules that are used in this work, and in most publications on graphene functionalization, are of the aryl type, meaning that they contain an aromatic ring. The general structure of an aryl diazonium salt is shown in Figure 4-8.

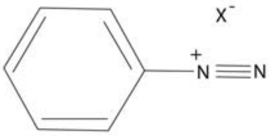

Figure 4-8. Structure of an aryl diazonium salt. X is an (in)organic anion.

The diazonium molecules are actually used as linker molecules to attach DNA to the graphene. Diazonium compounds with different para-substituted functional groups were used. The goal is to use the previously described EDC-coupling method to bind amino or carboxyl-labeled DNA strands to the functional groups of the linker molecules. Therefore, diazonium coupling should provide a carboxylic acid group or an amino group as anchor point to attach DNA.

4.4.2 4-nitrobenzene diazonium tetrafluoroborate

The first diazonium compound that was tested was 4-nitrobenzene diazonium tetrafluoroborate (Sigma-Aldrich, Bornem, Belgium). Attachment of this diazonium molecule to graphene sheets results in nitro groups. These nitro groups need to be converted into amino groups in order to use the EDC-binding protocol, see Figure 4-9 and Figure 4-10.

Binding method

Methanol was purged with N_2 gas, followed by the addition of 4-nitrobenzene-diazonium tetrafluoroborate powder to a final concentration of 5 mM. When all the powder was dissolved, the solution was added to a three-neck flask. Si samples with graphene flakes, deposited via the Geim method or dropcasting, were also added and the flask was kept under N_2 atmosphere. The reaction was incubated for 1 hour at room temperature under constant stirring. The reaction scheme is shown in Figure 4-9. The diazonium compound reacts with graphene and N_2 splits off and escapes as gas from the reaction. After the reaction, the samples were rinsed shortly with water (3 x 5 min), IPA and N_2 blow dried.

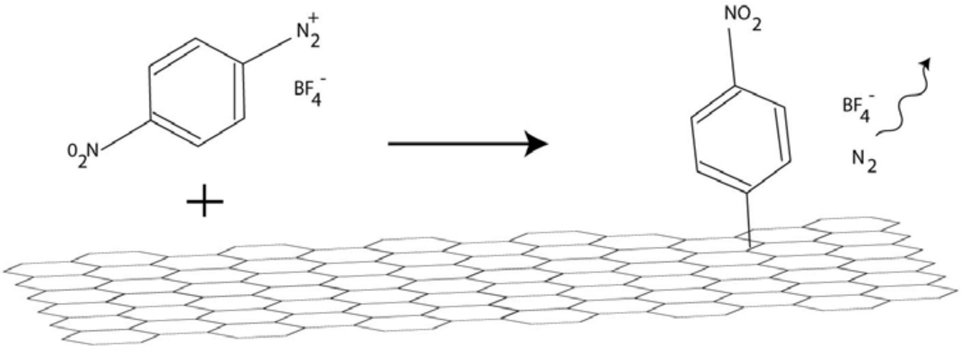

Figure 4-9. Illustration of 4-nitrobenzene diazonium tetrafluoroborate coupling to graphene. The byproducts N_2 and BF_4^- escape as gas and are rinsed off, respectively.

Conversion of the nitro group to an amino group

The nitro group of the nitrophenyl linker has to be converted into an amino group in order to bind DNA strands. This conversion was done via a Bechamp reduction. This reaction specifically reduces aromatic nitro compounds into aromatic amino compounds (anilines) and it involves the reduction with iron (Fe) in acidic environment, see Figure 4-10.

Iron in the form of powder (Sigma-Aldrich, Bornem, Belgium) was used as reducing agent. The reaction was done in the following way: a glass beaker was filled with 20 ml of water, 5 g of Fe powder and 3 ml of HCl (37%). Immediately after the addition of HCl, the mixture starts to fizz and the sample was added after a few seconds. The mixture was incubated for 2h at 50 °C.

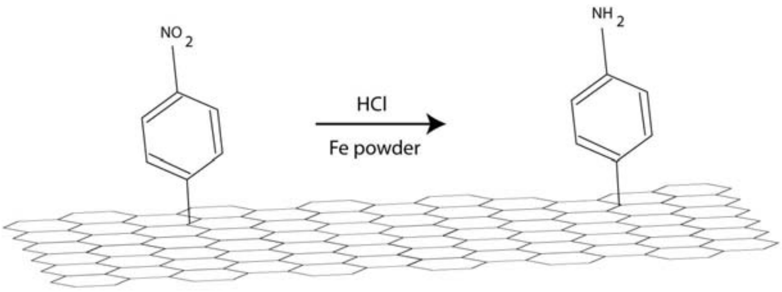

Figure 4-10. Bechamp reduction to convert the nitro group into an amino group.

The samples were thoroughly rinsed with water after the reaction. However, it was found that the Fe could not be totally removed with water. As a result, the sample was contaminated with Fe after this step, which was revealed by XPS measurements (not shown in the thesis).

Results

Raman spectra, taken on selected single layer graphene flakes, are presented in Figure 4-11. The Raman spectra were collected on pristine graphene (Reference), after the diazonium coupling (Nitrobenzene diazonium) and after the conversion reaction to reduce nitro groups into amino groups (Reduced 1 and Reduced 2). Two spectra of the reduced form are shown because of their different appearance. Figure 4-11 (A) shows the whole spectral range of interest with the characteristic graphene peaks, namely a G peak and 2D peak around 1585 cm^{-1} and 2640 cm^{-1}, respectively. The 2D peak has a full width at half maximum (FWHM) of about 30 cm^{-1} and no shoulders can be observed. Together with the absence of a D peak in the reference sample, all these signatures point to good quality single layer graphene.

After the functionalization reaction, some peaks, linked to the nitrobenzene diazonium, appear in the 1050 cm^{-1} – 1550 cm^{-1} region (shown in Figure 4-11 (B)). Furthermore, the G peak (Figure 4-11 (C)) shifts towards 1590 cm^{-1}, indicating a doping effect, and a shoulder becomes visible at 1597 cm^{-1}. This shoulder is called the D’ peak and points to lattice defects. It is not clear whether a D peak, the main defect related peak, is present. Its potential presence is masked by the diazonium related peaks. Figure 4-11 (D) shows that the FWHM of the 2D peak is unchanged but its position shifts to 2648 cm^{-1}, corresponding to p-doping.

The conversion reaction to the reduced form results in the disappearing of the diazonium related peaks in the 1050 cm^{-1} – 1550 cm^{-1} region. A D peak becomes visible at 1325 cm^{-1}. Depending on the flake that was measured, this D peak is very small (Reduced 1) or relatively high (Reduced 2). The G peak and 2D peak remain unchanged after the conversion step.

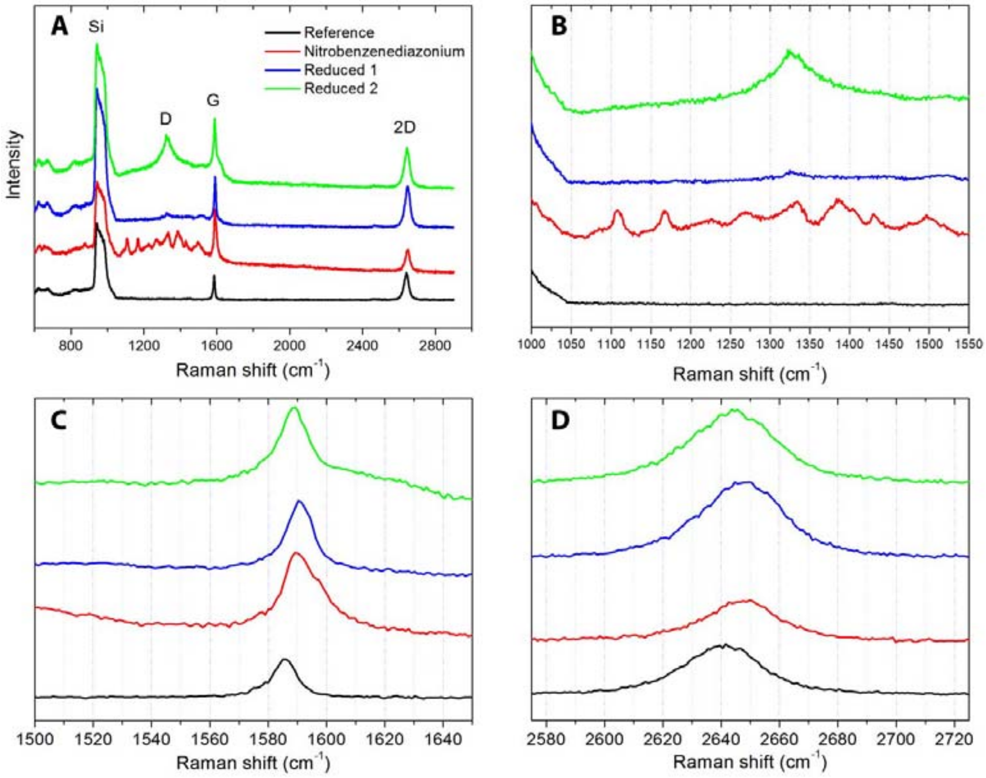

Figure 4-11. Raman spectra of graphene flakes before and after functionalization with nitrobenzene diazonium and subsequent reduction of the nitro group to an amino group. (A) shows an overview of the spectrum. (B, C and D) give an enlarged view of the D peak, G peak and 2D peak, respectively.

The conversion reaction seems to remove (some of) the diazonium, as the diazonium related peaks disappear in the Raman spectra. Therefore, it is not clear whether the diazonium is really bonded or merely physisorbed. The appearance of a D peak however, is a clear sign of lattice defects. These lattice defects are probably the result of covalent functionalization, whereby sp^2 bonds are converted into sp^3 bonds. Alternatively, the D peaks could be a result of the conversion reaction itself. In this case, the acidic conditions would damage the graphene structure. This alternative explanation for the D peak is unlikely, considering the good chemical stability of graphene. A plausible explanation would be that part of the diazonium is covalently coupled and part of it is physisorbed to graphene.

In addition, HOPG samples, functionalized with nitrobenzene diazonium, were also characterized with XPS before and after the conversion reaction. The XPS N 1s core peak spectral region is shown in Figure 4-12. The dark curve, taken before the conversion reaction, shows two different peaks. The peak at 405.8 eV corresponds to the oxidized nitrogen of the nitrogroup. The assignment of the other peaks is more difficult. It is assumed that the peak at 400 eV (dark curve) corresponds to the nitrogen of the diazo ($-N^+\equiv N$) functionality. The presence of this diazo functionality means that part of the diazonium is physisorbed on the HOPG, since covalent coupling is accompanied by the removal of this N_2 group. A comparison of the areas under the curve for both peaks (5100 and 4000 for peaks at 405.8 eV and 400 eV, respectively) results in a fraction of ~ 40 % of the present molecules that is adsorbed and ~ 60 % that is covalently bonded, keeping in mind that for each molecule there are two N atoms contributing to the peak at 400 eV.

The grey curve in Figure 4-12 represents the spectrum taken after the conversion reaction to the reduced form. It is clear that the peak related to the nitro group has almost completely disappeared, in agreement with the chemical reduction of this nitro group. The peak around 400 eV is shifted to lower binding energies by ~ 0.7 eV. This is also consistent with the chemical reduction of nitrogen species. However, the actual assignment of this peak to specific oxidation states of nitrogen is difficult. The peak could be linked to a slightly reduced form of the diazo functionality, to nitrogen from amino groups or to a combination of these possible explanations. It should be noted that XPS characterization of freshly cleaved HOPG did not show any nitrogen peaks, meaning that the peaks observed here do really originate from the diazonium species.

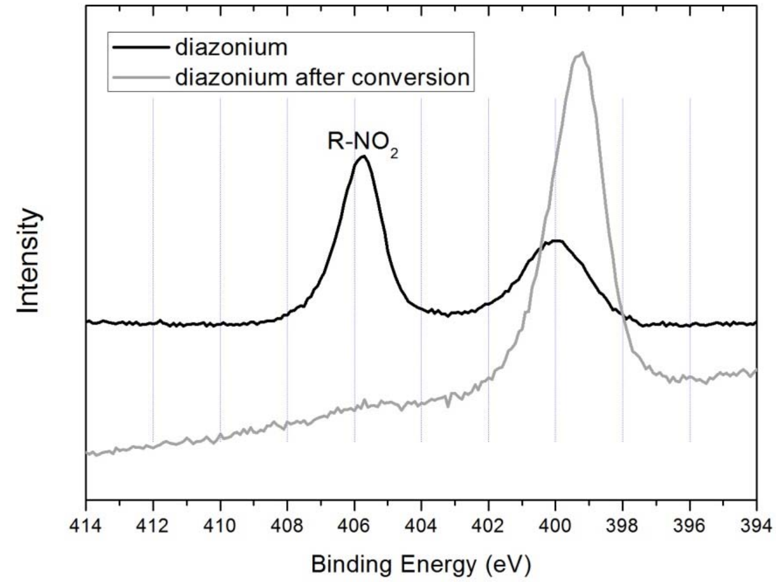

Figure 4-12. N 1s XPS spectra of HOPG functionalized with diazonium. Spectra were recorded before and after the conversion reaction of NO_2 to NH_2.

4.4.3 4-Benzoic acid diazonium tetrafluoroborate

As the nitrobenzene diazonium required an additional reduction reaction to yield amino groups, a second type of diazonium was tested in order to avoid this extra reaction step. 4-Benzoic acid diazonium tetrafluoroborate was used because the coupling of this species results in carboxylic acid groups that can be used in EDC-mediated DNA coupling without further modifications. The chemical structure of this diazonium species is shown in Figure 4-13.

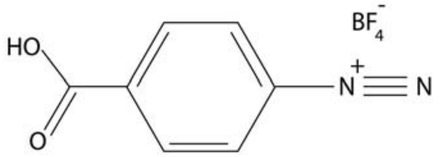

Figure 4-13. 4-Benzoic acid diazonium tetrafluoroborate.

Diazonium preparation

The 4-benzoic acid diazonium tetrafluoroborate was homemade, following two different synthesis routes.

The first route was done by following the synthesis described in references [212,213], this route will be called the isoamyl nitrite route.

First, 0.4 g (2.92 mmol) of 4-aminobenzoic acid was dissolved in 1 ml ethanol, followed by the addition of 0.65 ml aqueous tetrafluoroboric acid solution (48 %). The mixture was cooled on ice and 0.46 ml (3.4 mmol) of isoamyl nitrite was added dropwise. The mixture was incubated for 1 hour under stirring and cooling in the ice bath. After the incubation, diethyl ether was added until precipitation was observed. The solution with precipitate was filtered over a cellulose filter (Grade 1, particle retention: 11 µm, Whatman, 's Hertogenbosch, the Netherlands). The precipitate was dissolved in acetone and reprecipitated in diethyl ether to purify the powder. Finally, a second filtration yielded a light red/brown powder. The synthesized powder was stored in the fridge. 4-Aminobenzoic acid, aqueous tetrafluoroboric acid, isoamyl nitrite and ethanol were purchased from Sigma-Aldrich (Bornem, Belgium). Diethyl ether and acetone were technical grade and purchased from VWR (Haasrode, Belgium).

The second route was performed according to references [214,215] and this route will be called the sodium nitrite route.

First, 2.74 g (0.02 mol) of 4-aminobenzoic acid was dissolved in 28 ml of warm water, followed by the addition of 4.5 ml of HCl (37 %). The mixture was cooled to below 0 °C and 1.52 g (0.022 mol) of sodium nitrite, dissolved in 8 ml of cold water, was added dropwise. The solution was filtered over a cellulose filter. Sodium tetrafluoroborate (2.41 g or 0.022 mol), dissolved in 8 ml of cold water, was added to the filtrate. After cooling to below 0 °C, the mixture was filtered again, resulting in a white powder. The powder was washed with cold water and ether. Chemicals were purchased from Sigma-Aldrich (Bornem, Belgium).

The diazonium powder was characterized with infrared spectroscopy using a Tensor 27 from Bruker (Evere, Belgium). The spectrum, shown in Figure 4-14, contains the diazonium-functionality related peak at 2307 cm^{-1} and 2290 cm^{-1}, respectively [216]. The peak at 1045 cm^{-1} is related to the tetrafluoroborate. Some peaks (~3300 cm^{-1} and 1700 cm^{-1}) related to the carboxylic acid group are also indicated on the spectrum. The fact that the two spectra are not identical probably results from different purity levels.

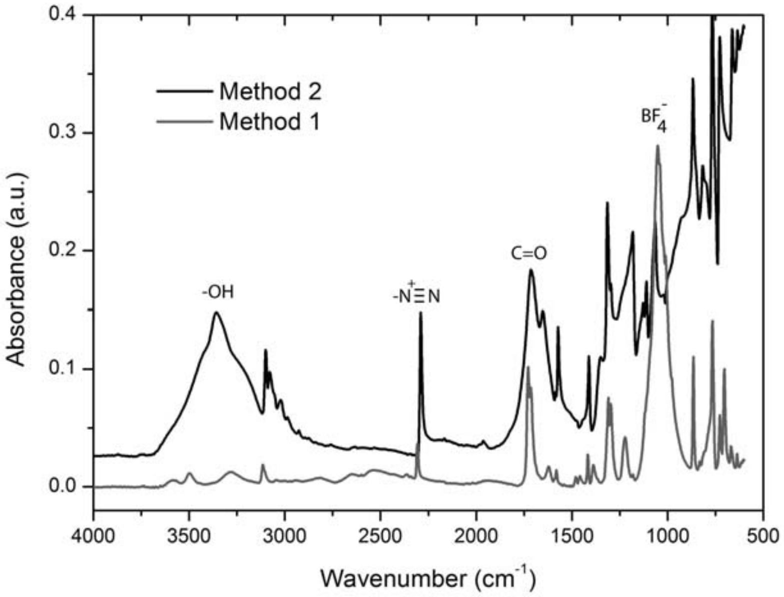

Figure 4-14. Infrared spectra of the 4-benzoic acid diazonium tetrafluoroborate, prepared by two different methods.

Binding method

The diazonium coupling reaction was carried out similar to the nitrobenzene diazonium coupling. In addition to similar reaction conditions, a higher concentration and longer incubation time were tested. Furthermore, the coupling reaction was also performed with cooled MeOH and later heated to 45 °C. The higher concentration was 8.7 mM with an incubation time of 2.5 hours (starting with a solution of ~4 °C, after 1 hour, the reaction mixture was heated to 45 °C). However, this higher concentration and longer incubation time did not improve binding results. The samples were rinsed in MeOH (5 min), water (2 x 10 min), isopropyl alcohol (IPA) (1 min) and finally blown dry before further use in EDC coupling.

EDC-mediated DNA coupling

The carboxylic acid group of the diazonium molecule, actually a benzoic acid after attachment to the graphene, is used in an EDC-mediated reaction to couple amino-labeled DNA strands. This EDC mediated coupling was already described in Chapter 3 on functionalization of CNW. The DNA used in combination with diazonium prepared by the isoamyl nitrite route was single stranded DNA, 8 nucleotides long, with amino-modification and fluorescent 6-FAM label at the 5’ end and 3’ end, respectively. Diazonium salt prepared by the sodium nitrite route was combined with single stranded DNA, 36 nucleotides long, with amino-modification at the 5’ end. Rinsing steps are described in detail in the following section on results.

Results

The samples functionalized with 4-benzoic acid diazonium and DNA were also investigated with Raman spectroscopy. Figure 4-15 shows the spectra of samples functionalized with diazonium salt prepared by the isoamyl nitrite route. Spectra from a pristine reference flake (Reference), a flake coupled with diazonium (Diazonium), a flake coupled with diazonium and DNA (EDC-POS) and an EDC-negative reference (EDC-NEG) are shown. This EDC-negative sample was coupled with diazonium but the DNA binding reaction was carried out without the EDC mediator. The EDC-negative flake is likely to be bilayer graphene as deduced from the broad 2D band.

The Raman spectrum of the diazonium coupled sample shows features that are similar to the nitrobenzene diazonium coupling. The G peak and 2D peak are slightly red shifted, due to doping, and the region between 1100 cm^{-1} and 1550 cm^{-1} contains a number of diazonium related peaks. Some of these benzoic acid diazonium related peaks are identical to the peaks from nitrobenzene diazonium while others are different. This is in agreement with the resembling chemical structures of the two diazonium species.

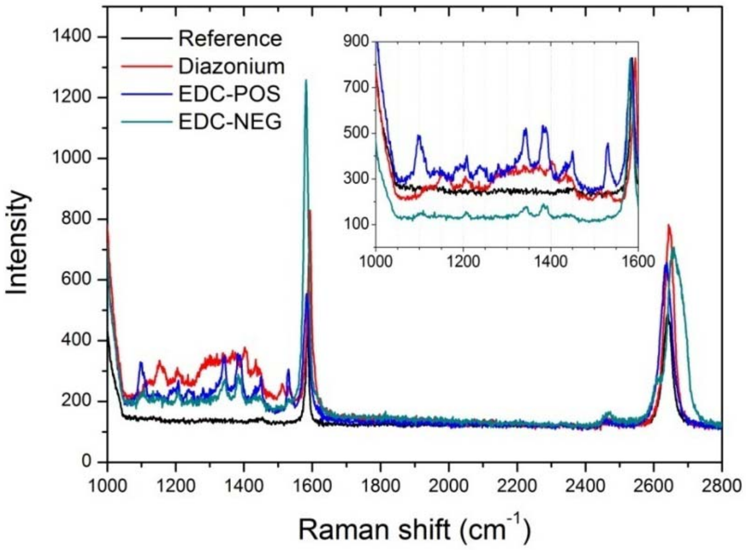

Figure 4-15. Raman spectra of graphene flakes functionalized with benzoic acid diazonium (method 1) and DNA. Inset: enlargement of the 1000 – 1600 cm^{-1} region with the spectra rescaled to the G peak intensity.

The binding of DNA strands results in the appearance of new peaks in the 1050 cm^{-1} – 1550 cm^{-1} region, as shown in the inset of Figure 4-15. The spectra in the inset are rescaled to a uniform G peak intensity in order to compare the DNA related peaks of the EDC-pos and EDC-neg sample. By comparing these two samples, it can be seen that the DNA related peaks (~ 1100 cm^{-1}, ~ 1340 cm^{-1} and ~ 1380 cm^{-1}) are much higher for the EDC-pos sample. The EDC-neg sample shows the same main features but in much lower intensities. It should be noted however, that it is tricky to compare the EDC-pos and EDC-neg sample in this case as they are single layer and bilayer, respectively. Single layers and bilayers could show different chemical reactivities.

Raman spectra that were collected in between the flakes, on the Si substrate, did not contain any peaks apart from the Si-related ones. This means that the diazonium and DNA selectively bind (or adsorb) to the carbon flakes.

The samples shown in Figure 4-15 were rinsed, after DNA coupling, in PBS, SSC, water and IPA. There were 8 rinsing steps in PBS for a total of 28 hours, mostly at 60 °C – 70 °C. Two rinsing steps in 2x SSC were performed, each 15 min.

Three rinsing steps were done in water for a total of 18 hours. This means that the samples were rinsed 13 times in total and for a total time of 46 hours. Another batch of samples was made, functionalized with diazonium and DNA and rinsed 7 times in PBS (49 hours) and 4 times in water (62 hours). This second batch of samples, which was rinsed 111 hours in total, only showed very small diazonium and DNA related peaks in Raman spectra. However, some samples contained a rather large D peak, while others did not. These results support the statement that part of the diazonium is physisorbed and can be rinsed off (albeit with very long rinsing steps) while another part is covalently bonded, causing the D peak. These results also rule out the acidic conditions, used in the previous section, as the cause of the D peak.

Samples that were functionalized with benzoic acid diazonium prepared by the sodium nitrite route, were rinsed only three times in PBS (30 min each) and 4 times in water (total 3.5 hours of which 2 hours at 60 °C). These samples only had a total rinsing time of 5 hours, compared to the 46 hours for the isoamyl nitrite route. Despite this shortened rinsing time, almost no diazonium or DNA related peaks can be observed in the Raman spectra, shown in Figure 4-16.

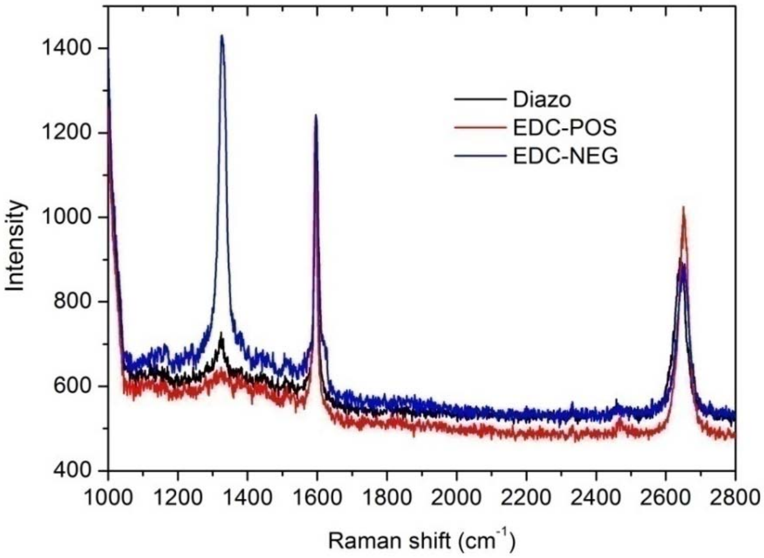

Figure 4-16. Raman spectra of graphene flakes functionalized with benzoic acid diazonium (Sodium nitrite route) and DNA. Spectra are rescaled to G peak intensity.

Although no real diazonium or DNA peaks can be observed, the spectra show clear D peaks, for the EDC-neg sample even higher than the G peak. This is again a proof for the covalent attachment of the diazonium. It is assumed that DNA is also present, covalently bonded to the diazonium linker, but stays undetected by the Raman spectroscopy measurements. This assumption is based on experiments where diamond (not shown in this thesis) and amorphous carbon (Chapter 5) samples were functionalized with the homemade diazonium, followed by EDC-mediated coupling of DNA. Confocal fluorescence microscopy confirmed the presence of bonded fluorescently labeled DNA strands on both types of samples. As the attachment of DNA to the diazonium linker is the same in all sample types, it is assumed that this reaction also worked on graphene samples. Strong reflection and potential fluorescence quenching made it impossible to detect fluorescently labeled DNA on graphene flakes using confocal fluorescence microscopy.

4.4.4 Conclusion on covalent functionalization

Single layer graphene flakes, prepared by the Geim method, were functionalized with diazonium salts. The aim was to use this diazonium as a linker molecule to attach DNA strands covalently to the graphene surface. First, a commercially available diazonium salt was used. As this diazonium required an extra step to chemically reduce the nitro group to an amino group in order to perform EDC coupling, efforts were shifted to a different diazonium type. The latter was homemade and resulted in carboxylic acid groups that could be used directly in an EDC coupling reaction. Raman spectroscopy indicated that at least a part of the diazonium was covalently bonded to the graphene surface, based on the D peak formation. It was also observed that part of the diazonium was physisorbed on the surface, resulting in a few Raman peaks in the 1100 cm^{-1} – 1550 cm^{-1} spectral region. These peaks disappeared after rinsing, indicating the removal of the physisorbed diazonium species. The amount of rinsing, required to remove the physisorbed species, was dependent on the diazonium preparation method. Physisorbed diazonium prepared by the isoamyl nitrite route required much more rinsing compared to diazonium prepared by the sodium nitrite route.

The presence of covalently bonded DNA could not be confirmed. One batch of samples showed some Raman peaks introduced by the DNA but it is not clear whether this DNA was covalently bonded or physisorbed. Other sample batches did not show clear DNA peaks. However, based on experiments on diamond and amorphous carbon, it is very much possible that covalently bonded DNA is present but stays undetected by the used characterization methods.

Chapter 5

Functionalization of amorphous carbon microstructures

Functionalization methods were not only performed on sp^2 carbon materials but also on amorphous carbon. Amorphous carbon lacks long-range crystalline order but shows some short-range order and can be considered as a poly- or nanocrystalline material. It is a mix of sp^2 and sp^3 carbon although with deviating bond distances and angles [20,217]. Despite the fact that amorphous carbon does not possess the exceptional physical properties of graphene-like carbon, it is a very interesting and useful material. Its good electrochemical properties make it a widely used electrode material in sensing applications [218-223] and fuel cells [224,225]. Also, it is often used in medical implants, like artificial heart valves and dental implants, due to its robustness and biocompatibility [219,226-229]. It can withstand high temperatures and has a high thermal conductivity [230]. An especially interesting property for this work is the high amount of dangling bonds, which facilitate functionalization with DNA strands.

The amorphous carbon structures that were used in this work have yet an additional huge advantage in functionalization purposes: the structures are made out of newly developed micro-nano hybrids. The overall dimensions of the structures are in the micrometer range while the surface layer of the structures consists of nanowires. These nanowires result in a huge surface area, ideal for biofunctionalization. The backbones of these structures are made of solid non-porous carbon, providing mechanical strength and electrical conductivity. Furthermore, the microstructures can be made in a variety of 3D shapes which allows for their integration in electrical circuits. A provisional DNA sensor was developed by functionalizing bridge structures with DNA strands and measuring the resulting change in bridge resistance.

5.1 Fabrication of amorphous carbon microstructures

The amorphous carbon microstructures were prepared by Dr. Michael De Volder at IMEC (Leuven, Belgium). As the fabrication process is still confidential at the time of writing, only a very concise description can be given here. The structures were made by patterning layers of a carbon containing photoresist. This was followed by pyrolysis in a nitrogen atmosphere. In addition to the micro-nano hybrid structures, bulk microstructures were produced with the same overall shape and dimensions but lacking the nanostructured coating layer. These bulk microstructures serve as a reference for the micro-nano hybrid structures.

5.2 Morphology of the microstructures

As mentioned above, the structures consist of a solid backbone and a porous nanostructured surface. Figure 5-1 presents a SEM image of the material with a cross-sectional view, clearly showing the solid core (about 5 µm thick) and nanostructured surface (about 3 µm thick).

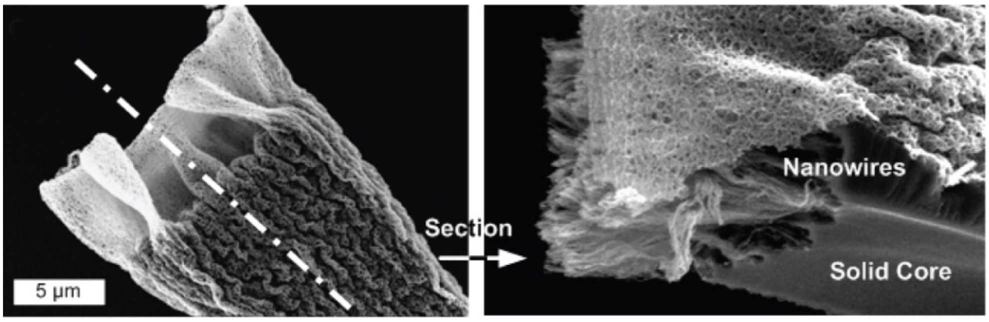

Figure 5-1. Close-up of an amorphous carbon pillar with cross-sectional view showing the solid backbone and nanostructured surface. The cross-section is indicated by the white dashed line. Images were recorded at IMEC.

To confirm that the structures are made out of pure amorphous carbon, the following characterization techniques were applied at IMEC: XPS, Raman and

TEM measurements. XPS characterization revealed carbon as major constituting material with only low levels of oxygen. Raman spectra show a G band and D band characteristic for amorphous carbon [187,231]. The meaning of these Raman bands is given in Chapter 2. TEM measurements did not reveal any long range crystalline order. The characterization results are summarized in Figure 5-2.

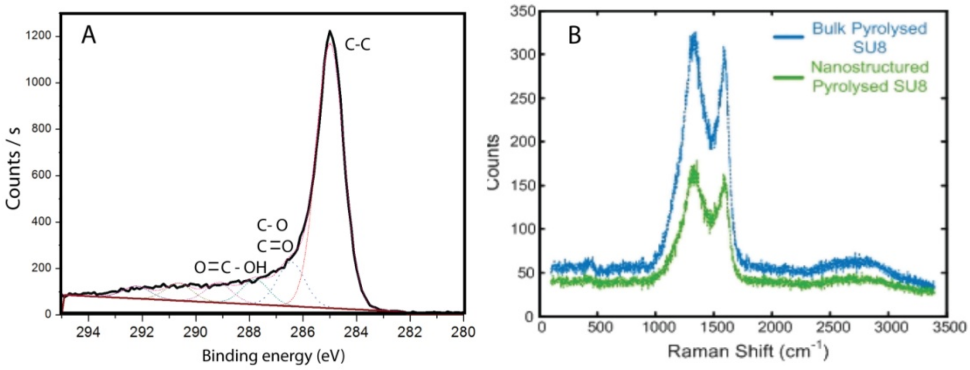

Figure 5-2. (A) XPS spectrum showing the C 1s peak. Only low levels of C-O, C=O and O=C-OH bonds are present. (B) Raman spectra of bulk and nanostructured material, showing D and G peaks.

The overall dimensions of the structures vary from a few tens of micrometers to a few hundred of micrometers. A broad variety of 3D shapes could be made. In addition to the two-leg bridge structures, shown in Figure 5-3, structures with 6, 12 or 180 legs for example could also be produced. The bulk structure, also shown in Figure 5-3, is made from the same material and can be made in the same shapes as the nanostructured ones. Structures that were used in this work, for DNA sensing, are composed of two pillars that touch each other at the top, forming a bridge between two electrodes. Two different examples of the used structures are given in Figure 5-3. The structures are placed on top of electrode arrays made from titanium nitride (TiN) or amorphous carbon. The electrically measured structures are produced in mini-arrays, such as the one showed in Figure 5-3 (C).

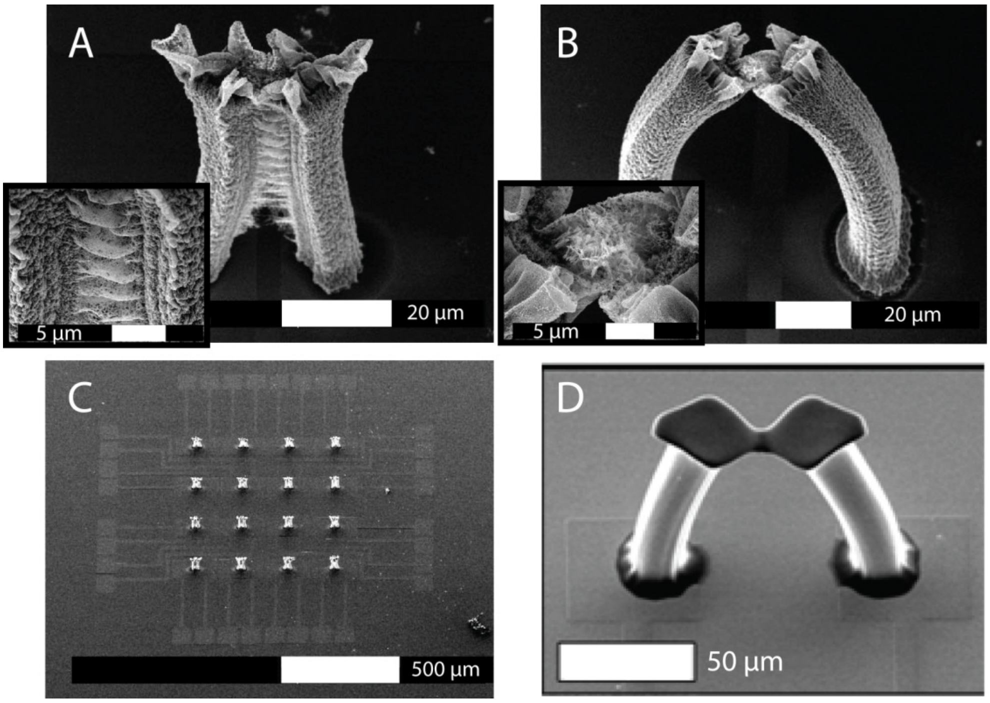

Figure 5-3. SEM micrographs of amorphous carbon microstructures. (A) and (B) show micro-nano hybrid bridge structures with collapsed-like and arch-like shape, respectively. (C) shows a typical array of electrodes with bridge structures on top. (D) portraits a bulk amorphous carbon microstructure .

5.3 Functionalization method

The structures were functionalized with single stranded DNA according to two different methods previously described in this thesis. One method involves the photochemical coupling of a fatty acid linker molecule, analogous to the functionalization of carbon nanowalls (Chapter 3). The other method is based on diazonium coupling analogous to the functionalization of graphene-like flakes (Chapter 4). After attachment of these linker molecules, EDC-based chemistry was applied to couple the amino-modified DNA strands. The EDC-mediated DNA coupling was the same for the two linking procedures. The specifics of the reactions will be shortly described here. It should be mentioned that special care was taken to avoid mechanical agitation during handling of the microstructures because they could detach from the surface upon mechanical disturbance.

Fatty acid coupling

Samples were covered with a liquid film of 10-undecenoic acid and illuminated for 20 h with UV light (254 nm). After binding, excess fatty acid was removed by rinsing with acetic acid (30 min at 95 °C) and Milli-Q water (2 x 30 min at 95 °C + 5 min at room temperature). The samples were dried in air (oven) at 60 °C for 30 min.

Diazonium coupling

4-benzoic acid diazonium tetrafluoroborate was prepared according to the isoamyl nitrite route described in Chapter 4. The homemade powder was dissolved in methanol to a concentration of 5 mM after the methanol was purged with N_2 gas. The dissolved diazonium was added to the samples in a three-neck-flask and the reaction was incubated for 75 min under N_2-atmosphere and gentle stirring. The reaction was performed at room temperature. Afterwards, the samples were rinsed in Milli-Q water (1 h at 95 °C and 2x 1 h at room temperature). Samples were dried in the oven at 60 °C for 30 minutes.

EDC-mediated DNA coupling

The samples with attached linker molecules (fatty acid or benzoic acid) were incubated with a solution of DNA in MES buffer for 15 min before EDC, also dissolved in MES buffer, was added to the reaction. The single stranded DNA was 8 nucleotides long, with an amino-modification at the 5' terminus and a fluorescent 6-FAM label (see Chapter 2) at the 3' terminus. Final concentrations of DNA and EDC were 6 µM and 130 mM, respectively. The MES buffer had a concentration of 25 mM and a pH of 6. Samples were incubated in the fridge (± 4 °C) for a minimum of 4 h.

After binding, the samples were rinsed several times (4-6) in 2 x SSC + 0.5 % SDS at 60 °C to remove unbound DNA, followed by 3 rinsing steps in Milli-Q water at 60 °C to remove salt ions from the washing fluid. Samples were again dried in the oven at 60 °C before resistance measurements were performed. After the resistance measurements, the samples were put in PBS buffer to characterize them with the confocal fluorescence microscope.

5.4 Functionalization results

Confocal fluorescence microscopy (CFM) was used to investigate the results of the functionalization procedures. Therefore, fluorescently labeled DNA strands were used. Functionalized samples, called positive samples, were compared to EDC-negative reference samples. Furthermore, nanostructured samples are compared to bulk microstructure samples.

Fatty acid route

The results for the fatty acid route are given in Figure 5-4. From this figure it is clear that the nanostructured samples are highly functionalized. The carbon material exhibits a high fluorescence with a mean pixel intensity 249 a.u.. Furthermore, bleaching tests confirmed that the signal is actual fluorescence instead of reflection or background signal. This is also proven by the EDC-negative reference sample where there is no fluorescence signal coming from the carbon. The bulk microstructures, without nanostructured surface, show only little fluorescence signal. Although a bit difficult to see, there is some fluorescence signal present because a faintly visible bleach bar can be observed (inside the red box in the figure). If compared to the bulk EDC-negative reference sample, one can see that the functionalized carbon material shows slightly more fluorescence. It should be noted that the substrate surface is visible as background signal in the images of the bulk samples and the EDC-negative samples. Because no fluorescence signal could be detected at other focus heights, it was chosen to focus on the substrate surface. Images from the functionalized nanostructured samples are taken at an elevated focus height, at the top of the carbon structure.

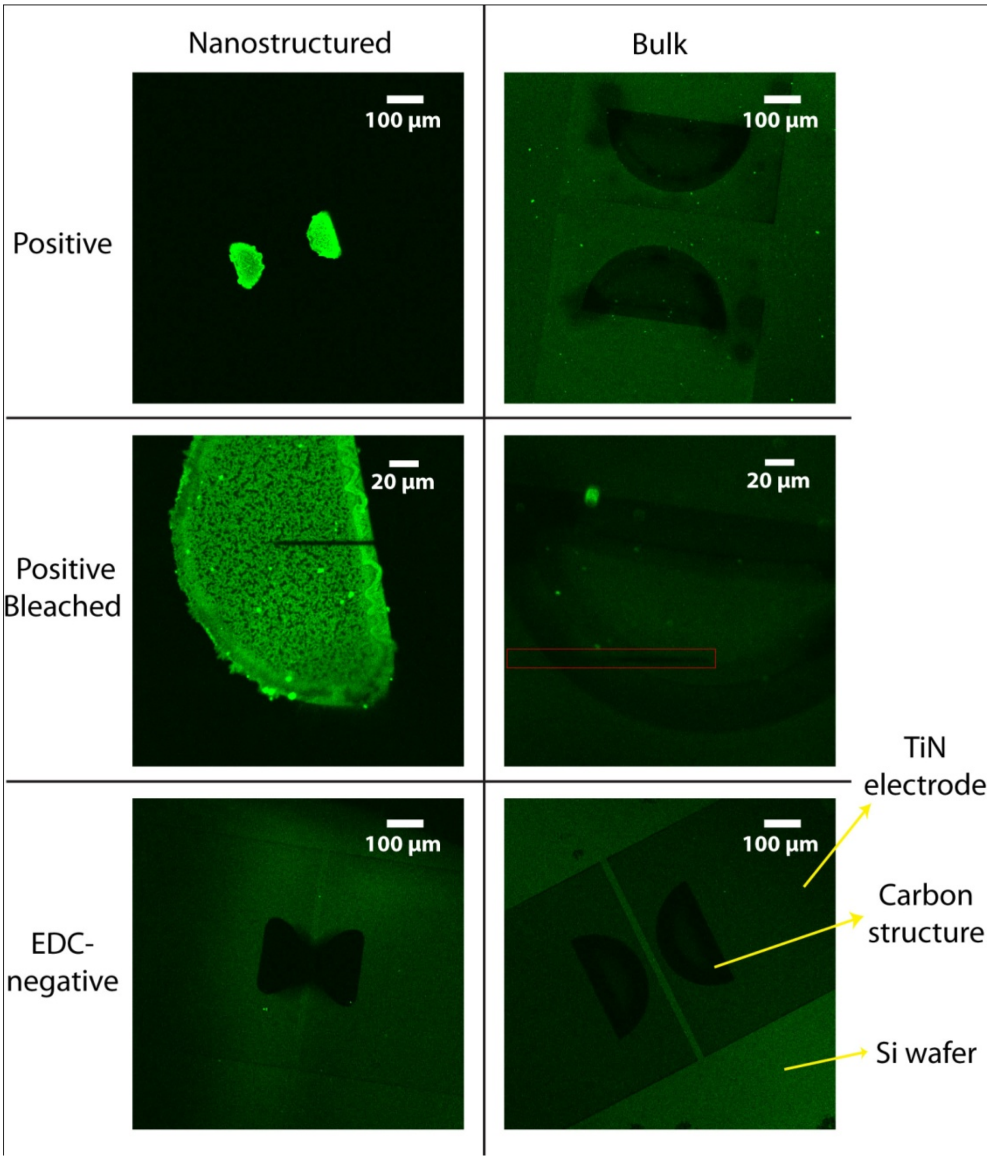

Figure 5-4. CFM images of functionalized carbon microstructures. Left side shows micro-nano hybrids while the right side shows bulk structures without the nanostructured outer layer. Top and middle row images are positive samples with bonded DNA. Bottom row images are EDC-negative reference samples. The middle row shows higher magnification images with an area where the fluorescent labels were bleached.

In order to rule out surface chemistry effects as the source of the difference between the nanostructured and bulk samples, both types of samples were treated with an H_2 plasma before functionalizaton. This plasma treatment should result in surfaces with the same chemical functionalities (C-H bonds), if this should not have already been so. Figure 5-5 presents the results of functionalization after this plasma treatment. The nanostructured sample (shown in A) still exhibits a fluorescence intensity that is much higher than in the bulk sample (shown in B). These results indicate that the greatly increased functionalization of nanostructured samples, compared to bulk samples, is a result of the huge increase in surface area of the nanostructured samples.

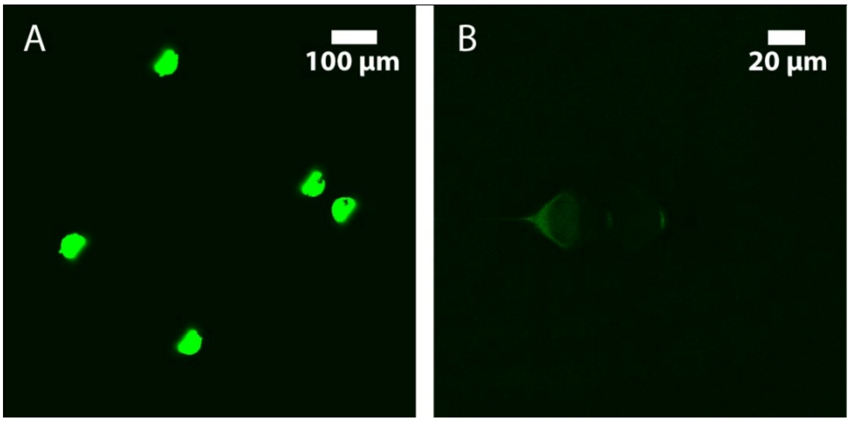

Figure 5-5. CFM images of H_2-plasma treated amorphous carbon samples functionalized with fluorescently labeled DNA. (A) Nanostructured sample, (B) bulk sample.

Diazonium route

The samples were also successfully functionalized with the diazonium route, see Figure 5-6. The positive sample shows a distinct fluorescence signal coming from the functionalized carbon. This fluorescence signal can be bleached clearly as shown in Figure 5-6 (B). The EDC-negative reference sample on the other hand exhibits no fluorescence signal at all. The carbon structures are shown as black dots against a green background, resulting from reflected laser light. This background signal could not be bleached.

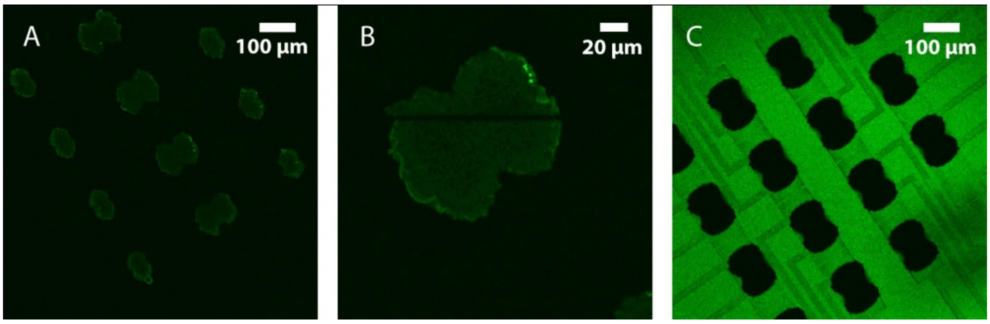

Figure 5-6. CFM images of nanostructured samples functionalized with DNA via the diazonium route. (A) Positive sample, (B) higher magnification of positive sample with bleached bar and (C) EDC-negative reference sample showing the carbon structures as dark spots on a reflecting substrate.

A comparison of the two routes indicates a higher functionalization degree for the fatty acid route than the diazonium route. Samples originating from the same wafer were functionalized via the fatty acid and the diazonium route. The EDC-mediated step was similar for both types and CFM measurements on both types were performed in one run. The results, presented in Figure 5-7, show that the fatty acid route is much more effective than the diazonium route. Image J software was used to quantify the pixel intensity of a selected region on the carbon structures. The mean pixel intensity was calculated and illustrated on the right of the figure. Mean pixel intensities for the diazonium and the fatty acid route are 36 a.u. and 249 a.u.,respectively.

The rather large difference in functionalization yield between the two routes could be due to the fact that the fatty acid route is an optimized route using commercial products whereas the diazonium coupling is a novel functionalization route about which little was known yet. Furthermore, the diazonium powder was homemade and its production still needs optimization to increase efficiency.

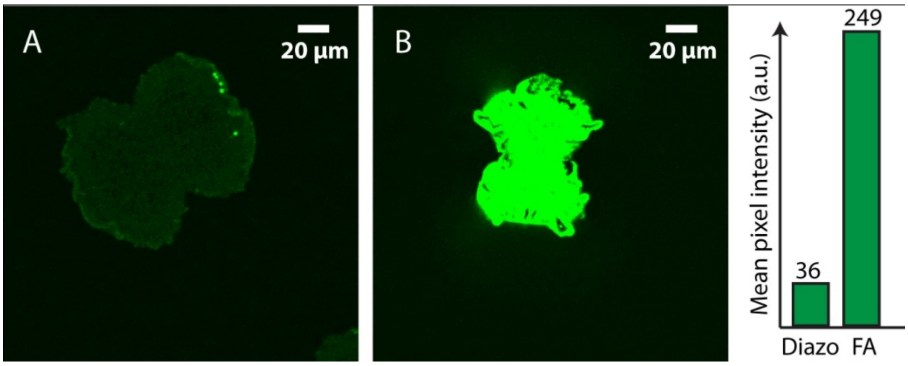

Figure 5-7. Comparison of the fatty acid route and the diazonium route. CFM images of samples functionalized via the diazonium route (A) and the fatty acid route (B). The mean pixel intensity for both routes is given on the right.

5.5 Resistance measurements on bridge structures

5.5.1 Measurement method

First steps were taken to investigate the potential of the amorphous carbon microstructures as DNA sensors. The bridge resistance was measured on the pristine microstructures, after attachment of the linker molecule and after attachment of single stranded DNA. Furthermore, nanostructured bridges were compared to bridges made of bulk amorphous carbon.

The resistance was measured over bridge structures spanning two in-plane electrodes. The bridge is formed by two amorphous carbon pillars that touch each other at the upper half, like the structures shown in Figure 5-3 A and B. It was found that the collapsed-like structures were more rigid than the arch-like structures. For this reason, the collapsed-like structures were preferred and results shown here are measured on this type of bridge.

Resistance measurements were performed in a four probe setup with a PA 200 probe system from SUSS MicroTec (Sacka, Germany). A current of 0.5 – 1 mA was applied over two probes and the resulting voltage was measured over the other two probes. So both ends of the bridges had two electrical connections.

The resistance was calculated according to Ohm's law. A scheme of the measurement setup is given in Figure 5-8. A Keithley 2400 SourceMeter, in 4-wire setting, was used to apply the current and measure the voltage. Measurements were performed under ambient conditions.

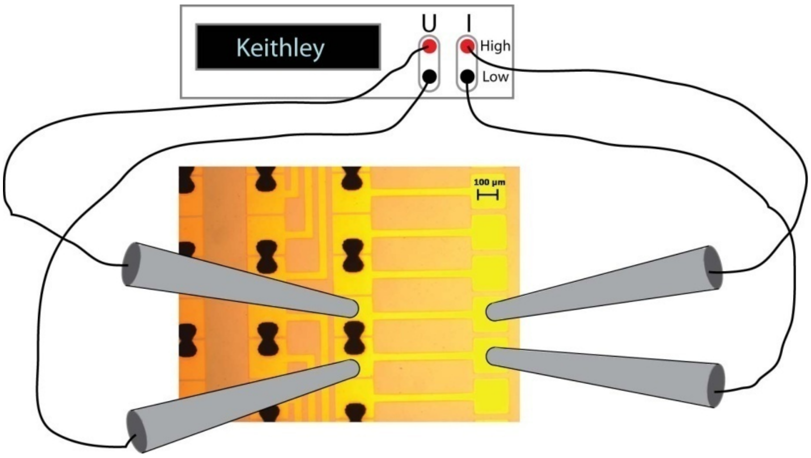

Figure 5-8. Illustration of the resistance measurement setup.

5.5.2 Results on resistance measurements

The I-V characteristics of the carbon microstructures were investigated first to assure good contact quality. The I-V curve shows linear behavior, confirming a good quality Ohmic contact. The I-V curve is plotted in Figure 5-9.

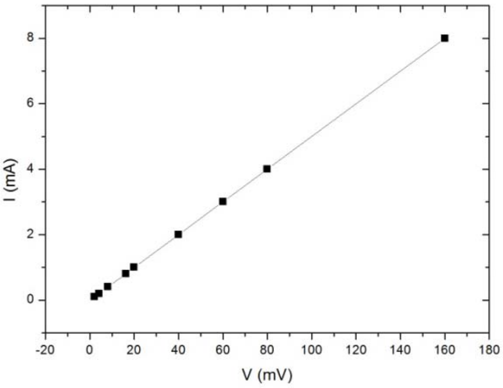

Figure 5-9. I-V curve of typical amorphous carbon bridge structure with a 20 Ω resistance.

The measured resistance values for two fatty acid route samples, with each a mini-array of bridge structures, are presented in Figure 5-10. One sample contained nanostructured carbon bridges and the other contained bulk carbon bridges. The overall shape of the two carbon types was very similar. After fatty acid attachment, each sample was broken in two pieces in order to prepare a positive sample and an EDC-negative reference sample for both sample types (nanostructured and bulk). The EDC-negative reference samples are denoted as reference in the figure.

Figure 5-10 (A) shows that the resistance increases after functionalization. The resistance of the nanostructured reference sample increases significantly more than the nanostructured positive sample. The resistance increase for both bulk samples lies somewhere in between the increase of the nanostructured samples. A possible explanation for the resistance increase is a damaging effect of the handling and reaction procedures. Especially the carbon-electrode attachment is prone to damage as it was observed that some carbon structures detached from the electrode surface.

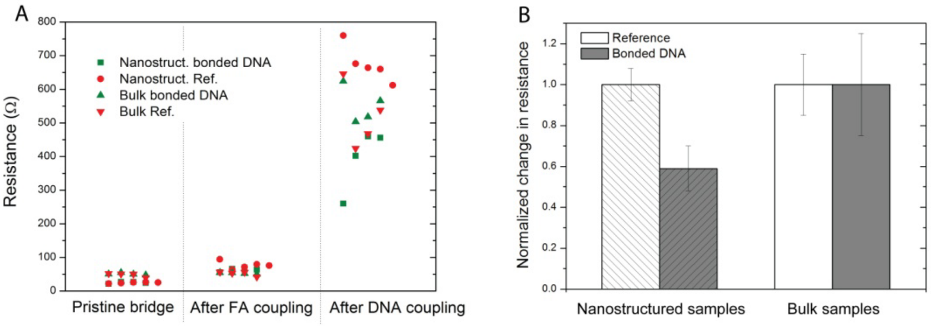

Figure 5-10. (A) Measured resistance values for the pristine bridge structures, bridges with fatty acid and bridges with DNA. Nanostructured bridges and bulk bridges were measured, both for a positive and an EDC-negative sample. (B) Graph showing the normalized change in resistance from pristine to DNA functionalized bridges. The resistance change of the reference samples was set to 1. Error bars indicate standard deviation (n=5 for the nanostructured Ref and n=4 for all other).

The change in resistance for each sample was determined in terms of percentage according to the following formula:

$$\Delta R = \frac{R_{DNA} - R_{pristine}}{R_{pristine}} \tag{5.1}$$

The average of the resistance change was determined for each sample type and the values were normalized by setting the resistance change of the reference samples to 1. These normalized resistance changes are shown in Figure 5-10 (B). For the nanostructured samples, one can see that DNA binding results in a 40 % lower change in resistance compared to the reference sample. For the bulk samples there is no difference between the positive and reference sample.

These results are in agreement with the fluorescence images which showed that bulk samples contained only very little DNA. It appears that DNA binding counteracts the resistance-increasing damage effects. Some possible explanations for this resistance-lowering effect could be the shortcutting of the amorphous carbon nanowires by conducting DNA strands and/or charge transfer effects. Binding of DNA molecules, which are negatively charged, may also induce the injection of holes or electrons into the amorphous carbon structure.

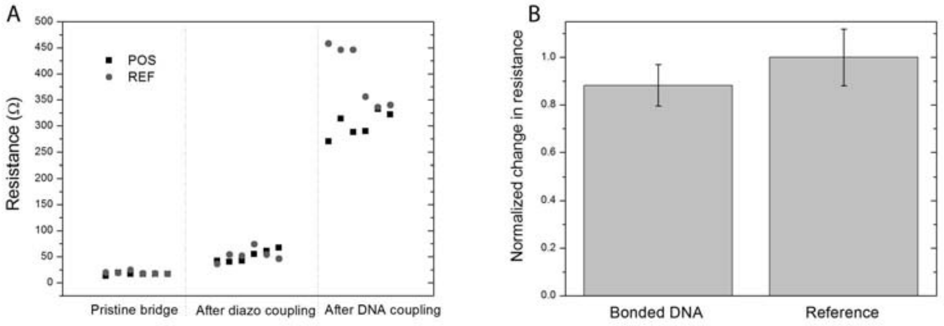

Figure 5-11. (A) Measured resistance values for the pristine bridge structures, bridges with diazonium and bridges with DNA. Nanostructured bridges were measured for a positive and an EDC-negative sample. (B) Graph showing the normalized change in resistance from pristine to DNA functionalized bridges. The resistance change of the reference samples was set to 1. Error bars indicate the standard deviation (n=6).

The resistance values and their changes after functionalization were also measured on the samples functionalized by the diazonium route. For this route, only nanostructured samples were functionalized and measured. Again, a positive sample is compared to an EDC-negative reference. The results are given in Figure 5-11.

Nanostructured samples functionalized via the diazonium route show the same trend as the fatty acid samples but the effect is less pronounced. The resistance also increases after functionalization, albeit not as much as for the fatty acid samples. The positive sample shows a lower increase in resistance compared to the EDC-negative reference, similar to the fatty acid route. However, the difference between positive and reference sample is only about 12 % compared to the 40 % for the fatty acid route. Looking at the standard deviations of the normalized changes, the 12 % difference is not enough to exceed the error bars and trust this "sensor" result. The smaller effect is consistent with the lower functionalization degree of the diazonium route as compared to the fatty acid route. The effect could possibly be increased by optimizing the diazonium functionalization.

5.6 Conclusions

Amorphous carbon microstructures were made with architectural and nanostructural tunability. These structures were functionalized with single stranded DNA via two different linking routes. The fatty acid route resulted in very high amounts of DNA bonded to the nanostructured surface of micro-nano hybrid structures. Bulk microstructures on the other hand, could only bind low amounts of DNA. The difference in DNA binding capacity can be explained by the huge difference in surface area between bulk and nanostructured samples. The second functionalization route, through diazonium coupling, was also successful in the biofunctionalization of nanostructured surfaces. Although the latter method turned out to be less effective, further optimization of this method may improve its efficiency. This method was only introduced in the last months of this thesis.

The potential of these amorphous microstructures as biosensors was investigated by measuring the resistance change after the DNA binding event. Although the resistance increased for all samples, it was found that the micro-nano hybrid structures show great potential as DNA sensors since a 40 % difference in resistance change was observed between samples with DNA and samples without DNA. Samples functionalized via the diazonium route only showed a 12 % difference and bulk samples did not show any difference between positive and reference samples. These results indicate that the nanostructured samples are very well suited for functionalization purposes due to their high surface area. They show a good potential as microstructured biosensors but their mechanical stability has to be improved to give univocal sensing responses. Furthermore, future work should investigate DNA hybridization and denaturation sensing with complementary or mismatched target DNA.

Chapter 6

Electronic characterization of ultrathin graphite flakes

Carbon-based materials with sp^2 bonding such as graphene, carbon nanowalls, and carbon nanotubes receive since years considerable scientific interest due to their extraordinary electronic transport properties. The unique features of graphene include the fact that the charge carriers behave like massless Dirac Fermions and the conductivity is not vanishing in the limit of vanishing carrier density [44], the sign of the carriers can be inverted by electric field effects [1], and the quantum Hall effect is observed [54]. Especially interesting with respect to sensor applications are the tunability of the carrier type and concentration as well as the ballistic charge transport with mean free path lengths of several micron. In combination with the extreme surface-to-volume ratio, the electronic band structure and transport properties respond with high sensitivity to various adsorbates (physisorbed gas molecules) as shown in recent work [232,233]. The mechanism is based on charge transfer between the adsorbates and the graphene sheets and is expected to fade out in graphite samples with ten or more stacked graphene layers.

In this chapter, we focus on the electronic properties of graphene stacks (i.e. ultrathin graphite layers) for sensing applications. First, the magnetoresistance effect is investigated. Results described in literature indicate a resistance increase by about 15 % at 270 K in a field of just 1 Tesla and the effect becomes even much more pronounced when increasing the magnetic field and lowering the temperature [234]. The positive magnetoresistance in pure metals is typically below 5 % in fields of 10 Tesla at liquid-helium temperature and this has no technological relevance for field-sensing applications or the readout of magnetically stored data. Instead, magnetic readheads are nowadays based on the giant negative magnetoresistance (GMR) achieved with metallic magnetic/non-magnetic multilayers [235,236]. The colossal negative magnetoresistance effect (CMR) in mixed-valency manganese perovskites offers even more substantial resistivity changes (orders of magnitude), but the effect requires fields much higher than those of technical relevance [237,238]. Also, materials with a strongly pronounced positive magnetoresistance 'PMR' such as Cr/Ag/Cr trilayers [239] and synthetic, boron-doped nano-crystalline diamond [240] show their giant PMR only in fields of several Tesla and at temperatures below 100 K. Therefore, graphite as a non-engineered, natural, and inexpensive material deserves a closer consideration for field-sensing purposes. Due to a wide variability of the material parameters documented in literature (presumably related to impurities and structural defects), we include also Hall-effect measurements in this study to obtain reliable information on the density and mobility of the charge carriers.

6.1 Sample preparation

6.1.1 Flake deposition

Ultrathin graphite flakes were produced by mechanical exfoliation of highly oriented pyrolytic graphite (HOPG) according to the method described by Geim and Novoselov [14]. HOPG crystals, grade SPI-2, from SPI Supplies (West Chester, USA) were used together with VD 8 ELEP Holder dicing tape from Nitto Denko (Osaka, Japan). Ultrathin graphite flakes were transferred to a Si substrate with a 300 nm thick, insulating oxide layer (WaferNet Inc. San Jose, USA). These flakes stick rather tightly to the surface due to van der Waals forces [1]. Next, Au alignment markers were deposited on the Si substrate with standard photolithography, followed by thermal evaporation of gold, and lift off. The alignment markers serve to identify the position of flakes on the substrate. Suitable flakes with a rectangular shape and typical lateral dimensions of 5 µm were selected by optical microscopy.

6.1.2 Electrical contact preparation

Before further processing, the samples were annealed in high vacuum of 10^{-7} hPa at 150 °C during 2 hours to remove adsorbates and tape residues. The actual electrical contact lines and contact pads for wirebonding were written with e-beam lithography. Therefore, a double layer of e-beam resist was spincoated on top of the sample. The resist concentrations and spinning parameters, see Table 6-1, were chosen to yield bottom- and top-resist layers with approximate thicknesses of 300 nm and 100 nm, respectively. The bottom layer consisted of MMA(8.5)MAA and the top layer of PMMA (MicroChem, Newton, USA).

	Bottom layer	**Top layer**
Resist	MMA(8.5)MAA	950 PMMA
Concentration	8.6 % in ethyllactate	2 % in chlorobenzene
Spincoat speed	4000 rpm	4000 rpm
Spincoat time	45 s	45 s
Bake temp/time	150°C / 90 s	180 °C / 90 s

Table 6-1. E-beam resist parameters

The contact pattern with four leads in van der Pauw geometry was designed on basis of earlier taken SEM images of the flake. Subsequently, the pattern was written and positioned using the alignment markers. An electron current dose of 270 μC/cm^2 was used for writing. In order to develop the exposed resist, MIBK developer (MicroChem, Newton) was used in a 1:3 dilution with isopropyl alcohol for 120 s. Titanium / aluminum contacts were prepared by sputtering a 5 nm thin layer of Ti followed by thermal evaporation of 70 nm of Al. Finally, a lift-off step was performed in boiling acetone to remove superfluous metal and e-beam resist. A schematic of the metal deposition process is given in Figure 6-1.

To minimize mechanical strain at the metal-graphite contacts and to remove adsorbates from the resists and developers, a second thermal annealing was done with the same parameters as specified above. Relying on current-voltage characteristics we have verified that these contacts have ohmic behavior. A graphite sample, prepared and contacted with the described procedures, is shown in Figure 6-1.

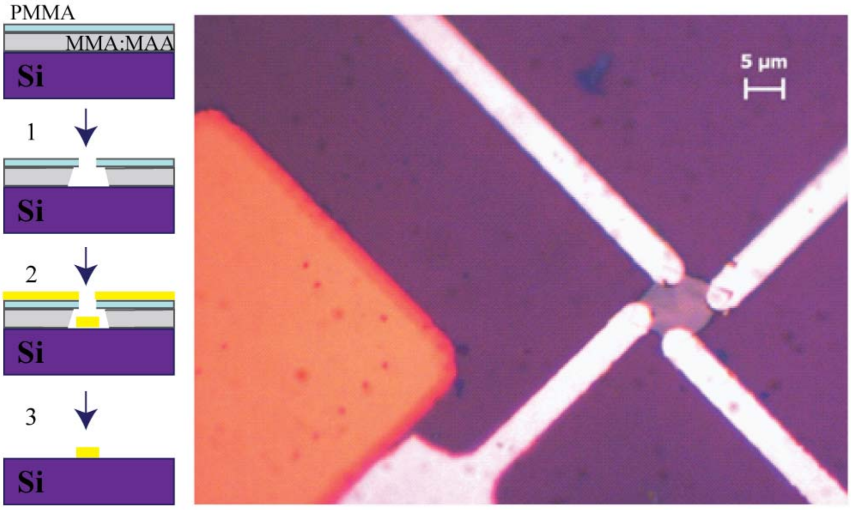

Figure 6-1. Left: Schematic of electrical contact deposition. (1) Writing the pattern in the e-beam resist and developing. (2) Metal deposition. (3) Lift off. Right: Microscopy image of a flake with four metal contacts (white structures). The orange structure on the left is an alignment marker.

6.2 Cryostat setup

The electronic transport properties were studied for two specific samples using the van der Pauw method [15]: Sample # G1 had lateral dimensions of 9.5 by 5 μm^2 with a thickness of 50 nm, corresponding to a stack of 150 graphene layers. From the viewpoint of the electronic band structure this sample should therefore reflect the properties of graphite rather than the features of graphene [4,5]. Unless stated otherwise, all data discussed within this chapter refer to # G1. For comparison, a second sample, # G2, was analyzed with lateral dimensions of 8.5 by 9 μm^2 and a thickness of 25 nm, corresponding to 75 graphene layers. The sample thicknesses were determined by atomic force microscopy after performing the transport measurements. The contacted samples were fixed on a holder on the cold finger of a flow cryostat (MicroStat, Oxford Instruments, UK) with a maximum temperature range from 4.2 K to 400 K. Electrical connections were obtained by wirebonds between the sample and the holder, and with triaxial cables between the cryostat and all external devices. The current source, Keithley 6221, was operated at a level of 50 µA while voltages were measured with a Keithley 2400 source meter. To allow for interchanging the current- and the voltage probes according to the van der Pauw method, we employed a grounded and shielded, manually operated switchbox, taking care that the current source was set to zero during the switching steps.

Magnetic fields, oriented parallel to the c-axis of the graphite samples, were generated with an electromagnet, type Bruker B-E 15 v. The relationship between the coil current and the resulting field at the sample position was calibrated with a Hall sensor, LakeShore HGT-2010, revealing field strengths up to a maximum of 2.07 Tesla. In the geometry with B parallel to the c-axis of the graphite flakes, we measured resistivities (transverse magnetoresistance) and Hall voltages for temperatures between 77 K and 300 K (# G1), and between 4.2 K and 400 K (# G2). Furthermore, magnetotransport studies were performed with several angles θ between the B field and the c-axis to evaluate whether there is also a noticeable longitudinal contribution to the magnetoresistance.

6.3 Results

6.3.1 Colossal positive magnetoresistance

As shown in Figure 6-2, the in-plane room temperature resistivity of the graphite flake is 40 µΩcm. This is by a factor of 20 smaller than literature values for bulk samples of graphite. Therefore, the resistivity of these small-volume samples appears to be intrinsic and not dominated by grain-boundary contributions. Although the temperature dependence of the zero-field resistivity (insert of Figure 6-2) is apparently thermally activated, it cannot be easily described by an Arrhenius law or hopping models in two or three dimensions.

Refinements, taking into account temperature-dependent pre-factors, do also not allow bringing the experimental data in agreement with theoretical models. However, an empirical expression, which will further be addressed in the section about the Hall effect, is in very good agreement with the data:

$$\rho(T) = \frac{\rho(T \to 0)}{1 + \alpha \cdot T} \tag{6.1}$$

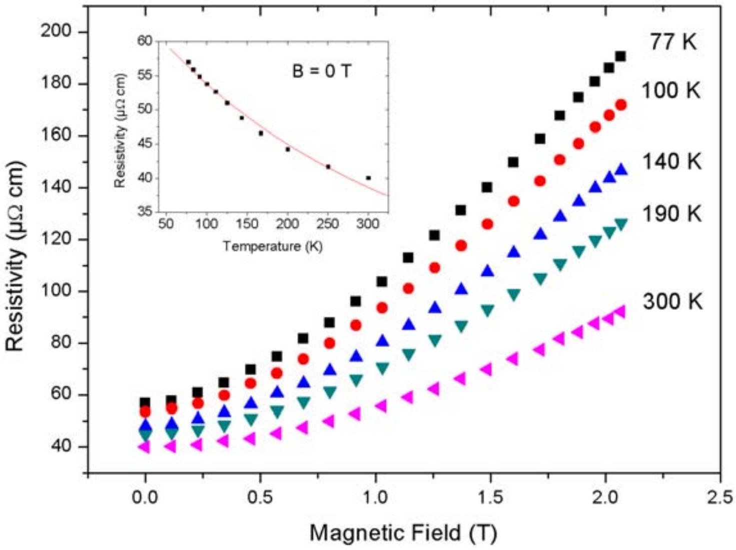

Figure 6-2. Magnetoresistance behavior of sample # G1 at selected temperatures between 77 K and 300 K. The magnetic field is oriented parallel to the c axis. The zero field resistivity is given in the insert with the solid line corresponding to the fit function described in the text.

For the fit parameters, we obtain the numerical values ρ (T→0) = 66.8 μΩcm and $\alpha = 2.42 \cdot 10^{-3}$ K^{-1} with $R^2 = 0.98$ (R^2 is the coefficient of determination). Applying the same function to sample # G2 gave ρ (T→0) = 93.1 μΩcm and $\alpha = 1.98 \cdot 10^{-3}$ K^{-1} with $R^2 = 0.91$. The magnetoresistance behavior of sample # G2 is plotted in Figure 6-3 along with the temperature dependence of its zero field resistivity, insert of Figure 6-3.

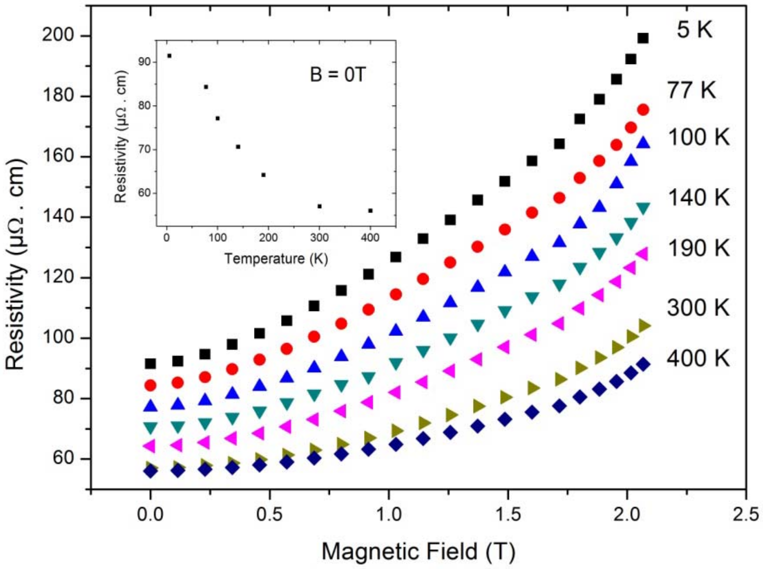

Figure 6-3. Magnetoresistance behavior of sample # G2 at selected temperatures between 5 K and 400 K. The zero field resistivity is given in the insert.

The positive magnetoresistance (PMR) becomes very pronounced already at room temperature and in moderate fields. For a quantitative description we define a PMR ratio as follows:

$$PMR = \frac{\Delta\rho}{\rho_0} = \frac{\rho(B) - \rho(B=0)}{\rho(B=0)} \tag{6.2}$$

In a field of 2 Tesla, the PMR of sample # G1 exceeds 100 % at 300 K and 200 % at 77 K and the magnitude of the effect as such is in good agreement with the work by Barzola-Quiquia et al. [234]. A comparison of the most important magnetoresistance data for samples # G1 and G2 is given in Table 6-2. Note that in comparison to pure metals, the PMR is substantial and easily measurable, it occurs already at room temperature, and the magnetic-field scale is moderate albeit not yet sufficiently low for applications related to the readout of magnetically stored data.

Sample	**G1**	**G2**
Thickness (nm)	50	25
ρ_0 (300 K) Ωm	4.01×10^{-7}	5.70×10^{-7}
PMR (300 K, 2.06 T) %	130	83
ρ_0 (77 K) Ωm	5.67×10^{-7}	8.43×10^{-7}
PMR (77 K, 2.06 T) %	235	108

Table 6-2. Summary of most important magnetoresistance results for sample # G1 and G2

Next, we analyzed the field dependence of the PMR magnitude for the different temperatures under study. Metallic-like conductors fulfill the classical Kohler rule [241], stating that the relative resistivity increase is a universal function of the ratio between the magnetic field B and the zero-field resistivity, equation (6.3). This originates from the fact that, under the influence of a magnetic field, the charge carriers will move on fragments of Landau circles rather than along straight lines. In turn, this reduces their effective mean free path.

In non-magnetic, clean metals and small magnetic fields, the function f is strictly quadratic in B, resulting in a more specific representation of Kohler's rule (equation (6.4)):

$$\frac{\Delta\rho}{\rho_0} \propto f\left(\frac{B}{\rho_0}\right) \tag{6.3}$$

$$\Delta\rho \cdot \rho_0 \propto B^2 \tag{6.4}$$

A scaling in the sense of equation (6.4) should collapse all ρ(B,T) data on one single curve. Representing the data given in Figure 6-2 according to equation (6.4) results in the magnetoresistance traces shown in Figure 6-4: Noteworthy, this scaling deviates from $\Delta\rho \propto B^2$, which holds in nonmagnetic, metallic conductors, and follows rather a power law relationship $\Delta\rho \propto B^{\beta}$ with a weakly temperature dependent exponent β, ranging from 1.51 (77 K) to 1.72 (300 K).

The reliability coefficients for all these temperatures are above $R^2 = 0.99$. Also, there is a systematic displacement along the $\Delta\rho\cdot\rho_0$ axis, which can be understood if the density of the charge carriers itself is temperature dependent. This aspect will be further addressed in the section below that deals with the Hall-effect measurements. Certain deviations from Kohler's rule have actually been reported for many metal-like materials, including layered organic metals [242] and cuprate superconductors in their normal state [243].

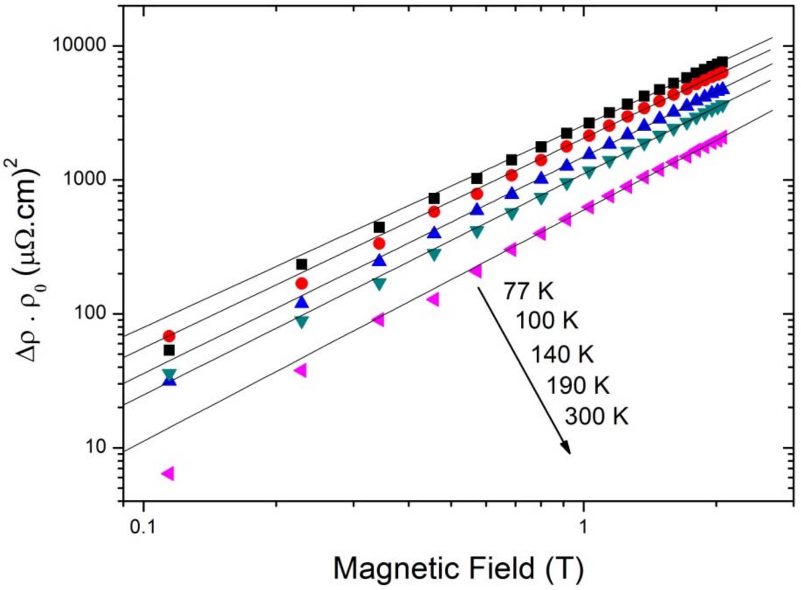

Figure 6-4. Magnetoresistance behavior of sample # G1 plotted according to Kohler's rule for metals. There is a systematic, temperature-dependent displacement along the Y-axis and the fitted slopes (ranging from 1.5 to 1.7) are smaller than the expected B^2 dependence.

The fact that $\beta < 2$ may possibly be interpreted in terms of the presence of correlated magnetic impurities or other local magnetic moments. At least in the ferromagnetic CMR materials, the magnetoresistance is known to be linear in the magnetic field ($\beta = 1$) as long as the magnetization is below the saturation limit [238]. In our case, the impurity concentration of the HOPG samples is below 10 ppm, according to the supplier, which sets a maximum on the concentration of (magnetic) atoms or ions. A careful analysis by x-ray photoemission spectroscopy gave a negative result with respect to the presence of iron or other magnetic impurities. Although the concentration of 10 ppm is low in absolute terms, the average distance between these dopants or impurities would correspond to 200 nm, meaning that scattering centers cannot be ignored. Irrespective of whether there are magnetic ions in the graphite lattice (e.g. in an intercalated way) ferromagnetic moments have also been reported in nominally iron-free HOPG samples and were attributed to topological defects or electron-electron correlations [244]. The recently discovered ferromagnetism of hydrogen vacancies in graphane, see ref. [245], should be negligible in our samples due to the almost bulk character of the graphite flakes as compared to few-layer graphene. SQUID (Superconducting Quantum Interference Device) measurements, performed at K.U.Leuven (Belgium), have shown that the HOPG crystals do contain magnetic moments, albeit in very low concentrations. After correction for diamagnetic background, the magnetization curves, presented in Figure 6-5, show a small hysteresis, hinting to the presence of ferromagnetic moments.

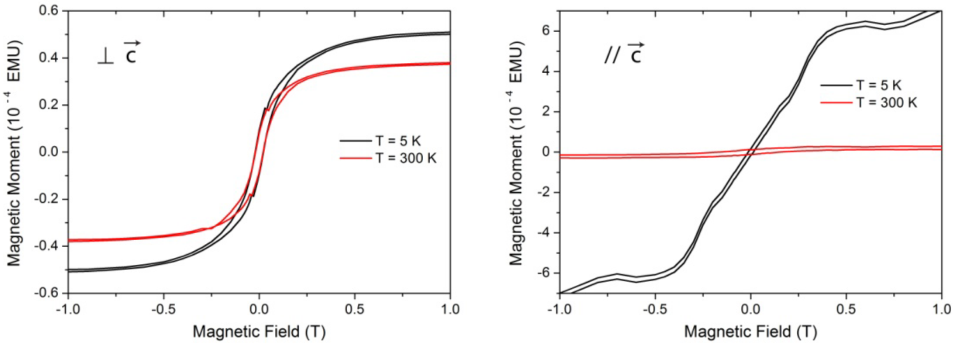

Figure 6-5. SQUID measurements on HOPG sample. Magnetization was measured parallel (left) and perpendicular (right) to the graphite sheets. Data were corrected for diamagnetism.

In order to check whether there is also a longitudinal magnetoresistive effect (field oriented in plane with the graphene sheets), we studied the magnetoresistance for several angles θ between the field direction and the c-axis of the graphite flakes. These measurements, illustrated in Figure 6-6, were performed at 300 K in the maximum available field of 2.07 Tesla. There is no measurable effect of the in-plane components of the magnetic field and the PMR is maximal when B is parallel to the c-axis of the flakes. This behavior is similar to other quasi two-dimensional materials such as the high-temperature superconductors [246]. The relevant field component is the component parallel to the c-axis of the graphene sheets, which can be expressed by the following scaling relation between the PMR amplitude and the angle θ:

$$\rho(B,\theta) = \rho(B=0) + \Delta\rho(B)\cdot\cos^{\beta}\theta \qquad (6.5)$$

Note that the curves presented in Figure 6-6 have no free fitting parameters, the only input data are ρ (2.07 T, θ = 90°) ≈ ρ (0 T) = 40.2 μΩcm and ρ (2.07 T, θ = 0°) = 83.6 μΩcm. The dashed line, obtained with β = 2 (non-magnetic materials) is already in good agreement with the data. An improved correspondence is obtained with β = 1.7, consistent with the results in Figure 6-4.

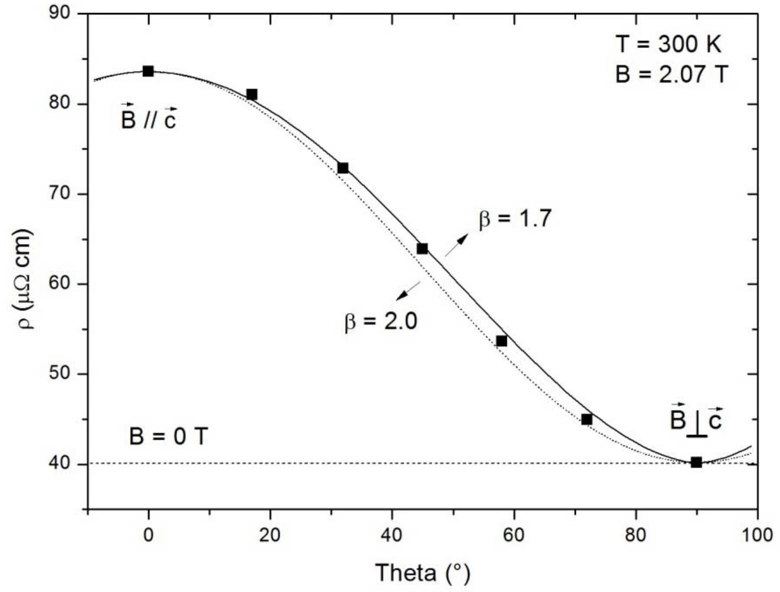

Figure 6-6. Magnetoresistance behavior of sample # G1 plotted at a fixed temperature and magnetic field for various angles between the field direction and the graphene sheets. The fit curves show that the perpendicular field component is responsible for the PMR effect.

6.3.2 Hall effect- and mobility study

Based on the van der Pauw measurements, we extracted also the temperature and field dependence of the Hall voltage, which is used as an input parameter for the determination of charge-carrier concentrations and mobilities. Since the van der Pauw scheme is more susceptible to potential geometrical and electronic errors than a Hall-bar configuration, we first verified the linearity of the Hall signal with respect to the magnetic field and the current at 300 K. As shown in Figure 6-7, both linearities are fulfilled, giving confidence in the reliability of the consecutively performed low-temperature measurements. From the sign of the Hall voltage U_H, we conclude that the dominant charge carriers are p-type.

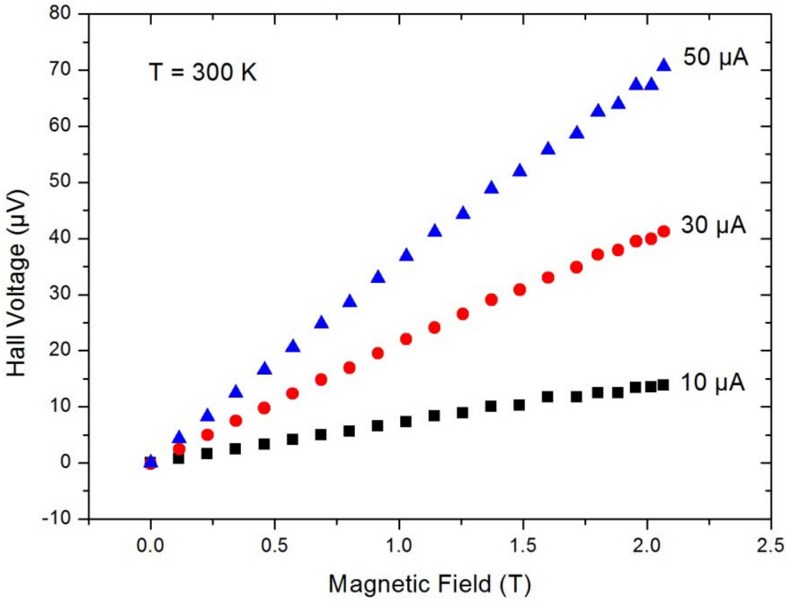

Figure 6-7. The Hall voltage at 300 K increases strictly linearly with the applied magnetic field and varies proportional to the measuring current.

The relationship between the Hall coefficient R_H, the Hall voltage U_H, the current I, and the sample thickness d and carrier concentration n is given by:

$$R_H = \frac{U_H \cdot d}{I \cdot B} = \frac{1}{n \cdot e} \tag{6.6}$$

Here, we assume a one-band model with p-type carriers only and e represents a positive elemental charge. For a field B = 2.0 T, the given sample thickness d = 50 nm, and the three different currents (10 μA, 30 μA, and 50 μA), we obtain R_H = 3.5 (± 0.2) · 10^{-8} m^3/C. This corresponds to a carrier density n = 1.7 (± 0.1) · 10^{26} holes per m^3. The concentration of carbon atoms in single-crystalline graphite is 1.13 · 10^{29} per m^3 and therefore we have an approximate ratio of 1 mobile charge carrier per 660 carbon atoms. According to the semi metallic behavior of graphite, a more refined analysis can be based on a two-band model with p- and n-type carriers [45]. However, this is less straightforward because it requires the mobility ratio between p- and n-type carriers as an additional, unknown parameter.

In the following, we studied the field dependence of the Hall voltage also for selected temperatures between 77 K and 300 K, see Figure 6-8. The current in these measurements was always set to 50 μA. Above 1 Tesla, there is a clear downward bend of the U_H (B) curves, which cannot be explained within the one-band model. Moreover, this is in contrast to earlier Hall studies on graphite by Kopelevich et al., where an upward bent of the Hall-voltage traces was observed and explained by a field-induced exciton-pairing mechanism [247]. A control experiment on sample # G2 has confirmed the downward bent: the initial slope of the U_H (B) traces at 300 K was also positive, but U_H even became zero around 1.5 T and turned out to have a negative sign for higher fields, see Figure 6-9.

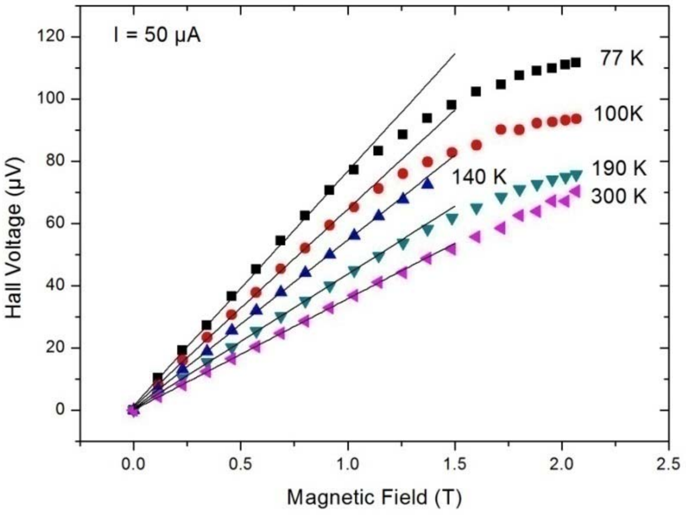

Figure 6-8. Hall voltage versus magnetic field of sample # G1 for selected temperatures between 77 K and 300 K. For fields above 1 T there is a deviation from linear behavior, suggesting the presence of anomalous contributions.

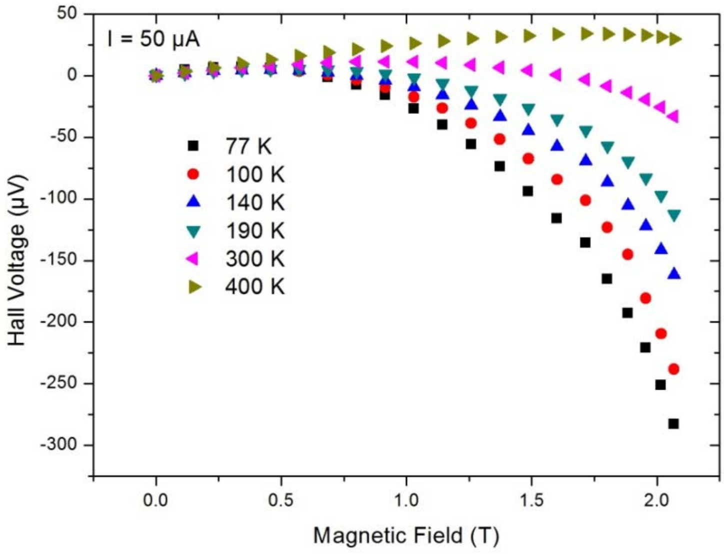

Figure 6-9. Hall voltage versus magnetic field of sample # G2 for selected temperatures between 77 K and 400 K. The Hall voltage is positive at lower fields but changes to negative values for higher fields. The magnetic field linked to this change is temperature dependent.

There are three possible explanations, but the given data set with its limited field- and temperature range does not yet allow to come to a clear conclusion: i) Signatures of the quantum-Hall effect are one possibility, but quantum oscillations in graphite and few-layer graphene have until now only been observed for temperatures below 50 K and 2 Tesla is an unusually low field scale [107,248,249]. ii) One may also infer a compensated Hall effect with a contribution by electron-type carriers: the nonlinear behavior could then indeed be caused by a field-dependent ratio between the hole- and electron mobilities. Compensation effects can therefore bring about apparent changes from hole- to electron type carriers [250]. iii) Finally, there is an anomalous Hall effect in magnetic metals and oxides with a superposition of the ordinary Hall effect and scattering mechanisms related to the magnetic moments of the samples, see e.g. [251] and references therein. As mentioned above, HOPG graphite is known to contain magnetic moments [244] which was also confirmed by the SQUID measurements. However, their concentration is by orders of magnitude lower than for example in iron or in manganese based perovskites. Therefore, also the validity of this explanation is unclear and further studies are required to pinpoint the precise origin of the non-linear U_H (B) behavior in higher magnetic fields.

To evaluate the temperature dependence of the charge-carrier density and mobility (of sample G1), we limit the data analysis to the low-field regime and calculated n based on the initial slopes of the U_H (B) traces presented in Figure 6-8. The carrier concentrations are given in Figure 6-10 and reveal a sublinear increase with temperature, in agreement with the half-metallic character of graphite. The existence of a bandgap cannot be excluded, but the characteristic energy scale, if any, cannot be extracted from these data. At most, we can conclude that the temperature dependence of n follows approximately a scaling proportional to the square root of temperature. From the zero-field resistivities ρ_0 and the carrier densities, we finally derived the carrier mobilities by using the formula:

$$\mu(B \to 0) = \frac{R_H(B \to 0)}{\rho_0} = \frac{e \cdot \tau}{m} \qquad (6.7)$$

The mobility values μ are also given in Figure 6-10 and μ should be independent of the absolute carrier concentrations. The carrier concentration and mobility for both samples are listed in Table 6-3. In a material such as graphite with a low absolute charge-carrier concentration, possible interactions between charge carriers can in good approximation be neglected.

Sample	**G1**	**G2**
Thickness (nm)	50	25
n (300 K) cm^{-3}	1.75×10^{20}	6.03×10^{20}
μ (300 K) cm^2/Vs	891	180
n (77 K) cm^{-3}	8.28×10^{19}	3.06×10^{20}
μ (77 K) cm^2/Vs	1329	239

Table 6-3. Comparison of carrier density and mobility in samples #G1 and G2

Since μ is related to the charge, effective mass m, and scattering time τ, one can derive a temperature dependence based on Matthiessen's rule for superimposed scattering mechanisms.

The scattering due to impurities and grain boundaries has a temperature independent value τ_0 and scattering due to phonons follows a scaling according to $\tau_1 \sim T^{-1}$. The effective scattering time follows the relationship $1/\tau = 1/\tau_0 + 1/\tau_1$. Using this relationship and equation (6.7), the mobility can be described as follows:

$$\mu = \frac{e}{m} \cdot \frac{\tau_1}{1 + \tau_1 / \tau_0} \qquad (6.8).$$

If we define the temperature dependence of τ_1 as $\tau_1 = A/T$, with A an unknown constant, equation (6.8) can be rewritten as:

$$\mu = \frac{e}{m} \cdot \frac{\frac{A}{T}}{1 + \frac{1}{\tau_0} \cdot \frac{A}{T}} \qquad (6.9).$$

Multiplication of equation (6.9) with τ_0 gives:

$$\mu(T) = \frac{e}{m} \tau_0 \cdot \frac{\frac{A}{T}}{\tau_0 + \frac{A}{T}} \qquad (6.10).$$

With $\mu(T \to 0) = {}^{e}\!/_{m} \cdot \tau_0$ and ${}^{\tau_0}\!/_{A} = \gamma$, the temperature dependence of the mobility should be given by the expression:

$$\mu(T) = \frac{\mu(T \to 0)}{1 + \gamma \cdot T} \qquad (6.11)$$

With the parameters $\mu(T \to 0) = 1566$ cm^2/Vs (± 96 cm^2/Vs) and $\gamma = 2.8 \cdot 10^{-3}$ K^{-1} (± $0.6 \cdot 10^{-3}$ K^{-1}) we obtain indeed a nice correspondence with the experimental data, as illustrated in Figure 6-10. The R^2 value of the calculated curve is 0.93. The absolute mobility values, at room temperature as well as in the low-temperature limit, are high when compared to metals and similar to electronic grade silicon. For comparison, in few-layer graphene sheets with a suitable gate voltage, values up to $6 \cdot 10^4$ cm^2/Vs have been reported at a temperature of 4 K [1]. The current record value is $2 \cdot 10^5$ cm^2/Vs at 5 K in gated single-layer graphene sheets, which were suspended to exclude any disturbing influence from an underlying material [47].

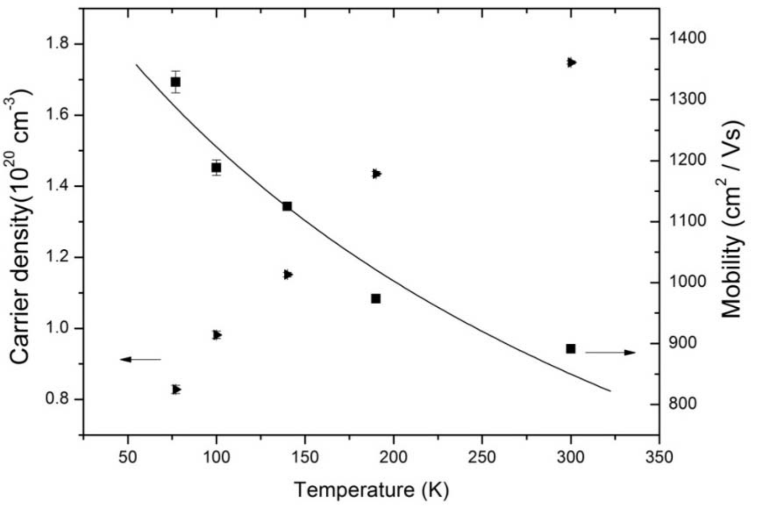

Figure 6-10. Temperature dependence of the charge-carrier density n (triangles, left scale) and the charge-carrier mobility μ (squares, right scale), derived in the limit of low magnetic fields B → 0. The solid line for the mobility scaling was calculated using equation (6.7).

Although the value $\mu(T \to 0) \approx 1566$ cm^2/Vs is reduced with respect to gated few- or single-layer graphene, the mean free path is in the order of 100 nm to 1 μm, which suggests a ballistic charge transport. Here, we have assumed that the carrier mass is in the order of the free-electron mass and that the carrier speed is in the range 10^5 – 10^6 m/s. The mean free path of 200 nm, estimated on the basis of the maximum impurity concentration in section 6.3.1, fits excellently within the margins obtained from the mobility analysis. The temperature dependence of the mobility, given by equation (6.11), suggests that the resistivity increases with increasing temperature. This is obviously not the case (see insert of Figure 6-2) because the temperature-induced rise of the charge-carrier density overcompensates the diminishing mobility. An improved description of the experimentally observed resistivity decrease with increasing temperature requires therefore mainly an in-depth understanding of the temperature dependence of the charge-carrier density.

As we have determined the charge carrier concentration, it is possible to plot Kohler's rule taking into account the temperature-dependent carrier concentration. First we will deduce the relation between magnetoresistance and carrier concentration. Magnetoresistance can be expressed as:

$$\frac{\Delta\rho}{\rho} = \frac{1}{24}\tau^2\omega_c^2 \tag{6.12}$$

with τ, the scattering time, and ω_c, the cyclotron frequency, given by

$$\tau = \frac{m}{ne^2\rho_0} \tag{6.13}$$

$$\omega_c = \frac{eB}{m} \tag{6.14}$$

If we plug equations (6.13) and (6.14) into equation (6.12), we get

$$\frac{\Delta\rho}{\rho_0} = \frac{1}{24}\frac{B^2}{e^2n^2\rho_0^2} \tag{6.15}$$

This means that the presentation of the Kohler rule in equation (6.4) can be rewritten as

$$\Delta\rho \cdot \rho_0 \cdot n^2 \propto B^2 \tag{6.16}$$

If we now plot the data from Figure 6-2 according to equation (6.16), we see that the magnetoresistance traces ρ(B,T) collapse to one single line as expected, see Figure 6-11.

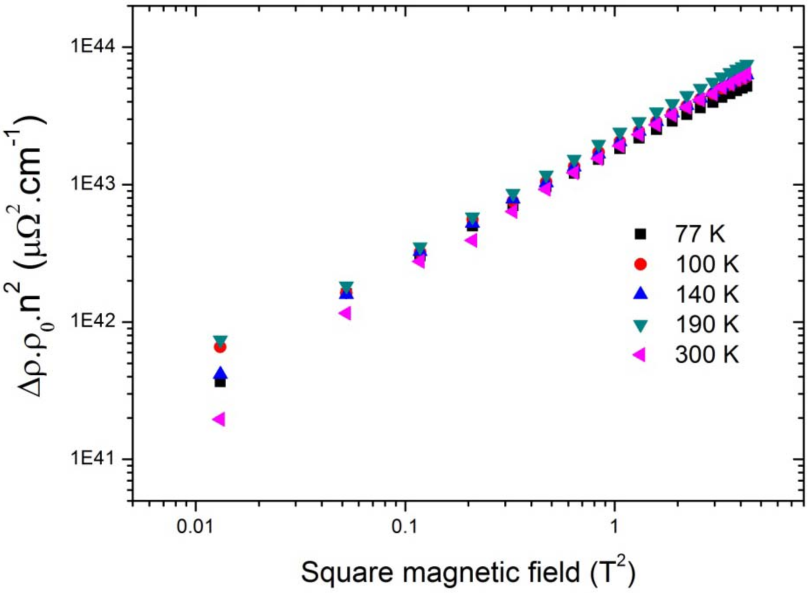

Figure 6-11. Magnetoresistance behavior from sample #G1 plotted according to Kohler's rule taking into account the temperature dependence of n. The temperature-dependent displacement of Figure 6-4 is canceled out.

6.4 Conclusion

We have analyzed the resistivity and Hall effect of ultrathin stacks of graphite and found that the resistivity increases markedly at fields below the 1 Tesla range. The resistance has a non-linear (close to quadratic, $\beta \approx 1.6 \pm 0.1$) response with respect to the applied field. In order to obtain linearized field-response characteristics, for example to develop magnetic-field sensors, it appears recommendable to induce intentionally ferromagnetic dopants or other ferromagnetic correlations associated with specific adsorbates or topological defects. The creation of carbon vacancies by irradiation with high-energetic ions is therefore a promising route to create magnetic moments with a controlled concentration [252,253].

We have found that the positive magnetoresistance (PMR) in ultrathin graphite flakes follows Kohler's rule with the side condition that the charge-carrier density is temperature dependent. The surprisingly strong PMR amplitude is related to the fact that the mean free path, in the order of 100 nm or more, is in the same range as the radius of Landau circles. The temperature dependence of the charge-carrier mobility can be understood in terms of scattering at impurities and thermal excitations. In order to determine the charge carrier density, we focused on the low-field limit, where there is a linear relationship between the applied field and the resulting Hall voltage. At higher field, the Hall effect shows anomalous features, which can possibly originate from compensation effects (superposition of hole- and electron carriers) or localized magnetic moments.

Chapter 7

Conclusion and outlook

In order to investigate the potential of graphene-based materials and amorphous carbon as DNA sensor platforms, functionalization experiments were carried out on different types of material. Each functionalization route tested here, aimed to bind DNA strands to a specific target. First steps were taken to investigate another aspect of DNA sensors namely the readout of a sensing event. Ultrathin graphite flakes were electronically characterized to improve the understanding and development of future sensors with electronic readout. Furthermore, a provisional DNA sensor, based on amorphous carbon structures, was developed.

All the functionalization routes that were tested here, made use of EDC coupling as it is an efficient and relatively easy way to covalently bind amino-modified DNA to the carboxylic acid group of specific linker molecules. However, each functionalization target requires a suited linker molecule and the key point of the functionalization work in this thesis was the attachment of specific linker molecules that allowed the EDC-mediated coupling.

CNW, consisting of vertically oriented stacks of 4-6 graphene sheets, show great potential as selective and reusable binding platforms for DNA. They were functionalized with DNA via a fatty acid linker molecule, which was photochemically attached. This method acted upon the hydrogen-terminated edges of the CNW as well as defect sites. Fluorescence microscopy proved that the functionalization was successful and that is was possible to differentiate, in hybridization experiments, between fully complementary and single mismatched target DNA. As it concerned one mismatch in a total of 29 nucleotides, one can conclude that the system shows a high selectivity. Reusability of the system was demonstrated by repeating 10 denaturation-rehybridization cycles.

Another aim was to functionalize the basal plane of graphene and thin graphite flakes with DNA strands. This allows to work with individual flakes and should increase the amount of bonded DNA per mass of graphene-based material. First, a non-covalent binding method was tested with the goal to functionalize graphene without losing its excellent conducting properties. For this purpose, pyrene-like linker molecules were allowed to interact with flake surfaces through π-π stacking. However, after the necessary washing steps, no clear evidence for the presence of the linker nor DNA could be found by fluorescence microscopy, fluorescence spectroscopy or XPS. Although literature exists where this method was successfully used on CNT and graphene, results obtained in this thesis indicate that this method is not suited for the non-covalent attachment of DNA to the basal plane of graphene and graphite. It is thought that the non-covalent coupling is not strong enough to withstand even mild washing steps. Non-covalent binding on graphene surfaces described in literature only served to improve the solubility of the graphene. The presence of the non-covalently attached species after rinsing was not detected nor required in experiments described in literature.

Since the non-covalent binding method failed, efforts were made to covalently functionalize the basal plane of graphene and graphite surfaces. For this purpose, diazonium salts were used as linker molecules. Functionalized samples were characterized with Raman spectroscopy, as this method allows the investigation of individual preselected flakes. Furthermore, this method is sensitive to changes in the graphene structure meaning that covalent coupling, accompanied by the conversion of sp^2 carbon into sp^3 carbon, can be detected as such. The Raman results indicated that at least a part of the diazonium linker was covalently bonded because a defect related D peak appeared in most functionalized samples. Another part was merely physisorbed, giving rise to a range Raman peaks that disappeared after thorough rinsing of the samples. Unfortunately, the presence of bonded DNA could not be unambiguously detected since there was no real difference in Raman spectra of positive and EDC-negative reference samples. However, based upon functionalization experiments with diazonium and DNA on diamond and amorphous carbon samples, it is believed that DNA is present, possibly in very low amounts, but stays undetected by the Raman spectroscopy. It can be concluded that the diazonium route works on graphene surfaces but its efficiency still needs improvement and it is also highly desirable to prove the presence of bonded

DNA strands on the graphene surface. A suggestion for the future would be to use DNA strands modified with a label that is easily detectable by Raman spectroscopy. Another idea would be to use surface enhanced Raman spectroscopy (SERS) to improve sensitivity. The use of other characterization techniques like AFM and XPS should also help in understanding the reaction. Furthermore, the synthesis of the homemade diazonium salt should also be optimized for future work as this is not the case at the time of writing.

The functionalization routes were also successfully applied to amorphous carbon structures and a provisional DNA sensor was developed. The structures were composed of a solid core and a nanostructured outer layer, resulting in a huge surface area available for functionalization. Confocal fluorescence microscopy has demonstrated that the amorphous carbon structures were successfully functionalized with DNA strands via both the fatty acid and the diazonium route. The potential use in DNA sensors was further investigated by measuring the electrical resistance over the structures before and after DNA binding. Their potential as DNA sensor platforms was shown by a 40 % difference in resistance change after DNA binding between EDC-positive samples and EDC-negative references. A comparison with bulk structures, lacking the nanostructured outer layer, emphasized the importance of the nanostructured layer as the bulk structures did not show a difference in resistance change. A drawback of the system is the fact that the resistance increased for all sample types, including EDC-negative samples where no DNA is bonded. The amount of the increase in resistance however, is dependent on DNA binding. Elimination of this basic increase should improve sensor capabilities and facilitate the understanding of the sensing processes. Therefore, future work should investigate the origin of the resistance increase and try to eliminate it. A possible explanation for the resistance increase is the damaging of the carbon-substrate contact. If this turns out to be the case, the development of more robust structures could improve this shortcoming. Future work should also explore the effect of DNA hybridization and denaturation events on the electrical resistance. If the structures prove to be sensitive for these events, it becomes possible to perform selectivity and reusability tests.

As the development of graphene/graphite based DNA sensors with electrical readout require insight into the electronic properties of these materials, first steps were taken in this direction by the electronic characterization of ultrathin graphite flakes. This electronic characterization was achieved by depositing electrical contacts, in a van der Pauw configuration, on individual flakes using e-beam lithography. Resistivity was inversely related to temperature and the samples showed a sheet resistivity of only 40 – 55 μΩcm at room temperature. A giant positive magnetoresistance behavior was found in magnetic fields as low as 2.06 T. At 300 K, a magnetoresistance effect of 130 % was observed. Furthermore, investigation of the field dependence of the Hall voltage showed an initial linear increase followed by a downward bent as the magnetic field increased. This downward bent in the Hall voltage field dependence could be explained by a combination of the presence of magnetic moments in the samples and a field-dependent ratio of hole and electron carrier mobilities. The charge carrier density and mobility were also determined. Although lower than for true graphene, charge carrier mobilities found in this thesis were still very high (1329 cm^2/Vs at 77 K and $n= 8.28 \times 10^{19}$ cm^{-3}). These results contribute to the comprehension of the electronic properties of graphene-based materials and confirm the statements about the exceptional nature of graphene and related materials. Suggestions for the future continuation of this aspect of the thesis would be to study the electronic properties of these flakes in the presence of gate voltages. Finally, the ultimate goal for the future should be the combination of functionalization and electronic measurements on graphene layers. Investigation of the effect of DNA binding and DNA hybridization on the electronic properties of graphene would be a huge step forward in the development of graphene-based DNA sensors.

References

1. Novoselov, K.S. et al. Electric field effect in atomically thin carbon films. *Science* **306**, 666-669 (2004).
2. Lin, J. et al. Gating of Single-Layer Graphene with Single-Stranded Deoxyribonucleic Acids. *Small* **6**, 1150-1155 (2010).
3. Mohanty, N. & Berry, V. Graphene-Based Single-Bacterium Resolution Biodevice and DNA Transistor: Interfacing Graphene Derivatives with Nanoscale and Microscale Biocomponents. *Nano Lett.* **8**, 4469-4476 (2008).
4. Zhang, B. & Cui, T. An ultrasensitive and low-cost graphene sensor based on layer-by-layer nano self-assembly. *Appl. Phys. Lett.* **98**, 073116-073118 (2011).
5. Schedin, F. et al. Detection of individual gas molecules adsorbed on graphene. *Nat Mater* **6**, 652-655 (2007).
6. Wikipedia http://en.wikipedia.org/wiki/Orbital_hybridisation. (2011).
7. Chang, R. http://www.mhhe.com/physsci/chemistry/essentialchemistry. (2001).at <http://www.mhhe.com/physsci/chemistry/essentialchemistry>
8. Schafhaeutl, C. On the combinations of carbon with silicon and iron, and other metals, forming the different species of cast iron, steel, and malleable iron. *Phil. Mag.* **16**, 570-590 (1840).
9. Schafhaeutl, C. Ueber die Verbindungen des Kohlenstoffes mit Silicium, Eisen und anderen Metallen, welche die verschiedenen Gallungen von Roheisen, Stahl und Schmiedeeisen bilden. *J. Prakt. Chem.* **21**, 129-157 (1840).
10. Brodie, C. On the Atomic Weight of Graphite. *Phil. Trans. R. Soc. Lon.* **149**, 249 (1859).
11. Staudenmaier, L. Verfahren zur Darstellung der Graphitsäure. *Ber. Deut. Chem. Ges.* **31**, 1481-1487 (1898).
12. Wallace, P.R. The Band Theory of Graphite. *Phys. Rev.* **71**, 622-634 (1947).
13. Slonczewski, J. & Weiss, P. Band structure of graphite. *Phys. Rev.* **109**, 272-279 (1958).
14. McClure, J. Diamagnetism of graphite. *Phys. Rev.* **104**, 666-671 (1956).
15. Boehm, H., Clauss, A., Hofmann, U. & Fischer, G. Dunnste kohlenstoff-folien. *Z Naturforsch pt B* **B 17**, 150-153 (1962).
16. Shelton, J., Patil, H. & Blakely, J. Equilibrium segregation of carbon to

a nickel (111) surface: A surface phase transition. *Surf. Sci.* **43**, 493-520 (1974).
17. Eizenberg, M. & Blakely, J. Carbon monolayer phase condensation on Ni(111). *Surface Science* **82**, 228-236 (1979).
18. Boehm, H., Setton, R. & Stumpp, E. Nomenclature and terminology of graphite intercalation compounds. *Carbon* **24**, 241-245 (1986).
19. Dreyer, D.R., Ruoff, R.S. & Bielawski, C.W. From Conception to Realization: An Historial Account of Graphene and Some Perspectives for Its Future. *Angew. Chem. Int. Ed.* **49**, 9336-9344 (2010).
20. McNaught, A. & Wilkinson, A. *Compendium of chemical terminology*. (IUPAC, Blackwell Scientific: Oxford, 1997).
21. Mermin, N.D. Crystalline Order in Two Dimensions. *Phys. Rev.* **176**, 250-254 (1968).
22. Peierls, R.E. Quelques propriétés typiques des corps solides. *Ann. I. H. Poincare* **5**, 177-222 (1935).
23. Landau, L. Zur Theorie der Phasenumwandlungen II. *Phys. Zeits. Sowjetunion* **11**, 26-47 (1937).
24. Geim, A. & Novoselov, K. The rise of graphene. *Nat Mater* **6**, 183-191 (2007).
25. Stolyarova, E. et al. High-resolution scanning tunneling microscopy imaging of mesoscopic graphene sheets on an insulating surface. *Proc. Natl. Acad. Sci. U.S.A.* **104**, 9209-9212 (2007).
26. Meyer, J. et al. The structure of suspended graphene sheets. *Nature* **446**, 60-63 (2007).
27. Carlsson, J. Buckle or break. *Nat Mater* **6**, 801-802 (2007).
28. Fasolino, A., Los, J. & Katsnelson, M. Intrinsic ripples in graphene. *Nat Mater* **6**, 858-861 (2007).
29. Sinitsyna, O. & Yaminsky, I. Atomic resolution probe microscopy of the graphite surface. *usp khim* **75**, 27-35 (2006).
30. Kwiecinska, B. & Petersen, H. Graphite, semi-graphite, natural coke, and natural char classification - ICCP system. *Int. J. Coal Geol.* **57**, 99-116 (2004).
31. Terrones, M. et al. Graphene and graphite nanoribbons: Morphology, properties, synthesis, defects and applications. *Nano Today* **5**, 351-372 (2010).
32. Rutter, G.M. et al. Scattering and Interference in Epitaxial Graphene. *Science* **317**, 219 -222 (2007).
33. Thrower, P. The study of defects in graphite by transmission electron microscopy. *Chem Phys Carbon* **5**, 262-320 (1969).
34. Stone, A. & Wales, D. Theoretical studies of icosahedral C60 and

some related species. *Chem Phys Lett* **128**, 501-503 (1986).

35. Liu, Z., Suenaga, K., Harris, P.J.F. & Iijima, S. Open and Closed Edges of Graphene Layers. *Phys. Rev. Lett.* **102**, 015501 (2009).
36. Girit, Ç.Ö. et al. Graphene at the Edge: Stability and Dynamics. *Science* **323**, 1705 -1708 (2009).
37. Son, Y., Cohen, M.L. & Louie, S.G. Half-metallic graphene nanoribbons. *Nature* **444**, 347-349 (2006).
38. Nakada, K., Fujita, M., Dresselhaus, G. & Dresselhaus, M.S. Edge state in graphene ribbons: Nanometer size effect and edge shape dependence. *Phys. Rev. B* **54**, 17954-17961 (1996).
39. Yang, L., Park, C., Son, Y., Cohen, M.L. & Louie, S.G. Quasiparticle Energies and Band Gaps in Graphene Nanoribbons. *Phys. Rev. Lett.* **99**, 186801-186804 (2007).
40. Jiang, D., Sumpter, B.G. & Dai, S. Unique chemical reactivity of a graphene nanoribbon's zigzag edge. *J. Chem. Phys.* **126**, 134701-134716 (2007).
41. Boukhvalov, D. & Katsnelson, M. Chemical Functionalization of Graphene with Defects. *Nano Lett.* **8**, 4373-4379 (2008).
42. Geim, A. & Kim, P. Carbon wonderland. *Sci. Am.* **298**, 90-97 (2008).
43. Wilson, M. Electrons in atomically thin carbon sheets behave like massless particles. *Phys today* **59**, 21-23 (2006).
44. Novoselov, K.S. et al. Two-dimensional gas of massless Dirac fermions in graphene. *Nature* **438**, 197-200 (2005).
45. Partoens, B. & Peeters, F.M. From graphene to graphite: Electronic structure around the K point. *Phys. Rev. B* **74**, 075404-075411 (2006).
46. Novoselov, K. et al. Two-dimensional atomic crystals. *Proc. Natl. Acad. Sci. U.S.A.* **102**, 10451-10453 (2005).
47. Bolotin, K. et al. Ultrahigh electron mobility in suspended graphene. *Solid State Commun.* **146**, 351-355 (2008).
48. Fradkin, E. Critical behavior of disordered degenerate semiconductors. II. Spectrum and transport properties in mean-field theory. *Phys. Rev. B* **33**, 3263-3268 (1986).
49. Gusynin, V.P. & Sharapov, S.G. Unconventional Integer Quantum Hall Effect in Graphene. *Phys. Rev. Lett.* **95**, 146801-146804 (2005).
50. Peres, N., Neto, A. & Guinea, F. Conductance quantization in mesoscopic graphene. *Phys. Rev. B* **73**, 125411-125433 (2006).
51. Nilsson, J., Neto, A.H.C., Guinea, F. & Peres, N.M.R. Electronic Properties of Graphene Multilayers. *Phys. Rev. Lett.* **97**, 266801-266804 (2006).
52. Nomura, K. & MacDonald, A.H. Quantum Transport of Massless

Dirac Fermions. *Phys. Rev. Lett.* **98**, 076602-076605 (2007).

53. Tan, Y. et al. Measurement of Scattering Rate and Minimum Conductivity in Graphene. *Phys. Rev. Lett.* **99**, 246803-246806 (2007).
54. Zhang, Y., Tan, Y., Stormer, H.L. & Kim, P. Experimental observation of the quantum Hall effect and Berry's phase in graphene. *Nature* **438**, 201-204 (2005).
55. Katsnelson, M. Graphene: carbon in two dimensions. *Materials today* **10**, 20-27 (2007).
56. Zhang, Y. et al. Landau-Level Splitting in Graphene in High Magnetic Fields. *Phys. Rev. Lett.* **96**, 136806-136809 (2006).
57. Klein, O. Die Reflexion von Elektronen an einem Potentialsprung nach der relativistischen Dynamik von Dirac. *Z. Physik* **53**, 157-165 (1929).
58. Katsnelson, M.I., Novoselov, K.S. & Geim, A.K. Chiral tunnelling and the Klein paradox in graphene. *Nat Phys* **2**, 620-625 (2006).
59. Young, A.F. & Kim, P. Quantum interference and Klein tunnelling in graphene heterojunctions. *Nat Phys* **5**, 222-226 (2009).
60. Stander, N., Huard, B. & Goldhaber-Gordon, D. Evidence for Klein Tunneling in Graphene p-n Junctions. *Phys. Rev. Lett.* **102**, 026807-026810 (2009).
61. Luk'yanchuk, I.A. & Kopelevich, Y. Dirac and normal fermions in graphite and graphene: implications of the quantum Hall effect. *Phys. Rev. Lett* **97**, 256801 (2006).
62. Liu, F., Ming, P. & Li, J. Ab initio calculation of ideal strength and phonon instability of graphene under tension. *Phys. Rev. B* **76**, 064120-064126 (2007).
63. Zhao, Q., Nardelli, M.B. & Bernholc, J. Ultimate strength of carbon nanotubes: A theoretical study. *Phys. Rev. B* **65**, 144105-144110 (2002).
64. Lee, C., Wei, X., Kysar, J. & Hone, J. Measurement of the elastic properties and intrinsic strength of monolayer graphene. *Science* **321**, 385-388 (2008).
65. Frank, I.W., Tanenbaum, D.M., van der Zande, A.M. & McEuen, P.L. Mechanical properties of suspended graphene sheets. *J. Vac. Sci. Technol. B* **25**, 2558-2561 (2007).
66. Poot, M. & van der Zant, H.S.J. Nanomechanical properties of few-layer graphene membranes. *Appl. Phys. Lett.* **92**, 063111-063113 (2008).
67. Gómez-Navarro, C., Burghard, M. & Kern, K. Elastic Properties of Chemically Derived Single Graphene Sheets. *Nano Letters* **8**, 2045-2049 (2008).

68. Booth, T.J. et al. Macroscopic Graphene Membranes and Their Extraordinary Stiffness. *Nano Lett* **8**, 2442-2446 (2008).
69. Leenaerts, O., Partoens, B. & Peeters, F.M. Graphene: A perfect nanoballoon. *Appl. Phys. Lett.* **93**, 193107-3 (2008).
70. Bunch, J.S. et al. Impermeable Atomic Membranes from Graphene Sheets. *Nano Letters* **8**, 2458-2462 (2008).
71. Saito, K., Nakamura, J. & Natori, A. Ballistic thermal conductance of a graphene sheet. *Phys. Rev. B* **76**, 115409-115412 (2007).
72. Mingo, N. & Broido, D.A. Carbon Nanotube Ballistic Thermal Conductance and Its Limits. *Phys. Rev. Lett.* **95**, 096105-096108 (2005).
73. Peres, N.M.R., Lopes dos Santos, J.M.B. & Stauber, T. Phenomenological study of the electronic transport coefficients of graphene. *Phys. Rev. B* **76**, 073412-073415 (2007).
74. Balandin, A.A. et al. Superior Thermal Conductivity of Single-Layer Graphene. *Nano Lett* **8**, 902-907 (2008).
75. Calizo, I., Miao, F., Bao, W., Lau, C.N. & Balandin, A.A. Variable temperature Raman microscopy as a nanometrology tool for graphene layers and graphene-based devices. *Appl. Phys. Lett.* **91**, 071913-071915 (2007).
76. Kuzmenko, A.B., van Heumen, E., Carbone, F. & van der Marel, D. Universal Optical Conductance of Graphite. *Phys. Rev. Lett.* **100**, 117401-117404 (2008).
77. Nair, R.R. et al. Fine Structure Constant Defines Visual Transparency of Graphene. *Science* **320**, 1308-1308 (2008).
78. Eigler, S. A new parameter based on graphene for characterizing transparent, conductive materials. *Carbon* **47**, 2936-2939 (2009).
79. Ni, Z.H. et al. Graphene Thickness Determination Using Reflection and Contrast Spectroscopy. *Nano Lett* **7**, 2758-2763 (2007).
80. Mak, K.F. et al. Measurement of the Optical Conductivity of Graphene. *Phys. Rev. Lett.* **101**, 196405-196408 (2008).
81. Blake, P. et al. Making graphene visible. *Appl. Phys. Lett.* **91**, 063124-063133 (2007).
82. Roddaro, S., Pingue, P., Piazza, V., Pellegrini, V. & Beltram, F. The Optical Visibility of Graphene: Interference Colors of Ultrathin Graphite on SiO2. *Nano Letters* **7**, 2707-2710 (2007).
83. Casiraghi, C. et al. Rayleigh Imaging of Graphene and Graphene Layers. *Nano Lett* **7**, 2711-2717 (2007).
84. Yu, V. & Hilke, M. Large contrast enhancement of graphene monolayers by angle detection. *Appl. Phys. Lett.* **95**, 151904-151906

(2009).

85. Jung, I. et al. Simple Approach for High-Contrast Optical Imaging and Characterization of Graphene-Based Sheets. *Nano Lett* **7**, 3569-3575 (2007).
86. Gao, L., Ren, W., Li, F. & Cheng, H. Total Color Difference for Rapid and Accurate Identification of Graphene. *ACS Nano* **2**, 1625-1633 (2008).
87. Abergel, D.S.L., Russell, A. & Fal'ko, V.I. Visibility of graphene flakes on a dielectric substrate. *Appl. Phys. Lett.* **91**, 063125-063127 (2007).
88. Hummers, W. & Offeman, R. Preparation of Graphitic Oxide. *J. Am. Chem. Soc* **80**, 1339 (1958).
89. Schniepp, H.C. et al. Functionalized single graphene sheets derived from splitting graphite oxide. *J Phys Chem B* **110**, 8535-8539 (2006).
90. Cai, W. et al. Synthesis and Solid-State NMR Structural Characterization of 13C-Labeled Graphite Oxide. *Science* **321**, 1815-1817 (2008).
91. Hamilton, C. PhD thesis. (2009).
92. Paredes, J.I., Villar-Rodil, S., Martínez-Alonso, A. & Tascón, J.M.D. Graphene Oxide Dispersions in Organic Solvents. *Langmuir* **24**, 10560-10564 (2008).
93. Stankovich, S., Piner, R.D., Nguyen, S.T. & Ruoff, R.S. Synthesis and exfoliation of isocyanate-treated graphene oxide nanoplatelets. *Carbon* **44**, 3342-3347 (2006).
94. Stankovich, S. et al. Synthesis of graphene-based nanosheets via chemical reduction of exfoliated graphite oxide. *Carbon* **45**, 1558-1565 (2007).
95. Niyogi, S. et al. Solution properties of graphite and graphene. *J. Am. Chem. Soc* **128**, 7720-7721 (2006).
96. Gómez-Navarro, C. et al. Electronic Transport Properties of Individual Chemically Reduced Graphene Oxide Sheets. *Nano Letters* **7**, 3499-3503 (2007).
97. Lomeda, J., Doyle, C., Kosynkin, D., Hwang, W. & Tour, J. Diazonium Functionalization of Surfactant-Wrapped Chemically Converted Graphene Sheets. *J. Am. Chem. Soc* **130**, 16201-16206 (2008).
98. Stankovich, S. et al. Stable aqueous dispersions of graphitic nanoplatelets via the reduction of exfoliated graphite oxide in the presence of poly(sodium 4-styrenesulfonate). *J. Mater. Chem.* **16**, 155-158 (2006).

99. Li, D., Muller, M., Gilje, S., Kaner, R. & Wallace, G. Processable aqueous dispersions of graphene nanosheets. *Nat Nanotechnol* **3**, 101-105 (2008).
100. Gilje, S., Han, S., Wang, M., Wang, K. & Kaner, R. A chemical route to graphene for device applications. *Nano Lett.* **7**, 3394-3398 (2007).
101. Wang, G. et al. Facile Synthesis and Characterization of Graphene Nanosheets. *J phys Chem C* **112**, 8192-8195 (2008).
102. Si, Y. & Samulski, E.T. Synthesis of Water Soluble Graphene. *Nano Lett.* **8**, 1679-1682 (2008).
103. McAllister, M. et al. Single sheet functionalized graphene by oxidation and thermal expansion of graphite. *Chem. Mat.* **19**, 4396-4404 (2007).
104. Gengler, R.Y.N. et al. Large-Yield Preparation of High-Electronic-Quality Graphene by a Langmuirâ "Schaefer Approach. *Small* **6**, 35-39 (2010).
105. Hernandez, Y. et al. High-yield production of graphene by liquid-phase exfoliation of graphite. *Nat Nano* **3**, 563-568 (2008).
106. De, S. et al. Flexible, Transparent, Conducting Films of Randomly Stacked Graphene from Surfactant-Stabilized, Oxide-Free Graphene Dispersions. *Small* **6**, 458-464 (2010).
107. Berger, C. et al. Ultrathin epitaxial graphite: 2D electron gas properties and a route toward graphene-based nanoelectronics. *J Phys Chem B* **108**, 19912-19916 (2004).
108. Berger, C. et al. Electronic Confinement and Coherence in Patterned Epitaxial Graphene. *Science* **312**, 1191 -1196 (2006).
109. de Heer, W.A. et al. Epitaxial graphene. *Solid State Commun.* **143**, 92-100 (2007).
110. Ohta, T. et al. Morphology of graphene thin film growth on SiC(0001). *New J. Phys.* **10**, 023034-023041 (2008).
111. Emtsev, K. et al. Towards wafer-size graphene layers by atmospheric pressure graphitization of silicon carbide. *Nat Mater* **8**, 203-207 (2009).
112. Hass, J. et al. Highly ordered graphene for two dimensional electronics. *Appl. Phys. Lett.* **89**, 143106-143108 (2006).
113. Orlita, M. et al. Approaching the Dirac Point in High-Mobility Multilayer Epitaxial Graphene. *Phys. Rev. Lett.* **101**, 267601-267604 (2008).
114. Geim, A.K. Graphene: status and prospects. *Science* **324**, 1530-1534 (2009).
115. Li, X., Cai, W., Colombo, L. & Ruoff, R.S. Evolution of Graphene Growth on Ni and Cu by Carbon Isotope Labeling. *Nano Letters* **9**,

4268-4272 (2009).
116. Kim, K. et al. Large-scale pattern growth of graphene films for stretchable transparent electrodes. *Nature* **457**, 706-710 (2009).
117. Reina, A. et al. Large area, few-layer graphene films on arbitrary substrates by chemical vapor deposition. *Nano Lett* **9**, 30-35 (2009).
118. Yu, Q. et al. Graphene segregated on Ni surfaces and transferred to insulators. *Appl. Phys. Lett.* **93**, 113103-113105 (2008).
119. Grüneis, A. & Vyalikh, D.V. Tunable hybridization between electronic states of graphene and a metal surface. *Phys. Rev. B* **77**, 193401-193404 (2008).
120. Li, X. et al. Large-Area Synthesis of High-Quality and Uniform Graphene Films on Copper Foils. *Science* **324**, 1312-1314 (2009).
121. Sutter, P.W., Flege, J. & Sutter, E.A. Epitaxial graphene on ruthenium. *Nat Mater* **7**, 406-411 (2008).
122. Marchini, S., Günther, S. & Wintterlin, J. Scanning tunneling microscopy of graphene on Ru(0001). *Phys. Rev. B* **76**, 075429-075437 (2007).
123. Wintterlin, J. & Bocquet, M. Graphene on metal surfaces. *Surf. Sci.* **603**, 1841-1852 (2009).
124. Li, X. et al. Transfer of Large-Area Graphene Films for High-Performance Transparent Conductive Electrodes. *Nano Lett.* **9**, 4359-4363 (2009).
125. Cai, J. et al. Atomically precise bottom-up fabrication of graphene nanoribbons. *Nature* **466**, 470-473 (2010).
126. Kosynkin, D.V. et al. Longitudinal unzipping of carbon nanotubes to form graphene nanoribbons. *Nature* **458**, 872-876 (2009).
127. Cataldo, F. et al. Graphene nanoribbons produced by the oxidative unzipping of single-wall carbon nanotubes. *Carbon* **48**, 2596-2602 (2010).
128. Jiao, L., Zhang, L., Wang, X., Diankov, G. & Dai, H. Narrow graphene nanoribbons from carbon nanotubes. *Nature* **458**, 877-880 (2009).
129. Loh, K., Bao, Q., Ang, P. & Yang, J. The chemistry of graphene. *JOURNAL OF MATERIALS CHEMISTRY* **20**, 2277-2289 (2010).
130. Sofo, J., Chaudhari, A. & Barber, G. Graphane: A two-dimensional hydrocarbon. *Phys. Rev. B* **75**, 153401-153404 (2007).
131. Elias, D.C. et al. Control of Graphene's Properties by Reversible Hydrogenation: Evidence for Graphane. *Science* **323**, 610 -613 (2009).
132. http://www.condmat.physics.manchester.ac.uk/pictures/. (2006).
133. Cheng, S. et al. Reversible fluorination of graphene: Evidence of a two-dimensional wide bandgap semiconductor. *Phys. Rev. B* **81**,

205435-205439 (2010).

134. Koehler, F.M., Jacobsen, A., Ensslin, K., Stampfer, C. & Stark, W.J. Selective Chemical Modification of Graphene Surfaces: Distinction Between Single- and Bilayer Graphene. *Small* **6**, 1125-1130 (2010).
135. Bekyarova, E. et al. Chemical modification of epitaxial graphene: spontaneous grafting of aryl groups. *J. Am. Chem. Soc* **131**, 1336-1337 (2009).
136. Niyogi, S. et al. Spectroscopy of Covalently Functionalized Graphene. *Nano Lett.* **10**, 4061-4066 (2010).
137. Dyke, C., Stewart, M., Maya, F. & Tour, J. Diazonium-based functionalization of carbon nanotubes: XPS and GC-MS analysis and mechanistic implications. *Synlett* **1**, 155-160 (2004).
138. Farmer, D.B. et al. Chemical Doping and Electron−Hole Conduction Asymmetry in Graphene Devices. *Nano Lett.* **9**, 388-392 (2009).
139. Salvio, R. et al. The Formation of Large-Area Conducting Graphene-Like Platelets. *Chem. Eur. J.* **15**, 8235-8240 (2009).
140. Yang, H. et al. Covalent functionalization of polydisperse chemically-converted graphene sheets with amine-terminated ionic liquid. *Chem. Commun.* 3880 (2009).doi:10.1039/b905085j
141. Wang, S. et al. Band-like Transport in Surface-Functionalized Highly Solution-Processable Graphene Nanosheets. *Adv. Mater.* **20**, 3440-3446 (2008).
142. Salavagione, H.J., Gómez, M.A. & Martínez, G. Polymeric Modification of Graphene through Esterification of Graphite Oxide and Poly(vinyl alcohol). *Macromolecules* **42**, 6331-6334 (2009).
143. Veca, L.M. et al. Polymer functionalization and solubilization of carbon nanosheets. *Chem. Commun.* 2565-2567 (2009).doi:10.1039/b900590k
144. Stankovich, S. et al. Graphene-based composite materials. *Nature* **442**, 282-286 (2006).
145. Katz, E. Application of bifunctional reagents for immobilization of proteins on a carbon electrode surface: Oriented immobilization of photosynthetic reaction centers. *J. Electroanal. Chem.* **365**, 157-164 (1994).
146. Xu, Y., Bai, H., Lu, G., Li, C. & Shi, G. Flexible graphene films via the filtration of water-soluble noncovalent functionalized graphene sheets. *J. Am. Chem. Soc* **130**, 5856-5857 (2008).
147. Su, Q. et al. Composites of Graphene with Large Aromatic Molecules. *Adv. Mater.* **21**, 3191-3195 (2009).
148. Wang, Y., Chen, X., Zhong, Y., Zhu, F. & Loh, K.P. Large area,

continuous, few-layered graphene as anodes in organic photovoltaic devices. *Appl. Phys. Lett.* **95**, 063302-063304 (2009).

149. Wang, X., Tabakman, S.M. & Dai, H. Atomic layer deposition of metal oxides on pristine and functionalized graphene. *J. Am. Chem. Soc* **130**, 8152-8153 (2008).
150. Wu, J. et al. A biosensor monitoring DNA hybridization based on polyaniline intercalated graphite oxide nanocomposite. *Sens Actuators B Chem* **104**, 43-49 (2005).
151. Lu, C., Yang, H., Zhu, C., Chen, X. & Chen, G. A Graphene Platform for Sensing Biomolecules. *Angew. Chem. Int. Ed.* **48**, 4785-4787 (2009).
152. Tang, Z. et al. Constraint of DNA on Functionalized Graphene Improves its Biostability and Specificity. *Small* **9999**, NA (2010).
153. Varghese, N. et al. Binding of DNA Nucleobases and Nucleosides with Graphene. *ChemPhysChem* **10**, 206-210 (2009).
154. Lin, Y. et al. 100-GHz Transistors from Wafer-Scale Epitaxial Graphene. *Science* **327**, 662-662 (2010).
155. Ponomarenko, L.A. et al. Chaotic Dirac Billiard in Graphene Quantum Dots. *Science* **320**, 356-358 (2008).
156. Sordan, R., Traversi, F. & Russo, V. Logic gates with a single graphene transistor. *Appl. Phys. Lett.* **94**, 073305-073307 (2009).
157. Chen, Z., Lin, Y., Rooks, M. & Avouris, P. Graphene nano-ribbon electronics. *Phys. E* **40**, 228-232 (2007).
158. Li, X., Wang, X., Zhang, L., Lee, S. & Dai, H. Chemically Derived, Ultrasmooth Graphene Nanoribbon Semiconductors. *Science* **319**, 1229-1232 (2008).
159. Wassei, J. & Kaner, R. Graphene, a promising transparent conductor. *Materials today* **13**, 52-59 (2010).
160. Wang, S. et al. High Mobility, Printable, and Solution-Processed Graphene Electronics. *Nano Letters* **10**, 92-98 (2010).
161. Tien, H., Huang, Y., Yang, S., Wang, J. & Ma, C.M. The production of graphene nanosheets decorated with silver nanoparticles for use in transparent, conductive films. *Carbon* **In Press, Corrected Proof**,
162. Wang, Y., Chen, X., Zhong, Y., Zhu, F. & Loh, K.P. Large area, continuous, few-layered graphene as anodes in organic photovoltaic devices. *Appl. Phys. Lett.* **95**, 063302-063304 (2009).
163. Wang, X., Zhi, L. & Mullen, K. Transparent, Conductive Graphene Electrodes for Dye-Sensitized Solar Cells. *Nano Lett.* **8**, 323-327 (2008).
164. Wu, J. et al. Organic Light-Emitting Diodes on Solution-Processed

Graphene Transparent Electrodes. *ACS Nano* **4**, 43-48 (2010).

165. Blake, P. et al. Graphene-Based Liquid Crystal Device. *Nano Lett.* **8**, 1704-1708 (2008).
166. Robinson, J.T., Perkins, F.K., Snow, E.S., Wei, Z. & Sheehan, P.E. Reduced Graphene Oxide Molecular Sensors. *Nano Lett.* **8**, 3137-3140 (2008).
167. Tang, L. et al. Preparation, Structure, and Electrochemical Properties of Reduced Graphene Sheet Films. *Adv. Funct. Mater.* **19**, 2782-2789 (2009).
168. Dan, Y., Lu, Y., Kybert, N.J., Luo, Z. & Johnson, A.T.C. Intrinsic Response of Graphene Vapor Sensors. *Nano Lett.* **9**, 1472-1475 (2009).
169. Mohanty, N. & Berry, V. Graphene-based single-bacterium resolution biodevice and DNA transistor: interfacing graphene derivatives with nanoscale and microscale biocomponents. *Nano Lett* **8**, 4469-4476 (2008).
170. Ohno, Y., Maehashi, K., Yamashiro, Y. & Matsumoto, K. Electrolyte-Gated Graphene Field-Effect Transistors for Detecting pH and Protein Adsorption. *Nano Lett.* **9**, 3318-3322 (2009).
171. Li, F. et al. A graphene-enhanced molecular beacon for homogeneous DNA detection. *Nanoscale* **2**, 1021-1026 (2010).
172. Lee, J.K., Smith, K.B., Hayner, C.M. & Kung, H.H. Silicon nanoparticles–graphene paper composites for Li ion battery anodes. *Chem. Commun.* **46**, 2025-2027 (2010).
173. Yoo, E. et al. Large Reversible Li Storage of Graphene Nanosheet Families for Use in Rechargeable Lithium Ion Batteries. *Nano Lett.* **8**, 2277-2282 (2008).
174. Stoller, M.D., Park, S., Zhu, Y., An, J. & Ruoff, R.S. Graphene-Based Ultracapacitors. *Nano Lett.* **8**, 3498-3502 (2008).
175. Li, F. et al. One-step synthesis of graphene/SnO2 nanocomposites and its application in electrochemical supercapacitors. *Nanotechnology* **20**, 455606-455611 (2009).
176. Srinivas, G. et al. Synthesis of graphene-like nanosheets and their hydrogen adsorption capacity. *Carbon* **48**, 630-635 (2010).
177. Bunch, J.S. et al. Electromechanical Resonators from Graphene Sheets. *Science* **315**, 490-493 (2007).
178. Meyer, J., Girit, C., Crommie, M. & Zettl, A. Imaging and dynamics of light atoms and molecules on graphene. *Nature* **454**, 319-322 (2008).
179. Kuilla, T. et al. Recent advances in graphene based polymer composites. *Prog. Polym. Sci.* **35**, 1350-1375 (2010).

180. Bulkin, B. *Analytical Raman Spectroscopy*. (John Wiley & Sons, Inc.: New York, 1991).
181. Ferraro, J. & Nakamoto, K. *Introductory Raman Spectroscopy*. (Academic Press: San Diego, 1994).
182. Vidano, R.P., Fischbach, D.B., Willis, L.J. & Loehr, T.M. Observation of Raman band shifting with excitation wavelength for carbons and graphites. *Solid State Commun.* **39**, 341-344 (1981).
183. Tuinstra, F. Raman Spectrum of Graphite. *J. Chem. Phys.* **53**, 1126-1130 (1970).
184. Ferrari, A.C. et al. Raman Spectrum of Graphene and Graphene Layers. *Phys. Rev. Lett.* **97**, 187401-187404 (2006).
185. Gupta, A., Chen, G., Joshi, P., Tadigadapa, S. & Eklund Raman Scattering from High-Frequency Phonons in Supported n-Graphene Layer Films. *Nano Lett.* **6**, 2667-2673 (2006).
186. Ferralis, N. Probing mechanical properties of graphene with Raman spectroscopy. *J Mater Sci* **45**, 5135-5149 (2010).
187. Ferrari, A.C. & Robertson, J. Interpretation of Raman spectra of disordered and amorphous carbon. *Phys. Rev. B* **61**, 14095-14107 (2000).
188. http://www3.physik.uni-greifswald.de/method/afm/eafm.htm. (2001).
189. http://www.microscopy.ethz.ch/sem.htm. (2009).
190. http://www.olympusmicro.com/primer/java/jablonski/jabintro/index.html. (2010).
191. Malesevic, A. et al. Synthesis of few-layer graphene via microwave plasma-enhanced chemical vapour deposition. *Nanotechnology* **19**, 305604-305609 (2008).
192. Malesevic, A. et al. Combined growth of carbon nanotubes and carbon nanowalls by plasma-enhanced chemical vapor deposition. *Carbon* **45**, 2932-2937 (2007).
193. Yu, J. et al. Vertically Aligned Boron Nitride Nanosheets: Chemical Vapor Synthesis, Ultraviolet Light Emission, and Superhydrophobicity. *ACS Nano* **4**, 414-422 (2010).
194. BenMoussa, B. et al. Hexagonal Boron Nitride Nanowalls Synthesized by Unbalanced RF Magnetron Sputtering. *Mater. res. soc. symp. p.* **1307**, null (2011).
195. Wenmackers, S. et al. Diamond-based DNA sensors: surface functionalization and read-out strategies. *Phys. Stat. Sol.(a)* **206**, 391-408 (2009).
196. Wenmackers, S. et al. DNA attachment to nanocrystalline diamond

films. *Phys. Stat. Sol.(a)* **202**, 2212-2216 (2005).

197. Yang, W. et al. DNA-modified nanocrystalline diamond thin-films as stable, biologically active substrates. *Nat Mater* **1**, 253-257 (2002).
198. Christiaens, P. et al. EDC-mediated DNA attachment to nanocrystalline CVD diamond films. *Biosens Bioelectron* **22**, 170-177 (2006).
199. Vermeeren, V. et al. Towards a real-time, label-free, diamond-based DNA sensor. *Langmuir* **23**, 13193-202 (2007).
200. Vermeeren, V. et al. Topographical and Functional Characterization of the ssDNA Probe Layer Generated Through EDC-Mediated Covalent Attachment to Nanocrystalline Diamond Using Fluorescence Microscopy. *Langmuir* **24**, 9125-9134 (2008).
201. van Grinsven, B. et al. Rapid assessment of the stability of DNA duplexes by impedimetric real-time monitoring of chemically induced denaturation. *Lab Chip* **11**, 1656-1663 (2011).
202. Jaegfeldt, H., Kuwana, T. & Johansson, G. Electrochemical stability of catechols with a pyrene side chain strongly adsorbed on graphite electrodes for catalytic oxidation of dihydronicotinamide adenine dinucleotide. *J. Am. Chem. Soc.* **105**, 1805-1814 (1983).
203. Chen, R.J., Zhang, Y., Wang, D. & Dai, H. Noncovalent sidewall functionalization of single-walled carbon nanotubes for protein immobilization. *J. Am. Chem. Soc.* **123**, 3838-3839 (2001).
204. He, S. et al. A Graphene Nanoprobe for Rapid, Sensitive, and Multicolor Fluorescent DNA Analysis. *Adv. Funct. Mater.* **20**, 453-459 (2010).
205. Bahr, J. et al. Functionalization of carbon nanotubes by electrochemical reduction of aryl diazonium salts: A bucky paper electrode. *J. Am. Chem. Soc* **123**, 6536-6542 (2001).
206. Dyke, C. & Tour, J. Unbundled and highly functionalized carbon nanotubes from aqueous reactions. *Nano Lett.* **3**, 1215-1218 (2003).
207. Bahr, J. & Tour, J. Highly functionalized carbon nanotubes using in situ generated diazonium compounds. *Chem. Mat.* **13**, 3823-3824 (2001).
208. Yoo, B. et al. Self-assembly of functionalized single-walled carbon nanotubes prepared from aryl diazonium compounds on Ag surfaces. *Mater. Lett.* **60**, 3224-3226 (2006).
209. Dyke, C. & Tour, J. Solvent-free functionalization of carbon nanotubes. *J. Am. Chem. Soc* **125**, 1156-1157 (2003).
210. Dyke, C. & Tour, J. Covalent functionalization of single-walled carbon nanotubes for materials applications. *J. Phys. Chem. A* **108**, 11151-

11159 (2004).

211. Strano, M.S. et al. Electronic Structure Control of Single-Walled Carbon Nanotube Functionalization. *Science* **301**, 1519-1522 (2003).
212. Kizil, M., Yilmaz, E., Pirinccioglu, N. & Aytekin, C. DNA cleavage activity of diazonium salts: Chemical nucleases. *Turk. J. Chem.* **27**, 539-544 (2003).
213. Beckwith, A.L.J. & Gara, W.B. Some intramolecular reactions of ortho-substituted aryl radicals. *J. Chem. Soc., Perkin Trans. 2* **6**, 593-600 (1975).
214. D'Amour, M. & Bélanger, D. Stability of Substituted Phenyl Groups Electrochemically Grafted at Carbon Electrode Surface. *J. Phys. Chem. B* **107**, 4811-4817 (2003).
215. Saby, C., Ortiz, B., Champagne, G. & Belanger, D. Electrochemical modification of glassy carbon electrode using aromatic diazonium salts .1. Blocking effect of 4-nitrophenyl and 4-carboxyphenyl groups. *Langmuir* **13**, 6805-6813 (1997).
216. Whetsel, K.B., Hawkins, G.F. & Johnson, F.E. The Infrared Spectra of Aryldiazonium Salts. *J. Am. Chem. Soc.* **78**, 3360-3363 (1956).
217. Anderson, P.W. Absence of Diffusion in Certain Random Lattices. *Phys. Rev.* **109**, 1492-1505 (1958).
218. Van der Linden, W.E. & Dieker, J.W. Glassy carbon as electrode material in electro- analytical chemistry. *Anal. Chim. Acta* **119**, 1-24 (1980).
219. Cespugli, R., Sarda, N., Gharib, A., Faradji, H. & Chastrette, N. Differential pulse voltammetry in vivo with working carbon fiber electrodes: 5-hydroxyindole compounds or uric acid detection? *Exp Brain Res* **64**, 589-595 (1986).
220. Dittmar, A. et al. In vivo and in vitro evaluation of specially designed gold and carbon fiber oxygen microelectrodes for living tissues. *Sens Actuators B Chem* **44**, 316-320 (1997).
221. Ikeda, O., Ohtani, M., Yamaguchi, T. & Komura, A. Direct electrochemistry of cytochrome c at a glassy carbon electrode covered with a microporous alumina membrane. *Electrochim. Acta* **43**, 833-839 (1997).
222. Brett, A.M.O., Serrano, S.H.P., Gutz, I., La-Scalea, M.A. & Cruz, M.L. Voltammetric behavior of nitroimidazoles at a DNA-biosensor. *Electroanalysis* **9**, 1132-1137 (1997).
223. Schueller, O., Brittain, S. & Whitesides, G. Fabrication of glassy carbon microstructures by soft lithography. *Sens Actuators A Phys.* **72**, 125-139 (1999).

224. Wang, Y., Pham, L., Vasconcellos, G.P.S.D. & Madou, M. Fabrication and characterization of micro PEM fuel cells using pyrolyzed carbon current collector plates. *J. Power Sources* **195**, 4796-4803 (2010).
225. Lin, P., Park, B.Y. & Madou, M.J. Development and characterization of a miniature PEM fuel cell stack with carbon bipolar plates. *J. Power Sources* **176**, 207-214 (2008).
226. Teixidor, G.T. et al. Carbon microelectromechanical systems as a substratum for cell growth. *Biomed. Mater.* **3**, 034116-034123 (2008).
227. Blazewicz, M. Carbon materials in the treatment of soft and hard tissue injuries. *Eur. Cells Mater.* **2**, 21-29 (2001).
228. Rettig, H., Weber, U., Bruckmann, H., Rosenblatt, U. & Huttinger, K. Carbon as an implant material in orthopedic-surgery. *Arch. Orthop. Trauma Surg.* **94**, 241-244 (1979).
229. Bokros, J. Carbon biomedical devices. *Carbon* **15**, 355-371 (1977).
230. Kroschwitz, J. & Howe-Grant, M. *Kirk-Othmer Encyclopedia of Chemical Technology*. (Wiley: New York, 1991).
231. Tamor, M.A. & Vassell, W.C. Raman ''fingerprinting'' of amorphous carbon films. *J. Appl. Phys.* **76**, 3823-3830 (1994).
232. Leenaerts, O., Partoens, B. & Peeters, F. Adsorption of H2O, NH3, CO, NO2, and NO on graphene: A first-principles study. *Phys. Rev. B* **77**, 125416-125423 (2008).
233. Leenaerts, O., Partoens, B. & Peeters, F.M. Paramagnetic adsorbates on graphene: A charge transfer analysis. *Appl. Phys. Lett.* **92**, 243125-243133 (2008).
234. Barzola-Quiquia, J., Yao, J., Rodiger, P., Schindler, K. & Esquinazi, P. Sample size effects on the transport characteristics of mesoscopic graphite samples. *Phys. Stat. Sol.(a)* **205**, 2924-2933 (2008).
235. Baibich, M.N. et al. Giant Magnetoresistance of (001)Fe/(001)Cr Magnetic Superlattices. *Phys. Rev. Lett.* **61**, 2472-2475 (1988).
236. Binasch, G., Grünberg, P., Saurenbach, F. & Zinn, W. Enhanced magnetoresistance in layered magnetic structures with antiferromagnetic interlayer exchange. *Phys. Rev. B* **39**, 4828-4830 (1989).
237. von Helmolt, R., Wecker, J., Holzapfel, B., Schultz, L. & Samwer, K. Giant negative magnetoresistance in perovskitelike La_{2/3}Ba_{1/3}MnO_{x} ferromagnetic films. *Phys. Rev. Lett.* **71**, 2331-2333 (1993).
238. Wagner, P. et al. Spin Dependent Hopping and Colossal Negative Magnetoresistance in Epitaxial Nd_{0.52}Sr_{0.48}MnO_{3} Films in Fields up to 50 T. *Phys. Rev. Lett.* **81**, 3980-3983 (1998).

239. Verbanck, G. et al. Large positive magnetoresistance in Cr/Ag/Cr trilayers. *Appl. Phys. Lett.* **70**, 1477-1479 (1997).
240. Willems, B.L. et al. Negative magnetoresistance in boron-doped nanocrystalline diamond films. *J. Appl. Phys.* **106**, 033711-033714 (2009).
241. Ziman, J. *Electrons and Phonons*. (Clarendon Press: Oxford, 1963).
242. McKenzie, R.H., Qualls, J.S., Han, S.Y. & Brooks, J.S. Violation of Kohler's rule by the magnetoresistance of a quasi-two-dimensional organic metal. *Phys. Rev. B* **57**, 11854-11857 (1998).
243. Harris, J.M. et al. Violation of Kohler's Rule in the Normal-State Magnetoresistance of YBa_{2}Cu_{3}O_{7- delta } and La_{2}Sr_{x}CuO_{4}. *Phys. Rev. Lett.* **75**, 1391-1394 (1995).
244. Esquinazi, P. et al. Ferromagnetism in oriented graphite samples. *Phys. Rev. B* **66**, 024429-024438 (2002).
245. Berashevich, J. & Chakraborty, T. Sustained ferromagnetism induced by H-vacancies in graphane. *Nanotechnology* **21**, 355201 (2010).
246. Jakob, G. et al. Scaling of the angular dependence of the critical current density in high-T_{c} superconductors. *Phys. Rev. B* **47**, 12099-12103 (1993).
247. Kopelevich, Y., Medina Pantoja, J., da Silva, R., Mrowka, F. & Esquinazi, P. Anomalous Hall effect in graphite. *Phys. Lett. A* **355**, 233-236 (2006).
248. Kopelevich, Y. et al. Searching for the Fractional Quantum Hall Effect in Graphite. *Phys. Rev. Lett.* **103**, 116802-116805 (2009).
249. Stamenov, P., Krstic, V. & Coey, J. Shubnikov-de Haas and Hall quantum oscillations in graphite. *J. Magn. Magn. Mater.* **290**, 1402-1404 (2005).
250. Jakob, G., Martin, F., Westerburg, W. & Adrian, H. Evidence of charge-carrier compensation effects in La_{0.67}Ca_{0.33}MnO_{3}. *Phys. Rev. B* **57**, 10252-10255 (1998).
251. Wagner, P., Mazilu, D., Trappeniers, L., Moshchalkov, V.V. & Bruynseraede, Y. Anomalous Hall effect in thin films of Pr_{0.5}Sr_{0.5}MnO_{3}. *Phys. Rev. B* **55**, 14721-14724 (1997).
252. Ugeda, M.M., Brihuega, I., Guinea, F. & Gómez-Rodríguez, J.M. Missing Atom as a Source of Carbon Magnetism. *Phys. Rev. Lett.* **104**, 096804-096807 (2010).
253. Ramos, M.A. et al. Magnetic properties of graphite irradiated with MeV ions. *Phys. Rev. B* **81**, 214404-214419 (2010).

Appendix 1: List of abbreviations

AFM	Atomic force microscopy
Ag	Silver
$CHCl_3$	Chloroform
CMR	Colossal magnetoresistance
CNT	Carbon nanotubes
CNW	Carbon nanowalls
Cr	Chromium
Cu	Copper
CVD	Chemical vapor deposition
DNA	Deoxyribonucleic acid
e	Elementary charge
EDC	1-ethyl-3-(3-dimethylaminopropyl)-carbodiimide
E_f	Fermi energy
FA	Fatty acid
Fe	Iron
FLG	Few-layer graphene
FWHM	Full width at half maximum
h	Planck's constant
HOPG	Highly oriented pyrolytic graphite
hPa	hectoPascal

IgG	Immunoglobulin G
IPA	Isopropyl alcohol
MeOH	Methanol
MES	2-[N-morpholino]-ethanesulphonic acid buffer
MW PECVD	Microwave plasma-enhanced chemical vapor deposition
n	Charge carrier density
N_2	Nitrogen gas
PBA	Pyrene-1-boronic acid
PBS	Phosphate buffered saline
PCR	Polymerase chain reaction
PDA	1-Pyrene decanoic acid
PMMA	Poly(methyl methacrylate)
PMR	Positive magnetoresistance
QED	Quantum electrodynamics
QHE	Quantum Hall effect
sccm	Standard cubic centimeters per minute
SDS	Sodium dodecyl sulfate
SEM	Scanning electron microscopy
Si	Silicon
SiC	Silicon carbide
SiO_2	Silicon dioxide
SSC	Saline sodium citrate
STM	Scanning tunneling microscopy
TEM	Transmission electron microscopy

XPS	X-ray photoelectron spectroscopy
ρ	Resistivity
σ	Conductivity
μ	Charge carrier mobility

Appendix 2: Publications and conference contributions

Publications

"A MIP-based impedimetric sensor for the detection of low-MW molecules"
R. Thoelen, **R. Vansweevelt**, J. Duchateau, D. Vanderzande, M. Ameloot, T.J. Cleij, P. Wagner
Biosensors & Bioelectronics 23 (6), 913-918 (2008).

"Biological modification of carbon nanowalls with DNA strands and hybridization experiments with complementary and mismatched DNA"
R. Vansweevelt, A. Malesevic, M. Van Gompel, A. Vanhulsel, S. Wenmackers, J. D'Haen, V. Vermeeren, M. Ameloot, L. Michiels, C. Van Haesendonck, P. Wagner
Chemical Physics Letters 485, 196-201 (2010).

"Study on the giant positive magnetoresistance and Hall effect in ultrathin graphite flakes"
R. Vansweevelt, V. Mortet, J. D'Haen, B. Ruttens, C. Van Haesendonck, B. Partoens, F.M. Peeters, P. Wagner
Physica Status Solidi (A) 208 (6), 1252-1258 (2011).

"Hierarchical carbon nanowire microarchitectures made by plasma-assisted pyrolysis of photoresist"
M. De Volder, **R. Vansweevelt**, P. Wagner, D. Reynaerts, C. Van Hoof, A.J. Hart
Submitted to *ACS Nano*

Poster contributions

- General scientific meeting of the Belgian Physical Society (BPS), Brussels (Belgium), May 21st ,2008, Bioactivation of graphene-like nanostructures, synthesized by MW PECVD, with ssDNA. **R. Vansweevelt**, A. Malesevic, M.P. Chowdhury, A. Vanhulsel, S. Wenmackers, V. Vermeeren, C. Van Haesendonck, P. Wagner

- Joint general scientific meeting of the Belgian Physical Society and the Belgian Biophysical Society (BPS), Hasselt (Belgium), April 1st, 2009, Biological modification of carbon nanowalls with ss-DNA and subsequent hybridization**. R. Vansweevelt**, A. Malesevic, M. Van Gompel, A. Vanhulsel, S. Wenmackers, V. Vermeeren, L. Michiels, C. Van Haesendonck, P. Wagner

- Engineering of Functional Interfaces (EnFI), Hasselt (Belgium), June 18-19, 2009, Covalent DNA binding and hybridization experiments on carbon-nanowall platforms. **R. Vansweevelt**, A. Malesevic, A. Vanhulsel, M. Van Gompel, S. Wenmackers, J. D'Haen, V. Vermeeren, M. Ameloot, L. Michiels, C. Van Haesendonck, P. Wagner

- Annual meeting of the Inter University Attraction Poles (IAP), Louvain-la-Neuve (Belgium) November, 2009, Covalent DNA binding and hybridization experiments on carbon-nanowall platforms. **R. Vansweevelt**, A. Malesevic, A. Vanhulsel, M. Van Gompel, S. Wenmackers, J. D'Haen, V. Vermeeren, M. Ameloot, L. Michiels, C. Van Haesendonck, P. Wagner

- Diamond Workshop (SBDD XV), Hasselt (Belgium), February 22-24, 2010, Linking DNA to graphene-based materials and hybridization with complementary and mismatched DNA strands. **R. Vansweevelt**, A. Malesevic, A. Vanhulsel, M. Van Gompel, S. Wenmackers, J. D'Haen, V. Vermeeren, M. Ameloot, L. Michiels, C. Van Haesendonck, P. Wagner

- Joint meeting of the Belgian Physical Society and the Netherlands Physical Society (Fysica 2010), Utrecht, April 23rd, 2010, Linking DNA to graphene-based materials and hybridization with complementary and mismatched DNA strands. **R. Vansweevelt**, A. Malesevic, M. Van Gompel, J. Ryken, V. Vermeeren, M. Ameloot, L. Michiels, C. Van Haesendonck, A. Vanhulsel, P. Wagner

- World Congress on Biosensors, Glasgow (United Kingdom), May 26-28, 2010, Covalent linking of DNA strands to graphene-based carbon nanowalls. **R. Vansweevelt**, M. Van Gompel, A. Malesevic, V. Vermeeren, A. Vanhulsel, P. Wagner

- Engineering of Functional Interfaces (EnFI), Marburg (Germany), July 15-16, 2010, Biological modification of graphene-like carbon structures with DNA molecules. **R. Vansweevelt**, J. Ryken, A. Vanhulsel, V. Mortet, S. Janssens, V. Vermeeren, M. Ameloot, C. Van Haesendonck, P. Wagner
- Annual meeting of the Inter University Attraction Poles (IAP), Hasselt (Belgium), November 29-30, 2010, Study on the giant positive magneto-resistance and Hall effect in ultrathin graphite flakes. **R. Vansweevelt**, V. Mortet, J. D'Haen, B. Ruttens, C. Van Haesendonck, B. Partoens, F.M. Peeters, P. Wagner
- MRS Spring Meeting, San Francisco (USA), April 25-29, 2011, Modification of sp^2 hybridized carbon materials with DNA strands and their electrical characterization. **R. Vansweevelt**, A. Vanhulsel, V. Mortet, L. Michiels, C. Van Haesendonck, P. Wagner

Oral contributions

- Engineering of Functional Interfaces (EnFI), Hasselt (Belgium), June 18-19, 2009, Covalent DNA binding and hybridization experiments on carbon-nanowall platforms. **R. Vansweevelt**, A. Malesevic, A. Vanhulsel, M. Van Gompel, S. Wenmackers, J. D'Haen, V. Vermeeren, M. Ameloot, L. Michiels, C. Van Haesendonck, P. Wagner
- Engineering of Functional Interfaces (EnFI), Marburg (Germany), July 15-16, 2010, Biological modification of graphene-like carbon structures with DNA molecules. **R. Vansweevelt**, J. Ryken, A. Vanhulsel, V. Mortet, S. Janssens, V. Vermeeren, M. Ameloot, C. Van Haesendonck, P. Wagner

Both oral contributions were only very brief talks

Appendix 3: List of figures and tables

Figure 1-1. Illustration of different atomic orbital hybridizations of carbon. Adapted from [7]... 3

Figure 1-2. Number of manuscripts per year when the search term "graphene" was entered as topic in Web of Knowledge. 5

Figure 1-3. Artistic impression of a rippled graphene sheet [26]. 6

Figure 1-4. Graphene sheet (top) as the base for other sp^2 carbon materials. Folding yields 0D bucky balls (left) or 1D carbon nanotubes (middle). Stacking gives 3D graphite (right) [24]. 7

Figure 1-5. Illustration of Stone-Wales defect. Rotation of one carbon-carbon bond over 90°, resulting in two pentagons and two heptagons. 8

Figure 1-6. Electronic band structure of graphene, showing the dependence of energy on momentum. The right side illustrates the conical shape of the touching valence and conduction bands around the K point. [43] 9

Figure 1-7. Quantum Hall effect measurement on single and double (inset) layer graphene. The green and red curve show the longitudinal resistivity (ρ_{xx}) and the Hall conductivity (σ_{xy}) respectively in function of the carrier density (n) [44]....................................... 11

Figure 1-9. Optical microscopy image of a graphene flake (indicated by the arrow) produced by the Geim method. The flake is lying on top of a Si substrate with 300 nm SiO_2. The flake in the lower region of the image is about 3-5 layers thick. 18

Figure 1-10. Illustration of possible graphene oxide structure. [91] 19

Figure 1-11. Schematic representation of the Langmuir-Schaefer method.................... 20

Figure 1-12. Bottom-up fabrication of graphene nanoribbons starting from precursor monomers (10,10-dibromo-9,9-bianthryl). (A) Dehalogenation of adsorbed monomers. (B) Diffusion and polymerization of biradical species upon thermal activation. (C) Second thermal activation initiates cyclodehydrogenation to form graphene nanoribbons. Adapted from [125]. 24

Figure 1-13. Artistic impression of graphane. Small and large spheres correspond to hydrogen atoms and carbon atoms respectively. The proposed structure is one with crystalline order. [128] 26

Figure 1-14. Reaction of graphene oxide with sodium azide (NaN_3). Azide functionalities can be reduced with lithium aluminium hydride ($LiAlH_4$) to aminogroups (left) or used in click chemistry (right). 28

Figure 1-15. Reaction of graphene oxide with isocyanate to transform hydroxyl and carboxyl groups into carbamate esters and amides respectively. 29

Figure 2-1. Optical microscopy image of a flake on Si/SiO_2 300 nm. Letters indicate some parts with different thicknesses with "A" the thinnest and "G" the thickest part. "A" indicates single layer graphene, "B" bilayer graphene and "C" marks an area consisting of at least three layers. Different steps in thickness can be seen in the transition zone from "E" to "F". The image was taken with a 100x objective. 33

Figure 2-2. G vibration mode with E_{2g} symmetry. Adapted from [183]......................... 35

Figure 2-3. (A) Raman spectra of graphene and graphite. (B) Evolution of the G peak in function of the number of layers, indicated on the left. The G peak shifts by about 5.5 cm^{-1} when the thickness changes from single layer to 5 layers. (C) Evolution of the 2D peak in function of number of layers. All spectra are taken at λ_{ex} = 514 nm. Image is adapted from [180],[181]. 36

Figure 2-4. AFM principle. (A) illustration of the AFM working principle and setup. (B) Force-distance curve that forms the basis for the AFM principle. In contact mode there is a repulsive force between tip and sample. In non-contact mode there is attraction. [184]. 37

Figure 2-5. (A) AFM height image of a graphene flake. The upper right insert shows a magnification of the indicated area and the lower right insert shows the height profile of the black line, indicated in the upper right insert. The vertical distance between the red arrows is 0.416 nm, corresponding to single layer graphene. (B) AFM height image of IgG antibodies adsorbed on a HOPG surface. Both images were recorded in tapping mode. .. 39

Figure 2-6. (A) Schematic of scanning electron microscope. [185] (B) Detectable electron-sample interactions.. 40

Figure 2-7. Contact angle principle. 42

Figure 2-8. Schematic representation of the XPS principle. 44

Figure 2-9. Jablonski energy diagram [186] 46

Figure 2-10. Chemical structure (A) and absorbance- and emission spectrum (B) of Alexa Fluor 488 label. The maximum absorption and emission are located at a wavelength of 495 nm and 519 nm respectively. This means that there is a Stokes shift of 24 nm. 48

Figure 2-11. Chemical structure of the 6-FAM label. 49

Figure 2-12. Confocal fluorescence microscope configuration. 50

Figure 2-13. Emission spectrum of PDA in methanol, taken at λ_{EX} = 340 nm. Three emission peaks can be seen at 376 nm, 396 nm, 415 nm and a shoulder at 440 nm...... 51

Figure 3-1. Cross-section SEM image of CNW morphology [187] 54

Figure 3-2. (A) Top view SEM image of CNW showing the overall morphology. (B) TEM image [187] revealing the almost planar shape and thickness of the CNW. Flakes consist of 4-6 atomic layers. 55

Figure 3-4. (A) Photochemical reaction to bind an unsaturated fatty acid (10-undecenoic acid) to the CNW edges. (B) EDC-mediated reaction to bind amino-modified probe DNA to the fatty acid carboxyl group. 59

Figure 3-5. Confocal fluorescence images of CNW samples. (a) Reference sample where no fatty acid was added. (b) EDC-negative reference sample. (c) Sample where the normal binding protocol was carried out. The bar in the upper right corner was induced by photobleaching of the Alexa dye. The same intensity scale was used for all images........ 61

Figure 3-6. Hybridization of fluorescently labeled target DNA to bound probe DNA. DNA molecules are not drawn to scale.. 62

Figure 3-7. Conventional fluorescence microscopy images of hybridized CNW samples. (a) Fluorescently labeled target DNA hybridized to covalently bound probe DNA. (b) Same sample after denaturation. (c) EDC-negative reference sample with minimal amount of adsorbed target DNA. The same intensity scale was used for all images. 63

Figure 3-8. Graph showing fluorescence intensity after successive hybridization and denaturation steps for two different hybridization temperatures (green triangles: 40°C, blue circles: 60°C). The graph also displays an EDC-negative reference sample (red stars). Odd and even numbers on the x-axis represent hybridization and denaturation runs respectively. 64

Figure 3-9. Influence of the temperature on hybridization with complementary (COM) and single mismatch (MM) DNA strands. 40 °C and 50 °C give the highest intensities. The relative difference between complementary and single mismatch DNA increases with temperature, see ratio COM/MM. Error bars show standard errors averaged over n=7 independent measurements. 65

Figure 3-10. (A) Si substrate with CNW and SEM images of the regions indicated in (A). These regions are (B) Uncovered centre zone, (C) Low density transition zone and (D) Outer area with high density CNW. The scale is the same for all SEM images. 66

Figure 3-11. Contact angle measurements of sample area with high coverage (outer zone) and area with no coverage of CNW (centre zone). Measurements were taken before and after fatty acid attachment. 67

Figure 3-12. Confocal fluorescence images of functionalized CNW grown on quartz (A) and platinum (B). The dark areas are spots where the CNW came off from the substrate. (B) contains a bleached bar, marked by the red rectangle, to confirm that the signal is coming from fluorescent labels. 68

Figure 4-1. 1-Pyrenedecanoic acid structure and π-stacking to graphene. 73

Figure 4-2. Pyrene-1-boronic acid.. 74

Figure 4-3. CFM images of (A) flakes functionalized with PDA and DNA, (B) EDC-negative reference, (C) PDA-negative reference, (D) Flake-negative reference. (E) shows a higher magnification of the EDC-negative sample with bleached bar. The scale bars correspond to 100 µm. 75

Figure 4-4. (A) Emission spectra of PDA taken at different times after the addition of flakes. Excitation wavelength 340 nm. (B) Fluorescence intensity of selected wavelengths plotted against time. 76

Figure 4-5. Fluorescence emission spectra of centrifugation supernatants. Spectra in the left column were taken at PDA signature wavelengths (λ_{EX} = 340 nm). The right column shows spectra taken at the Alexa fluor label signature wavelengths (λ_{EX} = 488 nm). (A, B) show spectra taken after different washing steps of the positive sample. (C, D) spectra compare the supernatants of the first washing step (in MeOH) of the positive sample with the references. (E, F) spectra are taken after the third rinsing step (in SDS)................ 78

Figure 4-6. Comparison of the total amount of material that was rinsed off from the different samples. The amount of material that was added in the beginning of the reaction is also given. The y-axis respresent an arbitrary scale derived from multiplying the fluorescence intensity and volume of the supernatant. 79

Figure 4-7. XPS spectrum of HOPG incubated with pyrene-1-boronic acid. Inset shows a magnification of the area indicated by the dotted square. The B 1s peak is indicated by the arrow. The boron level does not rise above the contamination level. 80

Figure 4-8. Structure of an aryl diazonium salt. X is an (in)organic anion. 83

Figure 4-9. Illustration of 4-nitrobenzene diazonium tetrafluoroborate coupling to graphene. The byproducts N_2 and BF_4^- escape as gas and are rinsed off respectively...... 84

Figure 4-10. Bechamp reduction to convert the nitro group into an amino group. 85

Figure 4-11. Raman spectra of graphene flakes before and after functionalization with nitrobenzenediazonium and subsequent reduction of the nitro group to an amino group. (A) shows an overview of the spectrum. (B, C and D) give an enlarged view of the D peak, G peak and 2D peak respectively.. 86

Figure 4-12. N 1s XPS spectra of HOPG functionalized with diazonium. Spectra were recorded before and after the conversion reaction of NO_2 to NH_2. 88

Figure 4-13. 4-Benzoic acid diazonium tetrafluoroborate. 88

Figure 4-14. Infrared spectra of the 4-benzoic acid diazonium tetrafluoroborate, prepared by two different methods... 90

Figure 4-15. Raman spectra of graphene flakes functionalized with benzoic acid diazonium (method 1) and DNA. Inset: enlargement of the 1000 – 1600 cm^{-1} region with the spectra rescaled to the G peak intensity. 92

Figure 4-16. Raman spectra of graphene flakes functionalized with benzoic acid diazonium (Sodium nitrite route) and DNA. Spectra are rescaled to G peak intensity.................... 93

Figure 5-1. Close-up of an amorphous carbon pillar with cross-sectional view showing the solid backbone and nanostructured surface. The cross-section is indicated by the white dashed line. Images were recorded at IMEC... 97

Figure 5-2. (A) XPS spectrum showing the C 1s peak. Only low levels of C-O, C=O and O=C-OH bonds are present. (B) Raman spectra of bulk and nanostructured material, showing D and G peaks. 98

Figure 5-3. SEM micrographs of amorphous carbon microstructures. (A) and (B) show micro-nano hybrid bridge structures with collapsed-like and arch-like shape respectively. (C) shows a typical array of electrodes with bridge structures on top. (D) portraits a bulk amorphous carbon microstructure 99

Figure 5-4. CFM images of functionalized carbon microstructures. Left side shows micro-nano hybrids while the right side shows bulk structures without the nanostructured outer layer. Top and middle row images are positive samples with bonded DNA. Bottom row images are EDC-negative reference samples. The middle row shows higher magnification images with an area where the fluorescent labels were bleached. 102

Figure 5-5. CFM images of H_2-plasma treated amorphous carbon samples functionalized with fluorescently labeled DNA. (A) Nanostructured sample, (B) bulk sample. 103

Figure 5-6. CFM images of nanostructured samples functionalized with DNA via the diazonium route. (A) Positive sample, (B) higher magnification of positive sample with bleached bar and (C) EDC-negative reference sample showing the carbon structures as dark spots on a reflecting substrate. 104

Figure 5-7. Comparison of the fatty acid route and the diazonium route. CFM images of samples functionalized via the diazonium route (A) and the fatty acid route (B). The mean pixel intensity for both routes is given on the right. 105

Figure 5-8. Illustration of the resistance measurement setup. 106

Figure 5-9. I-V curve of typical amorphous carbon bridge structure with a 20 Ω resistance. 106

Figure 5-10. (A) Measured resistance values for the pristine bridge structures, bridges with fatty acid and bridges with DNA. Nanostructured bridges and bulk bridges were measured, with each a positive and an EDC-negative sample. (B) Graph showing the normalized change in resistance from pristine to DNA functionalized bridges. The resistance change of the reference samples was set to 1. Error bars indicate standard deviation (n=5 for the nanostructured Ref and n=4 for all other)...107

Figure 5-11. (A) Measured resistance values for the pristine bridge structures, bridges with diazonium and bridges with DNA. Nanostructured bridges were measured with a positive and an EDC-negative sample. (B) Graph showing the normalized change in resistance from pristine to DNA functionalized bridges. The resistance change of the reference samples was set to 1. Error bars indicate the standard deviation (n=6). 108

Table 6-1. E-beam resist parameters 113

Figure 6-1. Left: Schematic of electrical contact deposition. (1) Writing the pattern in the e-beam resist and developing. (2) Metal deposition. (3) Lift off. Right: Microscopy image of a flake with four metal contacts (white structures). The orange structure on the left is an alignment marker. 114

Figure 6-2. Magnetoresistance behavior of sample # G1 at selected temperatures between 77 K and 300 K. The magnetic field is oriented parallel to the c axis. The zero field resistivity is given in the insert with the solid line corresponding to the fit function described in the text. 116

Figure 6-3. Magnetoresistance behavior of sample # G2 at selected temperatures between 5 K and 400 K. The zero field resistivity is given in the insert. 117

Table 6-2. Summary of most important magnetoresistance results for sample # G1 and G2 118

Figure 6-4. Magnetoresistance behavior of sample # G1 plotted according to Kohler’s rule for metals. There is a systematic, temperature-dependent displacement and the fitted slopes (ranging from 1.5 to 1.7) are smaller than the expected B^2 dependence. 119

Figure 6-5. SQUID measurements on HOPG sample. Magnetization was measured parallel (left) and perpendicular (right) to the graphite sheets. Data were corrected for diamagnetism. 120

Figure 6-6. Magnetoresistance behavior of sample # G1 plotted at a fixed temperature and magnetic field for various angles between the field direction and the graphene sheets. The fit curves show that the perpendicular field component is responsible for the PMR effect. 121

Figure 6-7. The Hall voltage at 300 K increases strictly linearly with the applied magnetic field and varies proportional to the measuring current...122

Figure 6-8. Hall voltage versus magnetic field of sample # G1 for selected temperatures between 77 K and 300 K. For fields above 1 T there is a deviation from linear behavior, suggesting the presence of anomalous contributions. 124

Figure 6-9. Hall voltage versus magnetic field of sample # G2 for selected temperatures between 77 K and 400 K. The Hall voltage is positive at lower fields but changes to negative values for higher fields. The magnetic field linked to this change is temperature dependent. 124

Table 6-3. Comparison of carrier density and mobility in sample #G1 and G2 126

Figure 6-10. Temperature dependence of the charge-carrier density n (triangles, left scale) and the charge-carrier mobility μ (squares, right scale), derived in the limit of low magnetic fields B → 0. The solid line for the mobility scaling was calculated using equation *(6.7)*. 128

Figure 6-11. Magnetoresistance behavior from sample #G1 plotted according to Kohler's rule taking into account the temperature dependence of n. The temperature-dependent displacement of Figure 6-4 is canceled out.. 130